STATE ESTIMATION AND VALIDATION OF CURRENTS USING DELFT GNSS SINGLE-FREQUENCY PRECISE POINT POSITIONING ALGORITHM

WITH EMPHASIS ON THE VARIANCE MODEL

ERIK MARIA OUDEJANS

TUDelft
Delft
University of
Technology

STATE ESTIMATION AND VALIDATION OF CURRENTS USING DELFT GNSS SINGLE-FREQUENCY PRECISE POINT POSITIONING ALGORITHM

WITH EMPHASIS ON THE VARIANCE MODEL

Erik Maria Oudejans

In partial fulfillment for the requirement for the degree of

Master of Science

in Geoscience and Remote Sensing
at Delft University of Technology
to be defended publicly on February 8, 2021

Supervisor: Dr.ir. C.C.J.M. Tiberius
Committee: Prof.dr.ir. R.F. Hanssen

              Dr.ir. M.A. de Schipper

ACKNOWLEDGMENTS

ABSTRACT

The Delft real-time GNSS single-frequency precise point positioning (RT-SF-PPP) algorithm is extended to include velocity and receiver clock drift as unknown states to be estimated from Global Navigation Satellite Systems (GNSS) measurements. Carrier-phase ambiguities are assumed constant over time. Two different variance models are used, one obtains variance as a function of satellite elevation, and the other obtains variance as a function of carrier-to-noise density ratio as estimated by the receiver. The elevation based variance model was used in the original RT-SF-PPP algorithm, and adapted to include Doppler measurements. The carrier-to-noise density ratio based variance model components are estimated from double difference (DD) observation combinations using measurements obtained from a short-baseline experiment with two receivers setup over multiple days. Two velocity observables are used and related to velocity and clock drift through the extended functional model of the original algorithm: the receiver generated Doppler and a time-derivative of the carrier-phase observable: the time-differenced carrier-phase (TDCP). Algorithmic performance is evaluated by the horizontal RMSE, which represents accuracy as the variance plus bias squared, precision and reliability. This was validated using three different experiments: a stationary receiver on top of a roof, a buoy freely adrift in the North Sea, and a receiver mounted on a car driving a regional road. It was found that in terms of position in the static experiment and under calm water conditions during the drifting buoy experiment the horizontal RMSE was between 0.429 and 0.530 [m], and under rough water conditions and a road partly flanked by fences and trees between 0.682 and 0.812 [m]. Furthermore in terms of velocity it was found that the TDCP observable in combination with the carrier-to-noise density based variance model has a horizontal RMSE between 0.014 and 0.068 [m/s] over all experiments, and using the Doppler observable with either variance model a RMSE between 0.033 and 0.122 [m/s]. The algorithm was even found by means of external reliability to be capable of detecting faults at the boundary of 0.5 [m] for position and 0.1 [m/s] for velocity in the TDCP observable case.

CONTENTS

INTRODUCTION

Coastal engineers predict the impact of ocean dynamics on shore systems, anticipating dangerous currents within the surf zone is key for a lifeguard, an Olympic sailor dealing with open water wants to know the state of this field before the race.
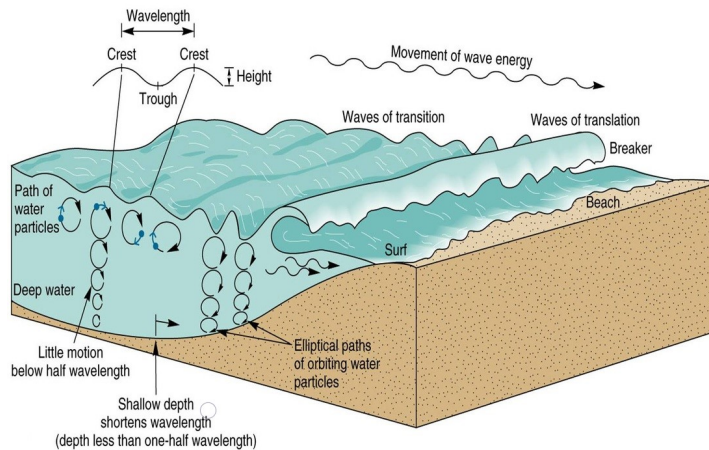
Figure 1: Schematic representation of an ocean-shore system. [Online, 01-10-2019]

Acquiring information on the state of the ocean surface in a reliable way is often non-trivial, for a system involving fluids there are many factors that influence the state. Major contributors for ocean currents are wind, density, the Coriolis effect and tides, especially at small scales this combination of contributing factors leads to uncertain predictions. [Laxague et al., 2018] Shore topography adds another layer of complexity as shallower water leads to shorter crest to crest distances, as Fig. 1 shows.

1.1 ALGORITHM REQUIREMENTS

In this work we attempt to measure and estimate the state of horizontal currents in the upper part of the ocean, which is defined to be at most 1 meter deep, which affects both swimmers and sailboats that reach no deeper.

Together with the Sailing Innovation Centre and the department of Hydraulic Engineering at Delft University of Technology we develop a horizontal currents state estimation algorithm. Where measurements related to the state of currents are obtained from a freely drifting buoy system, that is equipped with a receiver and antenna

tuned to Global Navigation Satellite Systems (GNSS). We assume that these GNSS measurements are representative for the horizontal currents of the upper layer of the water body. The performance of the algorithm is aimed to meet the following requirements:

- Be operated in real-time

- Have horizontal velocity RMSE $\leqslant$ 0.1 [m/s]

- Have horizontal position RMSE $\leqslant$ 0.5 [m]

Where operation in real-time allows for flexible, on-the-fly insights into the state of the water surface. The horizontal velocity error is a hard requirement set by the Sailing Innovation Centre. The position requirement may be strict in open water conditions as water is incompressible and does not take sharp turns, but in case coastguards want to find dangerous currents in the surfzone and determine where to place their flags to signal where swimmers can safely swim, a 0.5 [m] RMSE should be sufficiently accurate and is on the safe side. Given the algorithm requirements the following questions are investigated in this work:

- What is the best approach to estimate velocity?

- What is the formal position and velocity precision?

- What is the empirical position and velocity accuracy?

- What are the internal- and external reliability?

1.2   SATELLITE NAVIGATION POSITIONING APPROACHES

Position, velocity and time can be estimated using GNSS measurements. There is no "one size fits all" approach, but rather an approach fine-tuned to the requirements. Positioning based on GNSS can roughly be categorized into the following four classes where we list the approximate root-mean-squared error (RMSE) between braces: 1) standalone receiver solutions (5 to 10[m]). 2) regional satellite-based augmented systems and precise point positioning (PPP) type solutions (1 to 0.1[m]). 3) local relative baseline (RTK) or network solutions (0.01[m]). And 4) the long distance, long time relative solutions (0.01 to 0.001[m]).

Both PPP and RTK type approaches can estimate states in real-time; we adapt the PPP type approach based on the following considerations. First of all PPP is baseline independent, which means that corrections do not rely on a nearby base station. This is important because in surf-zone or open water settings we are not guaranteed to have a suitable location for a base station. Deploying a base station requires understanding of geodetic surveying and is prone to human

error. Secondly, in addition to the simplicity argument, it is also more cost efficient, there is no need for a base station.

There is also no single best PPP approach. The Mathematical Geodesy and Positioning (MGP) group, part of the Department of Geosciences & Remote Sensing (GRS) at Delft University of Technology have developed and tested a special ppp branch. Known as real time single frequency PPP (RT-SF-PPP). It uses a single GNSS frequency and can use more than one constellation. [Le and Tiberius, 2007, Le et al., 2009, van Bree and Tiberius, 2012, de Bakker and Tiberius, 2017] In this work we adapt this Delft RT-SF-PPP approach and expand it to estimate velocity and clock drift as states.

1.3   CONTEXT OF BUOYS FOR WAVE MONITORING

We are not the first and probably not the last to combine buoys and GNSS measurements. Drifting buoys fall within the category of Lagrangian methods, they move with the flow of water and wind. Valk et al. [2014] used a moored buoy equipped with GPS to detect slack tides. Slack tides are the tipping point from high to low tides or the other way around. They mapped three dimensional currents to a one dimensional space using principle component analysis. This dominant current direction is then used to geometrically determine whether the slack tide moment has past or not. [Herbers et al., 2012] have explored several commercial available buoys equipped with GPS, one of their findings is that buoys can have a limited position accuracy, but still resolve velocity even when significant wave height is less than 1[m]. They also find that velocity estimates agree between GPS and inertial measurement units (imu), providing foundation that low-cost GNSS solutions are a worthy candidate to measure currents.

Buoys are not the only method to estimate horizontal currents. Klemas [2012] lists alternative methods, we can group these alternatives into three categories. Eularian, shore based Radar and satellite systems.

Eularian techniques focus on a specific location of a water body, these can be in-situ systems like stationary rotors or propellers, but most of the time involve some type of acoustic Doppler current profiler (ADCP). These ADCP systems emit a sound wave at both fixed frequency and time interval. As the wave travels trough a water column it interacts with particles in the water, causing the wave to be in part reflected, if the particle is in motion the return signal seems to shift in frequency when observed, known as the Doppler effect. Which occurs for both light and sound waves. This effect is related to the line of sight (LOS) velocity vector, given several incidence angles of the wave we can estimate the horizontal velocity of currents. [Oberg and Mueller, 2007, Brumley et al., 1991]

Shore-based Radar systems (SBRS) are another way to estimate surface currents. Like ADCP Oceanographers estimate current properties using the Doppler shifted signal reflection. Just like ADCP a single Radar cannot split LOS velocity into different velocity components, to overcome this Paduan and Rosenfeld [1996] use an array of at least two Radars to make the distinction. Ohlmann et al. [2007] deploy a batch of buoys to compare the accuracy, they use the buoys as reference. They found that the difference between both methods varies with time, there is both a discrepancy in RMSE differences and bias. With average RMSE difference of 0.07 to 0.14 [m/s] and bias of 0.07 to 0.11 [m/s]. They link the RMSE discrepancy to difference in spatial resolution compared to buoys and antenna pattern. Radars can be characterized by their range resolution, this is the ability to distinguish between targets in the range direction, range resolution depends on transmitted pulse width, beamwidth, type of target, size of target and radar receiver efficiency. Range resolution determines for a major part the spatial resolution of currents sampling, buoys equipped with GNSS measurement system do not have this drawback. They furthermore expect the antenna pattern to change with time resulting in 0.05[m/s] difference, antenna pattern distortions are also likely to cause the observed biases.

Satellite remote sensing is another way to observe surface currents. Compared to buoys the field of view is usually much larger, even more as is the case with SBRS. Because of the large distance between sensor and target the spatial resolution is poor compared to what a buoy equipped with GNSS is capable of. Most satellites are also not capable of continuous real time measurements, exception would be a satellite in geostationary orbit, this type of orbit is not easily maintainable for most inclinations. Satellite based techniques are usually used to measure over large spatial distances. Klemas [2012] distinguishes three satellite based methods:

1) Thermal-infrared or visible pattern recognition where images are scanned for patterns. It usually requires two or more images taken over time, coherence of these patterns is necessary, where a mapping is estimated to translate between spatial patterns in both images. Based on this mapping a rough estimate of current velocity is obtained. [Liu et al., 2017]

2) Oceanographers use Synthetic Aperture Radar (SAR) based techniques in two ways. The back scatter of the Radar beam is linked to various ocean surface states. These states consist of winds, waves, and currents on the ocean surface. Additionally like SBRS Doppler shift is obtained and can be used in a similar manner.[Romeiser et al., 2005, Romeiser, 2007]

3) Radar or Lidar based altimetry provides a direct measurement of sea surface heights. Differences in height link to pressure gradients. When the pressure gradient is in balance with the Coriolis

effect predictable currents arise. Better known as geostrophic currents. For large spatial scales it is sufficient to assume geostrophic currents.[Robinson, 2004, Vigo et al., 2018]

Additionally GNSS reflectometry (GNSS-R) is another satellite based method were signal reflections on the water surface are measured, si multipath is the measurement. The mathematical model links these measurements geometrically to the location of the satellite, the point of reflection on the water and the position of the receiver antenna. Several surface water parameters can be estimated such as significant wave heights or roughness. [Caparrini et al., 2007, Alonso-Arroyo et al., 2015]

Given the requirements only drifting buoys equipped with a GNSS system, Eularian, SBRS and GNSS-R methods are capable of real time measuring. Of these four the Eularian methods have the smallest spatial resolution. SBRS and GNSS-R span a much larger area. Compared to buoys, they both need a stable platform to operate from. This is not a guarantee at sea.

Buoys have proven to be reliable, accurate and low cost. Even though they do not cover as large of an area compared to SBRS or GNSS-R, we are not looking to cover the scale of the Volvo Ocean Race, but rather to acquire information on difficult to predict areas before a race or at the Dutch coast to anticipate dangerous currents.

1.4 RESEARCH MOTIVATION

The majority of research on GNSS focuses on position estimation. Be it single or multi frequency and/or constellation. Integrity monitoring and ambiguity resolution are two examples of the effort; where ambiguity resolution is about estimation of carrier-phase measurement ambiguity in an efficient way and integrity monitoring refers to how reliable the state estimate is, including checking for outliers, faults and other anomalies in the measurement system in order to make the system fault tolerant. [Borre and Tiberius, 2000, Teunissen et al., 2003, Teunissen, 2001b, Teunissen and Verhagen, 2009]

Velocity estimation through GNSS has had a strong emphasis on the functional model and what observable to use. [Freda et al., 2015, Bevly et al., 2000, Wieser, 2007] In this thesis we propose a single model for both position and velocity and elaborate on the stochastic model for single frequency GNSS receivers. The goal is to gain more insight in the quality of the measurements, which allows for better weighting in the estimation process.

1.5 OUTLINE

Chapters two and three give a concise overview of how position and velocity are estimated, this includes the functional model, its correc-

tions and the stochastic model. It further describes parameter estimation and online integrity monitoring. Chapter four describes the experiments conducted throughout this work. Chapter five describes how we estimate the carrier-to-noise density based variance model and other stochastic components of interest such as correlation. Chapter six describes the obtained results and insights of both the static and kinematic experiments. Chapter seven discusses the methodology and hands over possible improvements and research opportunities. Chapter eight concludes the work mostly following the questions posed in the introduction.

SINGLE FREQUENCY PPP: POSITION

2.1 FUNCTIONAL AND STOCHASTIC MODEL

Humans, animals and plants use their senses to perceive the world. If you take a series of images of a plant over the day you notice it follows the light source. Usually the Sun. Rays that reach the photo-receptors trigger a hormone called auxin. This hormone causes shaded cells to elongate. Causing a bend towards the light. Optimal in the sense of leaf surface area aimed at the Sun. [Kong and Okajima, 2016, Peer et al., 2011]

In geodetic state estimation problems we are in some sense also searching for the optimal bend. A mathematical model is formulated, consisting of a functional and stochastic model. We use a functional model to link measurements to state variables. Eq. 1 describes the functional model in a formal way. It also describes the stochastic model. The stochastic model captures uncertainty which we cannot account for in the functional model. Measurements can be ranges from satellites to the receiver on a floating buoy, and state variables are geometric position and velocity coordinates, next to (nuisance) parameters accounting for instance for systematic effects in the measurements, as the bias caused by the receiver clock error.

$$E\left\{\underline{y}\right\} = Ax; \qquad D\left\{\underline{y}\right\} = Q_{\underline{y}} \qquad (1)$$

With measurement vector y. x the deterministic state vector. $E\{\cdot\}$ and $D\{\cdot\}$ the expectation and dispersion operators. Matrix A the linear model that maps x to y. And variance matrix $Q_{\underline{y}}$. Syntax-wise underlining means the term is stochastic. Matrices are written in uppercase.

2.1.1 Observation Equations

Vector $\underline{y}$ contains code and phase observables to all satellites in view in the rtsfppp positioning case. Given two satellites we get,

$$\underline{y} = \begin{bmatrix} \underline{P}_r^1 \\ \underline{\Phi}_r^1 \\ \underline{P}_r^2 \\ \underline{\Phi}_r^1 \end{bmatrix} \qquad (2)$$

With $\underline{P}_r^s$ and $\underline{\Phi}_r^s$ the code and phase observables measured by receiver r from satellite s. Following De Bakker [2016] pp.14 we can formulate the observation equations of Eq. 2 as,

$$\underline{P}_r^s(t_r) = \|r^s(t_r - \tau_r^s) - r_r(t_r)\| + c_0\delta t_r(t_r) - c_0\delta t^s(t_r - \tau_r^s) + \\ T_r^s(t_r) + I_r^s(t_r) + c_0 d_r^s(t_r) + \underline{\epsilon}_r^s \quad (3)$$

And,

$$\underline{\Phi}_r^s(t_r) = \|r^s(t_r - \tau_r^s) - r_r(t_r)\| + c_0\delta t_r(t_r) - c_0\delta t^s(t_r - \tau_r^s) + \\ T_r^s(t_r) - I_r^s(t_r) + \lambda a_r^s + c_0\delta_r^s(t_r) + \underline{\epsilon}_r^s \quad (4)$$

The first term in Eqs. 3 and 4 is the geometric range between satellite and receiver antennae at time of transmission t_r. With $r^s(t_r - \tau_r^s)$ and $r_r(t_r)$ satellite and receiver position vectors at time of transmission $(t_r - \tau_r^s)$ and reception (t_r). Expandable as $r_r = (x_r \ y_r \ z_r)^\mathsf{T}$ and $r^s = (x^s \ y^s \ z^s)^\mathsf{T}$. c_0 the speed of light in a vacuum. Receiver and satellite clock biases $\delta t_r(t_r)$ and $\delta t^s(t_r - \tau_r^s)$. Troposphere delay $T_r^s(t_r)$. Ionospheric delay or phase advance $I_r^s(t_r)$. Constant phase ambiguity a_r^s in cycles with λ the carrier wavelength. And any other systematic delays specified as d_r^s and δ_r^s. And $\underline{\epsilon}$ and $\underline{\epsilon}$ the random code and phase measurement errors.

2.1.2   Corrections

Corrections are generally applied before least squares adjustment. To diminish terms atleast partially through modeling. Following De Bakker [2016] we distinguish between the error terms in table 1.

The first column states the term. The second column specifies if we take the term into account for the rtsfppp algorithm. This can hold three different values: 'yes', 'no' or 'estimated'. If 'yes 'then we correct for it to the best of our knowledge or information present. If 'no' then the term is either so small that it falls well below the noise levels expected using low cost hardware. Or we do not have a sufficient accurate model to even consider correcting for it. If 'estimated' then the term is of importance. There is however no way to accurately model it. This is the case for the receiver clock bias which is expected to behave chaotic. The receiver instrumental delays are lumped with the receiver clock bias. In the single frequency case we cannot distinguish between the two. Therefore our estimate of the receiver clock bias also contain the receiver hardware delays.

For a more in depth discussion the reader is referred to De Bakker [2016] pp.13-29 and Kleijer [2004] for troposphere delay in particular. Correction does not imply we fully remove the term. Rather to the best of our knowledge or to the information that is present. The troposphere delay is divided into a wet and dry component. The dry component behaves rather predicable. The wet component does not. [Kleijer, 2004]

Term	Corrected
Troposphere delay	yes
Ionosphere delay/advance	yes
Satellite orbit and clock bias	yes
Receiver clock bias	estimated
Differential code biases	yes
Differential code-phase biases	yes
Phase-windup	yes
Satellite antenna PCO	indirect
Solid Earth tides	yes
Polar tides	no
Antenna PCV	no
Receiver instrumental delays	estimated
Multipath code	no
Multipath phase	no
Ocean loading	no
Relativity	yes

Table 1: Signal delay terms and whether they are corrected for under the real-time single frequency precise point positioning algorithm before adjustment.

As De Bakker [2016] mentions it is possible to estimate the residual wet troposphere delay. This however will weaken our estimation procedure because it lowers the models redundancy. Leading to less reliable estimates of state $\hat{\underline{x}}$.

2.2   NONLINEAR POSITION ESTIMATION

2.2.1   Best Linear Unbiased Estimator (BLUE)

Eq. 1 can be solved for x using least-squares parameter estimation. For this we formulate a least-squares estimator $\hat{\underline{x}}$. The form of $\hat{\underline{x}}$ is constrained. Our constraints aim for an unbiased estimator: $E\{\hat{\underline{x}}\} = x$ and have $\sigma_{\hat{x}}^2$ minimized. Better known as the Best Linear Unbiased Estimator (BLUE). Eq. 5 and Eq. 6 formulate the BLUE estimator $\hat{\underline{x}}$ its uncertainty. [Teunissen, 2000]

$$\hat{\underline{x}} = (A^\mathsf{T} Q_y^{-1} A)^{-1} A^\mathsf{T} Q_y^{-1} \underline{y} \tag{5}$$

with

$$Q_{\hat{x}} = (A^\mathsf{T} Q_y^{-1} A)^{-1} \tag{6}$$

The position model is nonlinear because we expand line of sight distance into a satellite and receiver position coordinates. We use a linear approximation around a local point through Tailor expansion. Eqs.5 and 6 change accordingly. Estimation becomes an iterative process. Stopping when a certain criteria is met. In our case this when the norm of $\hat{x} - x_0$ is smaller than 0.001[m],

$$\hat{x} = x_0 + [\partial_x A(x_0)^\mathsf{T} Q_y^{-1} \partial_x A(x_0)]^{-1} \partial_x A(x_0)^\mathsf{T} Q_y^{-1} [\underline{y} - A(x_0)] \qquad (7)$$

With x_0 the current best estimate of x. $\partial_x A(x_0)$ the Jacobian of nonlinear mapping $A(x)$ with respect to x. The Jacobian contains partial differentials to the elements of state vector x. And $\underline{y} - A(x_0)$ are the observed minus computed (OMC) observations. With variance matrix $Q_{\hat{x}}$,

$$Q_{\hat{x}} = [\partial_x A(x_0)^\mathsf{T} Q_y^{-1} \partial_x A(x_0)]^{-1} \qquad (8)$$

For the linearized approximation in Eqs. 7 and 8 to work we need a first approximation that leads to convergence of the state variables $\hat{x}$ to x. With rtsfppp at epoch 0 we use the code-only adjustment. This model is less precise compared to also using the phase observations. However the state space is smaller, which makes it less likely to not converge properly.

2.2.2   Code-Only Adjustment

As a first approximation of x_0 at epoch 0 we solely rely on code observations. As the code only adjustment needs an x_0 approximation as well we use the center of Earth as $x_0 = [0\ 0\ 0]^\mathsf{T}$. Following De Bakker [2016] pp.53 the linearized code observation at epoch k is,

$$E\{\Delta\rho_{r,k}^m\} = \begin{bmatrix} -\mathbf{A}_{r,k}^m & c_0 u_m \end{bmatrix} \begin{bmatrix} \Delta r_{r,k} \\ \delta t_{r,k} \end{bmatrix} \qquad (9)$$

With $\Delta\rho_{r,k}^S$ the observed minus computed code observations. $\mathbf{A}_{r,k}^m$ the unit direction vectors from receiver to satellites with dimensions mx3. And speed of light in vacuum c_0 times vector with ones $c_0 u_m$.

2.2.3   Code+Phase Adjustment

Similar to Eq. 9 the linearized observation equations of the phase are, [De Bakker, 2016]

$$E\{\Delta\Phi_{r,k}^m\} = \begin{bmatrix} -\mathbf{A}_{r,k}^m & c_0 u_m & \lambda\mathbf{I} \end{bmatrix} \begin{bmatrix} \Delta r_{r,k} \\ \delta t_{r,k} \\ a_r^m \end{bmatrix} \qquad (10)$$

We can formulate the RTSFPPP solution for a single epoch. Here we estimate the state vector with only the information present at the given epoch. For the multi-GNSS case we follow de Bakker and Tiberius [2017]. They mention that according to Montenbruck et al. [2014] biases exist between satellite systems. These biases are added to the state x and estimated accordingly. Given we have S satellites we formulate the system of linearized observation equations as,

$$
E \begin{bmatrix} \Delta \rho_{r,k}^m \\ \Delta \Phi_{r,k}^m \end{bmatrix} = \begin{bmatrix} -\mathbf{A}_{r,k}^m & c_0 u_m & \delta & \\ -\mathbf{A}_{r,k}^m & c_0 u_m & \delta & \lambda \mathbf{I} \end{bmatrix} \begin{bmatrix} \Delta r_{r,k} \\ \delta t_{r,k} \\ b \\ a_r^m \end{bmatrix} \tag{11}
$$

Where in Eq. 11 δ is 0 for GPS and 1 for the other constellations. And unknown bias vector b is introduced. Where we reference all constellations with respect to one. In our case this is GPS. Therefore if we use n constellations, b has shape $[n\text{-}1, 1]$. We can extend the single epoch solution to the multi epoch case. The most relaxed constraints lead to a partially constant state space. de Bakker and Tiberius [2017] assume constant ambiguities a_r^m and thus no cycle slips. Previous estimates of a_r^S are used in the current epoch,

$$
E \begin{bmatrix} \Delta \rho_{r,k}^m \\ \Delta \Phi_{r,k}^m \\ \hat{a}^- \end{bmatrix} = \begin{bmatrix} -\mathbf{A}_{r,k}^m & c_0 u_m & \delta & \\ -\mathbf{A}_{r,k}^m & c_0 u_m & \delta & \lambda \mathbf{I} \\ & & & \lambda \mathbf{I} \end{bmatrix} \begin{bmatrix} \Delta r_{r,k} \\ \delta t_{r,k} \\ b \\ a_r^m \end{bmatrix} \tag{12}
$$

Using a partially constant state space in Eq. 12 implies little constraints on receiver dynamics. We may extend this model and add a dynamic model. One example is the constant velocity dynamical model as discussed in Teunissen [2001a] pp.202 and 216.

Following de Bakker and Tiberius [2017] and De Bakker [2016] the stochastic model for the rtsfppp algorithm is specified as,

$$
D \begin{bmatrix} \Delta \rho_{r,k}^m \\ \Delta \Phi_{r,k}^m \\ \hat{a}^- \end{bmatrix} = \begin{bmatrix} Q_{\rho\rho} & Q_{\rho\Phi} & \\ Q_{\Phi\rho} & Q_{\Phi\Phi} & \\ & & Q_{\hat{a}\hat{a}}^- \end{bmatrix} \tag{13}
$$

With $Q_{\rho\rho}$ and $Q_{\Phi\Phi}$ the variance of code and phase observables. $Q_{\rho\Phi}$ the covariance between code and phase observables. We assume no correlation between observations from different epochs. Thus $\hat{a}^-$ is uncorrelated with the current epoch observations. Observations to different satellites are also assumed to be uncorrelated. This means that $Q_{\rho\rho}$, $Q_{\Phi\Phi}$ and $Q_{\Phi\rho}$ are diagonal matrices.

The cross-correlation between observables is introduced through the corrections. For more discussion on this topic the reader is referred to De Bakker [2016] and de Bakker and Tiberius [2017] pp.3.

2.3 INTEGRITY MONITORING

We use the BLUE estimator in Eqs. 5 and 6 to 'invert' Eq. 1. Both our functional- and stochastic models are tailored to fit measurement vector y. We call the model specification under Eq. 1 our null hypothesis H_0. The validity of H_0 is not guaranteed. As Zaminpardaz and Teunissen [2018] state H_0 can be violated. We may have wrongly specified the functional- or stochastic model. Or a combination of both. We assume the cause of this misspecification to be an underparametrization of the mean of $\underline{y}$. Which according to Zaminpardaz and Teunissen [2018] is the most common error when formulating A and Q_y.

So if we have misspecified our model, there exists an alternative model specification that does justice to the true mean of $\underline{y}$. The set of alternative model specifications are our alternative hypotheses H_i. We specify the alternative models in this set according to common occurring model biases. De Bakker [2016] pp.173 for instance specifies H_i for the geometry-free GNSS model. And distinguishes between outliers in code data, cycle slips and losses of lock in the phase data.

Given redundancy under H_0 we can test it against alternative hypotheses H_i. Redundancy under H_0 is defined as $r = m - rank(A) = m - n$. With r the redundancy, m size of y and n the size of x. Probability of correctly rejecting H_0 is known as the power of a test γ. The power is intimately linked to the non centrality parameter λ [Teunissen, 2006] pp.96. And as Teunissen [2006] pp.101 states: "One is much more interested in the model error that can be detected with a certain probability γ". With non-centrality parameter given as,

$$\lambda_0 = \nabla^\intercal C_i^\intercal Q_y^{-1} Q_{\hat{e}} Q_y^{-1} C_i \nabla \tag{14}$$

The power of our test is determined by A, Q_y and our alternative hypotheses $C_y \nabla$. [Teunissen, 2006] pp.98 The components of Q_y are determined and described in ch. 6. Under H_i our new model is specified as,

$$H_i : \qquad E\{\underline{y}\} = Ax + C_i b_i; \qquad D\{\underline{y}\} = Q_y \tag{15}$$

With C_i specifying the type of model error. b_i the vector with unknown model biases with dimension equal to $rank(C_i)$. The form of $C_i b_i$ is thus constrained by the formulation of H_i. Lets say our alternative hypothesis H_j is such that one observation is affected by an outlier. Then C_j takes form of a canonical unit vector c_j. And b_j is a scalar. [Zaminpardaz and Teunissen, 2018] Note that subscript $[\cdot]_i$ denotes the set of alternative hypotheses. Where $[\cdot]_j$ concerns an individual hypothesis.

Given H_j in Eq. 15 we can specify its BLUE,

$$\hat{\underline{x}}_j = (\bar{A}^\mathsf{T} Q_y^{-1} \bar{A})^{-1} \bar{A}^\mathsf{T} Q_y^{-1} \underline{y} \tag{16}$$

With

$$\bar{A} = P_{C_i}^\perp A; \qquad P_{C_j}^\perp = I_m - C_j (C_j^\mathsf{T} Q_y^{-1} C_j)^{-1} C_j^\mathsf{T} Q_y^{-1} \tag{17}$$

2.3.1 Detection Identification and Adaptation (DIA)

Given H_0, H_i and $r > 0$ we can validate the model under H_0 through statistical testing. We apply a three step procedure as developed by Baarda [1968] and Teunissen [1990]. Steps consist of detection, identification and adaptation (DIA). Detection determines the fit of the model H_0 to the data. If H_0 contains a misspecification we go through identification to identify the most likely location of misspecification. Finally adaptation deals with the found errors and a new H_0 hypothesis is formulated. Testing is based on the least-squares residual vector $\hat{\underline{e}}$ defined as $\hat{\underline{e}} = \underline{y} - A\hat{\underline{x}}$.

Imparato et al. [2018] pp.4 mention that in geodesy detector is generally a choice between two. One based on the overall model test (OMT). The other based on multiple w-tests. This distinction is important because the H_0 acceptance regions differ. The OMT has an ellipsoidal acceptance region while that of the w-test detector is a m-dimensional polygonal region. Each dimension bounded by the univariate w-test given the H_0 and individual alternative hypothesis H_j. In this work we use the detector based on multiple w-test.

As mentioned we solely consider alternative hypotheses where C_i takes form of canonical unit vector c_i. Thus a model misspecification in one observation. Given the set H_i we formulate the w-test statistics as,

$$\underline{w}_i = \frac{C_i^\mathsf{T} Q_y^{-1} \hat{\underline{e}}}{\sqrt{C_i Q_y^{-1} Q_{\hat{e}} Q_y^{-1} C_j}} \tag{18}$$

Eq. 18 is performed for the full set of alternative hypotheses H_i. The w-test statistic for a single alternative hypothesis H_0 is rejected if any of the w-test statistics is greater than some critical region k. With k determined given the univariate type 1 error α_1: $k = \sqrt{\mathcal{X}^2(1,0)}$. If H_0 is rejected the accepted hypothesis H_j is the largest w-test statistic: $|w_j| = max|w| > k$

Finally given we have accepted H_j we adapt to the new situation. The first step is to accept H_j as our new null hypothesis. Then $\hat{x}_j$ becomes the accepted estimate of x. In this work we adapt by ignoring the observation completely. As Teunissen [2018] notes it is also possible that there is no redundancy left for statistical testing. In that

case we state that tests have been indecisive in proposing a suitable alternative hypothesis. The solution is either remeasuring or accepting that there is no solution available.

The DIA procedure is iterative. Identifying one bias in the measurements does not mean the other measurements are without. DIA iterations are performed up to the moment there is no redundancy left or H_0 is accepted.

Detection and identification are central to the integrity of our solution. For both DIA phases we can obtain an idea how sensitive our detector and identifier are. The detector its sensitivity is given by the minimal detectable bias (MDB). That of the identifier by the minimal identifiable bias (MIB). [Imparato et al., 2018]

2.3.2 Minimal Detectable Bias (mdb)

Sensitivity of the detection step is captured by the minimal detectable bias (MDB). Imparato et al. [2018] distinguish between the univariate and multivariate case MDB_1 and MDB_m. The univariate case only looks at H_0 versus H_j. Where test statistic w_j and critical region k are calculated assuming H_j is the only alternative hypothesis. In contrast to the multivariate case. Here critical region k and w_j are determined taking into account the whole set H_i. We focus solely on the univariate case.

MDB_1 is relatively easy to compute. It is the magnitude of the model error that can be detected using probability γ through testing given H_0 and H_j. As mentioned we constrain the set of H_i to a bias in a single observation. Then matrix C_i reduces to canonical unit vector c_i. The MDB_1 $|\nabla_y|$ is then formulated as,

$$|\nabla_y| = \left(\frac{\lambda_0}{c_i^\mathsf{T} Q_y^{-1} Q_{\hat{e}} Q_y^{-1} c_i} \right)^{1/2} \tag{19}$$

Aydin and Demirel [2004] show how λ_0 can be determined. And also note that λ_0 can be approximated as $\lambda_0 = f(\alpha_0, \gamma_0, q, \inf) = (u_{1-\alpha_0/2} - u_{1-\gamma_0})$. With $u_{1-\alpha_0/2}$ and $u_{1-\gamma_0}$ the upper percentage points of the standard normal distribution.

We can take the result of 19 and propagate these minimal detectable biases into the state vector estimate space. This gives us insight in what catastrophe we may expect in case estimation procedure misses a fault in the data. Teunissen [2006]

$$|\nabla_x| = (A^\mathsf{T} Q_y^- A)^- A^\mathsf{T} Q_y^- |\nabla_y| \tag{20}$$

With external reliability vector $|\nabla_x|$.

SINGLE FREQUENCY PPP: VELOCITY

3.1 DOPPLER SHIFT FOR LIGHT

Doppler shift occurs when range between source (s) and observer (r) changes. As result both wavelength and frequency of light are altered. According to special relativity we can make no distinction between movement of source or observer. We have to take a time dilation term into account.[Giancoli, 2008](pp.979) Received wavelength λ_r and frequency f_r are described as:

$$\lambda_r = \lambda^s \sqrt{\frac{c_0 + v_r^s}{c_0 - v_r^s}}; \qquad f_r = f^s \sqrt{\frac{c_0 - v_r^s}{c_0 + v_r^s}} \tag{21}$$

With λ^s the transmit wavelength, c_0 the speed of light in vacuum, v_r^s the relative motion along a the line of sight between source and observer and f^s the transmit frequency. When source and observer move toward each other the relative motion is smaller than zero: $v_r^s < 0$. Resulting in smaller λ_r and larger f_r. And the other way around. See appendix B for a more complete derivation. The Doppler shift is the change in frequency because $v_r^s \neq 0$. And can further be written as:

$$f_D = f_r - f^s \tag{22}$$

Which tells us that also the Doppler shift f_D is larger than 0 when the source approaches the observer. And is smaller than 0 when they move away from one another.

3.2 DOPPLER SHIFT FOR GNSS

We can make assumptions on the dynamics of v_r^s. Where now $_r$ denotes receiver and ^{s} satellite. In particular when the relative velocity is much smaller than the speed of light: $v_r^s \ll c_0$. This is the case for GNSS current velocity state estimation. In appendix B it is shown through Taylor series that second order and higher terms can be neglected. This simplifies Eq.21 to:

$$f_r \approx f^s (1 - \frac{v_r^s}{c_0}) \tag{23}$$

Using Eq. 22, scaling by wavelength λ^s, splitting v_r^s into receiver and satellite velocity components. And assuming that Doppler shift is

solely caused by satellite receiver geometry changes we get the geometric range rate between satellite and receiver:

$$D_r^s = \lambda^s f_D = -\frac{f^s \lambda^s}{c_0} v_r^s = -v_r^s = -(\dot{r}^s - \dot{r}_r)^\top a_r^s \tag{24}$$

$$a_r^s = \frac{r^s - r_r}{\|r^s - r_r\|} \tag{25}$$

With D_r^s the geometric range rate in $[m/s]$, a_r^s a unit vector pointing from receiver to satellite. And $\dot{r}^s$ and $\dot{r}_r$ satellite and receiver velocities in some common frame of reference. Fig. 2 shows a geometric representation of this situation. The sign of Doppler shift is subject to
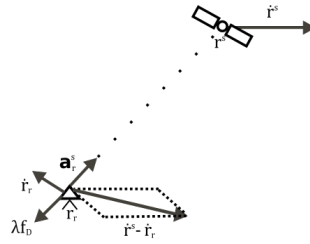
Figure 2: Satellite-receiver geometry for range-rate observables. Satelite and receiver move in opposite directions. Resulting in a relative velocity larger than their individual components. And by definition that Doppler-shift is *positive* for approaching satellites resulting in a negative range-rate.

definition. As can be seen we uniformly define it as: **Doppler shift is positive for approaching satellites**. Which is in line with the RINEX convention. [Gurtner and Estey, 2007] And likewise with the definition found in Teunissen and Montenbruck [2017] (ch.19 Eq. 19.11).

3.3   ASPECTS OF GNSS VELOCITY ESTIMATION

Navigation satellite signals contain Doppler shift as satellite and receiver generally move with respect to each other. As shown, Doppler shift can be linked to receiver and satellite velocities. From analog signal to velocity state estimate various aspects have been investigated over the last three decades. These aspects can be subdivided into three:

- Receiver Architecture Implementation and Noise

- Range-Rate Observables

- Range-Rate Modeling and Processing

The first evaluates receiver architectures. How they propagate noise from analog signal to observables. And how to model this. The second takes the receiver output as baseline. And formulate observables

that contain range-rate information. And the third formulates models and processing routines that estimate velocity states from observables.

3.3.1 Receiver Architecture Implementation and Noise

GNSS receivers architectures are designed within a set of constraints. There is not one architecture best, it depends on application. We can make an abstract representation of these different architectures because they share building blocks. One such abstraction is shown in Fig. 3. Which is a synthesis of representations found in Borio et al. [2009], Teunissen and Montenbruck [2017], Aumayer and Petovello [2015]. With input the received satellite signal (RF Signal). And out-
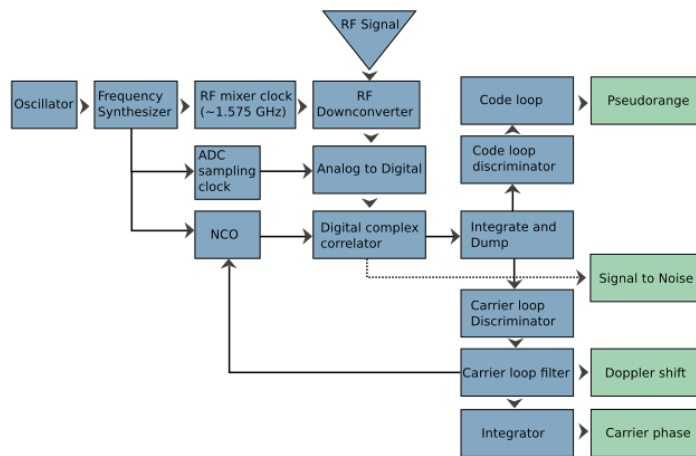
Figure 3

put four observables. Pseudorange, Doppler shift, carrier phase and carrier-to-noise density ratio. The RF signal is first downconverted to an intermediate frequency. It is then converted to a digital signal using an analog to digital converter (ADC). The digital signal is then correlated to a local carrier replica at the integrate and dump block (ID). The route above ID is a delay locked loop (DLL). Which keeps a current estimate of delay between received signal and its replica. And below the ID we find a phase locked loop (PLL). Where in the PLL case the discriminator extracts the phase error. And the loop filter filters the phase error and estimates the Doppler shift. The output of the carrier loop filter steers the numerically controlled oscillator (NCO). And the Doppler shift is integrated to estimate the carrier phase observable.

Borio et al. [2009] derive a theoretical model that describes Doppler noise as consequence of signal tracking. It is assumed that code wipe-off is performed perfectly and input signal is a code-free version of the signal provided by the receiver front-end. And the Doppler state is extracted from the PLL. The PLL is approximated as linear filter.

Using this simplification it is shown that the tracking noise that propagates into the Doppler obervable is a function of C/N_0, coherent integration time and Doppler bandwidth B_D. Where the Doppler bandwidth is a newly introduced term. It determines the ability of a tracking loop to produce smooth frequency estimates:

$$\sigma^2_{f_D} = \frac{B_D}{4\pi^2 T_c^2 C/N_0}(1 + \frac{1}{2T_c C/N_0}) \tag{26}$$

With Doppler bandwidth B_D in [Hz]. See Borio et al. [2009] for a complete explanation of Doppler bandwidth B_D. $\sigma^2_{f_D}$ the Doppler shift variance $[(Hz)^2]$. Coherent integration time T_c. And carrier-to-noise density ratio C/N_0. The variance is inversely proportional to C/N_0. Which leads to the obvious conclusion that satellites at low elevation and low C/N_0 contain more noise in their observations.

Teunissen and Montenbruck [2017] (pp.433) also specify a tracking noise model for Doppler observables. In their model the Doppler is estimated from a frequency locked loop (FFL) instead of a PLL. Which is governed by different mechanisms.:

$$\sigma^2_{f_D} = \frac{4B_{FLL}}{4\pi^2 T_c^2 C/N_0}(1 + \frac{1}{T_c C/N_0}) \tag{27}$$

With B_{FLL} the frequency locked loop bandwidth. Although underlying mechanisms may differ under both variance models. There is a fair bit of overlap between the two.

Borio et al. [2009] put Eq. 26 to the test using both a GNSS software defined receiver and clear-sky data. It is shown that for the two test scenarios the Doppler noise model follows the observed measurement noise closely.

They also mention that a temporary bias is introduced when dynamics change. The loop filter has to adjust to the new situation. For a pedestrian walking at 1.5[m/s] and taking a sharp ninety-degree turn a maximum bias of 0.65[Hz] or 0.12[m/s] at L1 frequency is introduced. This is of course a trade-off within the architecture. A larger loop bandwidth gives less precise observations but makes the tracking more robust to sudden changes in dynamics and the other way around. In open water environments currents do not take sharp turns. Rough surface waves at high frequency may however be able to introduce noticeable biases.

Aumayer and Petovello [2015] present that for *receiver-generated Doppler* observable a scaling occurs. An error in the oscillator in Fig. 3 is propagated. Quantization effects of ADC are ignored. The scaling is derived as:

$$f_D = \frac{f_{D,geom}}{(1+\beta)} - \frac{\beta f_c}{1+\beta} \tag{28}$$

Based on these findings Aumayer and Petovello [2015] proposes that for the final Doppler observable (f_D) both the geometric ($f_{D,geom}$)

and clock drift (βf_c) part of the *receiver-generated Doppler* observable is scaled by the receiver clock drift. For lesser quality oscillators this means that at L1 satellites close to the horizon would experience a 0.046[m/s] range-rate error.

We tested for this proposed effect according to Aumayer and Petovello [2015] for our own u-blox neo m8t receiver. A receiver clock drift of 60 ppm leads to [cm/s] short-term velocity estimate biases. It can be shown that both residuals and velocity state components are influenced. Where the velocity state components show a short-term non-zero mean. We empirically test our hardware for this effect. By comparing the zero-mean assumption against an alternative hypothesis that the mean is not zero:

$$H_0 : \mu = \mu_0, \quad H_a : \mu \neq \mu_0 \tag{29}$$

Since we know the receiver is static, the true velocity is known to be zero. Assuming the variance estimate to be properly computed we convert the individual velocity component estimates to follow the standard normal distribution using:

$$|\hat{\underline{r}}_i / \sigma_i| \tag{30}$$

With velocity component estimate $\hat{\underline{r}}_i$. With subscript i denoting the x, y or z component. Which we substitute with our BLUE velocity component estimates. Formal velocity component standard deviation σ_i. Now choosing level of significance α at 0.1, 0.05 and 0.01 we can check each individual velocity component estimate. Counting the number of occurrences that our null-hypothesis is rejected. Done using the inverse standard normal distribution $\xi_{1-\alpha_0/2}$. If the total amount of rejected samples are larger than α, we have reason to assume that we are not dealing with zero mean velocity components.

Static data is collected for two stationary and independent GNSS receivers with open-sky conditions. Setup for a measurement rate of 10[Hz]. For a total of 25e3 epochs. But processed at 1[Hz] interval. Fig. 4 shows the resulting velocity component estimates.

Now lets focus on table 2. We see that under all chosen α the samples stay well within area $1 - \alpha$. Based on these results we assume that the effect investigated by Aumayer and Petovello [2015] does not play a significant role for our receiver. And therefore neglect implementation of their proposed correction.

3.3.2 Range-rate Observables

In general there are two different range-rate observables used. 1) The already discussed *receiver-generated Doppler* observable scaled by the carrier wavelength. And 2) since the carrier-phase observable is an integration of the Doppler shift we can differentiate its time-series. This gives the reconstructed *time-differenced carrier phase* observable. They
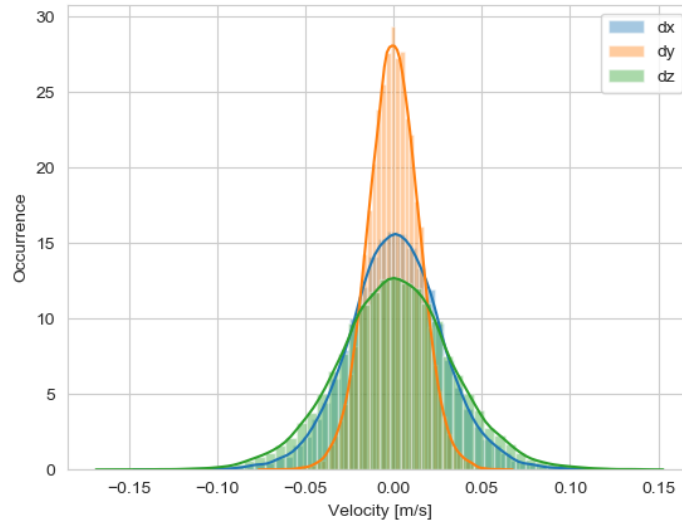
Figure 4: Static u-blox neo m8t GNSS receiver experiment. Situated at Delft Observatorium. Velocity states estimated through Delft single frequency PPP algorithm. In GPS only mode. Sampling was setup at 10[Hz], but data is processed at 1[Hz]. In total 25e3 epochs are used.

α	$P(\frac{\hat{\dot{r}}_x}{\sigma_x} \leqslant \xi_{1-\alpha_0/2})$	$P(\frac{\hat{\dot{r}}_y}{\sigma_y} \leqslant \xi_{1-\alpha_0/2})$	$P(\frac{\hat{\dot{r}}_z}{\sigma_z} \leqslant \xi_{1-\alpha_0/2})$
0.1	0.0446	0.03656	0.0456
0.05	0.01252	0.00908	0.01272
0.01	0.00068	0.00048	0.00116

Table 2: Static u-blox neo m8t GNSS receiver experiment. Used to test if velocity component estimates have zero mean. Or fall under alternative hypothesis that mean is non-zero. Three α levels are used: 0.1, 0.05 and 0.01.

are from hereon expressed in equations as $\underline{D}_r^s$ and $\underline{\dot{\Phi}}_r^s$. The latter is generally assumed to be more precise. [Freda et al., 2015, Salazar et al., 2011] Due to properties of an integrator working on a Gaussian random process.[Lyons, 2004] Producing smooth carrier-phase observables. Whereas the *receiver generated Doppler* is in principle instantaneous. Borio et al. [2009] note that by opportunely filtering timeseries of the latter the precision will become similar. This is intuitively true for an object moving at constant velocity but when dynamics are introduced, this assumption does not hold.

Converting carrier phase time-series to *time-differenced carrier phase* observables requires a differentiator. Bruton [2000] shows that these differentiators can be written as finite-impulse response (FIR) filters:

$$\underline{\dot{\Phi}}_r^k(t) = \sum_{j=-M}^{M} h_M[j]\underline{\Phi}_r^k[t-j] \tag{31}$$

With $\underline{\dot{\Phi}}_r^k(t)$ the *time-differenced carrier phase* observable. Filter coefficients h_M. Filter length of $2M + 1$ carrier phase observations. And carrier phase observable $\underline{\Phi}_r^k$. The ideal differentiator is formulated as [Lyons, 2004]:

$$H(j\omega) = j\omega \text{ for } 0 \leqslant \|\omega\| < \frac{\omega_s}{2} \tag{32}$$

With frequency response $H(j\omega)$, spectrum frequency ω [rad/s]. And angular sampling frequency ω_s [rad/s]. The goal is to formulate filter coefficients h_M in a way that its frequency response resembles Eq. 32. Bruton [2000] gives several considerations. The frequency response should be close to a linear function within the frequency band of interest. The filter should be of odd length. Or else severe position errors will propagate into the velocity estimate. And the absolute length of impulse response is a compromise: larger gives more accurate magnitude response. On the other hand edge effects such as cycle slips will influence the observable longer with larger M.

Bruton [2000] evaluates several differentiators: 1) first-order Taylor, 2) third-order Taylor, 3) high-order Taylor differentiator of order 48 and 4) remez-exchange optimized FIR of order 48, window size 97. The optimal filter is designed to have a transition band from $\omega = 0.4$ to 0.5[rad/s], with ω_s being 0.5[rad/s]. He proposes that Taylor differentiators perform well under static to low dynamics. While the optimal filter performs best under more dynamic situations.

The first-order Taylor differentiator is widely used. [Freda et al., 2015, Salazar et al., 2011, Wieser, 2007, Ding and Wang, 2011, Serrano et al., 2004, Andrew and Boon, 2003, Kennedy, 2003, Hohensinn et al., 2019] It is important to mention that fields of research that use the first-order Taylor differentiator can almost always safely make assumptions on application dynamics. The field of gravimetry is one such application that has open sky and stable trajectory.

One has to take care in open water however. Imagine a drifting buoy in two dimensions, East and Up. And assume that its velocity can be attributed to two factors: currents and waves. Waves are superimposed on the current, which creates a bobbing motion of the buoy. If this bobbing motion has a constant period and we sample our GNSS measurements only when the buoy moves backwards due to the wave, the velocity estimate will become biased.

Luckily open water does not behave in such idealized way. Waves do not have perfectly constant period. However a short-term bias may still be introduced. Therefore higher sampling rates are preferred.

3.3.3   Range-rate Observation Modeling and Processing

Range-rate observables are consistently expressed using observation equation [Misra and Enge, 2006, Salazar et al., 2011]:

$$\underline{D}_r^s = \dot{\rho}_r^s + c_0(\delta \dot{t}_r - \delta \dot{t}^s) + \ddot{T}_r^s - \alpha_f \dot{I}_r^s + \underline{\dot{\varepsilon}}_r^s \tag{33}$$

With $\underline{D}_r^s$ the range-rate expressed in [m/s]. Geometric range-rate $\dot{\rho}_r^s$. Which can be written as function of satellite and receiver velocity: $\dot{\rho}_r^s = -(\dot{\mathbf{r}}^s - \dot{\mathbf{r}}_r)^{\mathsf{T}} \mathbf{a}_r^s$. With $\mathbf{a}_r^s$ the receiver-satellite line of sight vector:

$$\mathbf{a}_r^s(t_r) = \frac{\mathbf{r}^s(t^s) - \mathbf{r}_r(t_r}{\|\mathbf{r}^s(t^s) - \mathbf{r}_r(t_r)\|} \tag{34}$$

Satellite and receiver clock drift $\delta \dot{t}_r$ and $\delta \dot{t}^s$. Troposphere and ionosphere rates $\ddot{T}_r^s$ and $\alpha_f \dot{I}_r^s$. And noise terms $\underline{\dot{\varepsilon}}_r^s$.

Wieser [2007] extends this model for phase-range rate observable. Using:

$$\underline{\dot{\Phi}}_r^s(t) = \frac{\Phi_r^s(t) - \Phi_r^s(t - \Delta t)}{\Delta t} \tag{35}$$

But the derivative of $\underline{\Phi}_r^s$ observables is negative when approaching. In order to align this differentiator with the Doppler definition used here Wieser [2007] defines the Doppler shift as:

$$D_r^s = -\frac{\Phi_r^s}{dt} \tag{36}$$

With which we take the derivative of the carrier-phase observation equation to time, and leads to:

$$\underline{\dot{\Phi}}_r^s(t_r) = -[(\mathbf{I}_3 - \Delta t_r^s \Omega_E)\dot{\mathbf{r}}^s(t^s) - \dot{\mathbf{r}}_r(t_r)]^{\mathsf{T}} \mathbf{a}_r^s(t_r)(1 - \delta \dot{t}_r) - $$
$$c_0(1 - \delta \dot{t}_r)\delta \dot{t}_r + c_0 \delta \dot{t}^s(t^s) - \ddot{T}_r^s(t_r) + \alpha_f \dot{I}_r^s(t_r) - \dot{m}_r^s(t_r) - \tag{37}$$
$$\dot{\vartheta}_r^s(t_r) - \dot{\psi}_r^s(t_r) + \underline{\dot{\varepsilon}}_r^s(t_r)$$

With

$$\mathbf{a}_r^s(t_r) = \frac{[\mathbf{I}_3 - \Omega_E \Delta t_r^s]\mathbf{r}^s(t^s) - \mathbf{r}_r(t_r)}{\|[\mathbf{I}_3 - \Omega_E \Delta t_r^s]\mathbf{r}^s(t^s) - \mathbf{r}_r(t_r)\|} \tag{38}$$

$$\Omega_E = \begin{pmatrix} 0 & -\omega_E & 0 \\ \omega_E & 0 & 0 \\ 0 & 0 & 0 \end{pmatrix} \tag{39}$$

With phase-range rate $\underline{\dot{\Phi}}_r^s(t_r)$ at receiver time t_r. 3-by-3 identity matrix $\mathbf{I}_3$. Signal travel time Δt_r^s. Ω_E the rotation matrix that accounts for Earth's rotation. Satellite and receiver ECEF position and velocity $\mathbf{r}^s$, $\mathbf{r}_r$, $\dot{\mathbf{r}}^s$, $\dot{\mathbf{r}}_r$ in [m] and [m/s]. Time of signal transmission t^s. Directional unit vector $\mathbf{a}_r^s(t_r)$. Speed of light in a vacuum c_0. Satellite and receiver clock drift $\delta \dot{t}^s$ and $\delta \dot{t}_r$. Tropo- and Ionosphere change with time $\ddot{T}_r^s$

and $\alpha_f \dot{I}_r^s$. Multipath change rate $\dot{m}_r^s$. Combined receiver and satellite phase-wind-up rates $\dot{\vartheta}_r^s(t_r)$. Relativistic rate term $\dot{\psi}_r^s(t_r)$. And random noise plus geometric effects not accounted for $\underline{\dot{\varepsilon}}_r^s(t_r)$. And finally the IERS earth rotation rate ω_E, $7.292115090 * 10^{-5}$ [rad/s].

Assuming that clock drift $\delta \dot{t}_r < 100$[ppm]. And derivative of signal propagation time with respect to time can be neglected in phase wrap-up and clock drift terms. Given the maximum range-rate of ± 800[m/s] for GPS. From phase-range-rate contributors in Eq. 37 Wieser [2007] shows that phase-windup rates can be neglected. And multipath is too complex to properly take into account. Below are the most important considerations for the other terms.

3.3.3.1 *Time Considerations*

GNSS receivers have imperfect oscillators. Manifesting in a frequency offset over short time periods. For the *time-differenced* phase methods this frequency offset has two effects. 1) the oscillator frequency offset propagates directly into the perceived signal frequency. The Doppler measurement is therefore incorrect. And 2) the moment of the measurements is also incorrect due to the oscillator frequency offset. And are taken with respect to receiver time. The obtained range-rate observable when differentiating the phase observable with respect to time is therefore:

$$-\frac{d\Phi_r^s}{dt_r} = -\frac{d\Phi_r^s}{dt}\frac{dt}{dt_r} \tag{40}$$

Ignoring term dt/dt_r results in two contributions. First we take the derivative with respect to t_r and not t. This means that our solution epoch contains an offset. We will simply list the epoch of solution as corrected by the estimated clock bias. The second contribution is introduced when evaluating right-hand terms in Eq. 37. Of these terms, those with receiver position/velocity and clock unknowns are found to significantly influence the states. Both contributions account for about 1[mm/s] error for a low-cost receiver clock. [Hohensinn et al., 2019]

dt/dt_r can be derived as [Wieser, 2007, Hohensinn et al., 2019]:

$$\frac{dt}{dt_r} = \frac{1}{1 + \delta \dot{t}_r} \approx (1 - \delta \dot{t}_r). \tag{41}$$

With approximation $(1 - \delta \dot{t}_r)$ accurate up to [mm/s] velocity estimates.

A similar addition to the observation equation is proposed for the *receiver-generated Doppler* observable through Eq. 28.

3.3.3.2 *Geometric Range Rate*

The first term of Eq. 37 is the geometric part of the range rate observable. As shown in Eqs. 33,34,37 and 39 we can expand $\dot{\rho}$ into receiver and satellite velocity and position components. Wieser [2007]
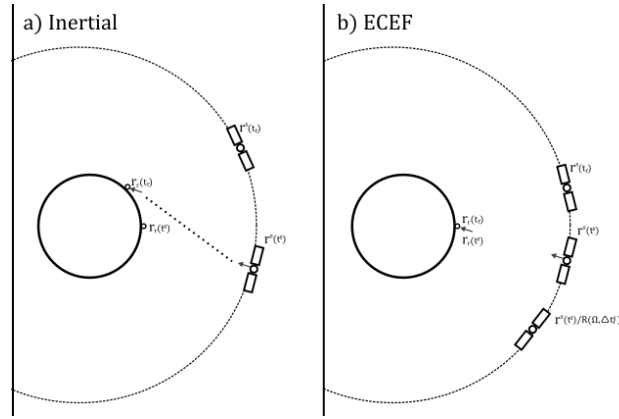
Figure 5: Adapted from Wieser. Apparent signal propagation in inertial and ECEF frame of references. The ECEF-frame rotates with Earths rotation rate. This causes the apparent signal propagation speed to change with time.

chooses to account for Earth's rotation rate here. Since it is convenient to express velocity in an Earth-centered, Earth-fixed frame of reference. Earth's rotation changes the apparent velocity of the signal with time. Fig. 5 shows two situations. a) Inertial frame of reference. Satellite transmits at t^s. Receiver has position $r_r(t^s)$ at time of signal transmission. As the signal propagates towards Earth, receiver moves along with Earth. The signal is received at t_r. b) shows the same signal propagation but here in an ECEF frame of reference. The frame rotates with Earth. Three satellite positions are shown. The middle satellite position denotes the actual position from where the signal is transmitted at t^s. Since the frame moves along with Earth the apparent position from which the satellite transmits its signal is influenced by Earths rotation between t^s and t_r, where the satellite position in ECEF becomes dependent on the Earth rotation, as this effect does not disappear: $r^s(t^s, R(\Omega, \Delta t_r^s))$, shown by the bottom satellite. The top satellite expresses the apparent satellite position at time of reception t_r. For the inertial frame of reference the geometric range-rate can be expressed as:

$$\dot{\rho}_r^s(t_r) = -[\dot{\mathbf{r}}^s(t^s) - \dot{\mathbf{r}}_r(t_r)]^\mathsf{T} \mathbf{a}_r^s \tag{42}$$

With satellite and receiver velocity and position expressed in inertial coordinates. Wieser [2007] expresses the geometric Doppler shift in an ECEF reference frame. With accuracy bound to be better than 10^{-3}[m/s]. The derivation shows that polar motion, precession and nutation rates can be neglected in the transformation. And that only Earth rotation rate has to be accounted for. Due to the situation expressed in Fig. 5. Also known as the Sagnac effect. Which if taken into account compensates for the excess path length due to receiver motion during signal propagation as consequence of expressing positions in an ECEF frame of reference. The Sagnac effect rate contributes

up to 4[mm/s] to the range-rate error budget. By compensating the inertial geometric range-rate for Earth's rotation rate we account for this effect in Eq. 42.

3.3.3.3 *Satellite Position and Velocity*

Wieser [2007] shows that range-rate error due to satellite position and velocity errors can be approximated using satellite centered frame of reference. In terms of radial, along and across track components:

$$\delta D_r^s \approx -[1 \quad 0 \quad 0]\delta \dot{r}^s - [0 \quad 2 \cdot 10^{-4} \quad 0]\delta r^s \tag{43}$$

With Doppler error δD_r^s. And satellite position and velocity errors δr^s, $\delta \dot{r}^s$ expressed in a satellite centered frame of reference. The radial satellite velocity error of 1[mm/s] contributes 1[mm/s]. And 5[m] along-track satellite position error results in 1[mm/s] Doppler error. For real-time orbit products used in our work accuracy of 1[mm/s] or better can be assumed.

Satellite velocity can be obtained in various ways. Kennedy [2003] obtain them by fitting a Lagrange polynomial to satellite positions. This polynomial can be analytically differentiated. However Salazar et al. [2011] concludes through a static experiment that this is actually a weak model for physical satellite orbits. And may yield oscillations known as Runge-phenomenon. Which will bias receiver velocity estimates. They employ a FIR filter differentiator. We will use the approach of Serrano et al. [2004] and take the derivative of satellite position equations. Even though computationally it will be a bit more intensive, it is closer to the actual satellite orbit dynamics.

3.3.3.4 *Troposphere and Ionosphere*

Wieser [2007] underlines that both $\dot{T}_r^s$ and $\dot{I}_r^s$ are relatively stable over time. The largest change occurs due to the changing satellite-receiver geometry. $\dot{T}_r^s$ contributes in the order of 13[mm/s] for satellite elevations above 10[°]. $\dot{I}_r^s$ rarely exceeds 1.5[mm/s] (exception being ionospheric storms). Geometry changes are again the most dominant contributor. A simple broadcast ionosphere model suffices. These findings are independently underlined by Zhang [2007].

3.3.3.5 *Relativistic Corrections*

If satellite orbits would be circular and assuming Earth is a point mass the satellite internal clock would run at constant rate. Satellite orbits are elliptical in reality. This causes the satellites minimum distance to the Earth's surface to vary, known as orbit eccentricity. This variation in distance changes the gravitational potential with time. Which in turn due to relativistic effects causes the clock to run slower and faster at times. Its first derivative, the eccentricity rate contributes

a maximum of 2[mm/s] to the Doppler-shift error budget. [Wieser, 2007]

3.3.3.6 *Baseline and Network Observation Equations*

Stand-alone receiver approaches in Serrano et al. [2004], Freda et al. [2015] have resulted in several [mm/s] level accuracy, the Ionosphere and Troposphere rates leave room for baseline solutions. These terms are spatially correlated, and thus overlap between receivers that are situated near each other. Kennedy [2003], Salazar et al. [2011] formulate the double differenced *time differenced phase* observation equation as:

$$\Delta\nabla\underline{\dot{\Phi}}_{r,k}^{q,p} + \nabla\dot{\rho}_k^{q,p} + e_r^p\dot{r}^p - e_r^q\dot{r}^q = (e_r^p - e_r^q)\dot{r}_r + \Delta\nabla\underline{\dot{\varepsilon}}_r^p \qquad (44)$$

With satellites p and q. Salazar et al. [2011] extends this model to a network solution. It is assumed that receiver clock adjustments are removed a-priori. Either by preprocessing the measurements or using a receiver with clock-steering. A master station 0 is introduced. All measurements will be relative to the master station. A common master clock allows us to estimate satellite clock drifts. Leading to relative clock drifts:

$$\dot{\tau}_r = \dot{t}_r - \dot{t}_0 \qquad (45)$$

$$\dot{\tau}^q = \dot{t}^q - \dot{t}_0 \qquad (46)$$

$$\dot{\tau}_k = \dot{t}_k - \dot{t}_0 \qquad (47)$$

With receiver r, satellite q and reference station k. Using master station 0 and reference station k we can formulate the following system of equations:

$$\dot{\Phi}_{0,r}^q - e_r^q\dot{r}^q = -e_r^q\dot{r}_r + c_0\delta\dot{\tau}_r - c_0\delta\dot{\tau}^q \qquad (48)$$

$$\dot{\Phi}_{0,0}^q - e_0^q\dot{r}^q = -c_0\delta\dot{\tau}^q \qquad (49)$$

$$\dot{\Phi}_{0,k}^q - e_k^q\dot{r}^q = c_0\delta\dot{\tau}_k - c_0\delta\dot{\tau}^q \qquad (50)$$

Where the $_0$ in the first subscript in $\dot{\Phi}_{0,r}^q$ means observation-minus-modelable-effects. The third equation is used to improve the satellite clock drift estimate.

A-priori receiver positions are required at every epoch. As long as the position error does not exceed 10[m] root-mean-squared error it is deemed sufficiently accurate. Both a static and kinematic test are performed. Under the static test it is shown that the network method outperforms both the improved baseline and RTKLIB methods. Under kinematic test conditions the network method outperforms the improved baseline method. The network method accuracy can be improved by increasing the network. Resulting in lower standard deviations for North, East and Up components.
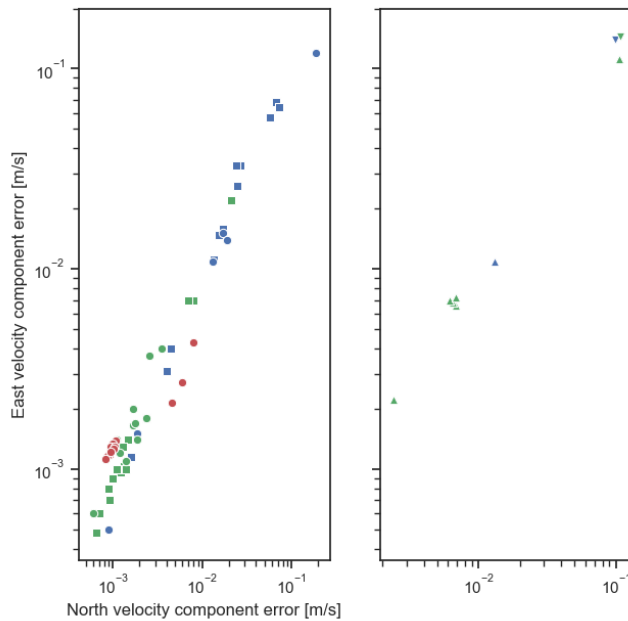
Figure 6: Overview of obtained velocity accuracies through GNSS. In horizontal directions North and East. Overview is split into observable type: receiver generated Doppler (blue), time-differenced phase (green) and network time differenced phase (red). The figure on the left is the result of static experiments. The right kinematic. Usually the receiver is mounted on a plane flying a stable trajectory.

The estimation of the satellite clock drift was necessary at time of research due to correction update rates once every 10 minutes. Nowadays we have final clock and orbit estimates available once every 1[s]. Which improves the accuracy of the interpolation to epoch of measurement.

Fig. 6 shows a synthesis of obtained standard deviations and root-mean-squared errors for various research experiments in literature with velocity estimation through GNSS. The *time-differenced carrier phase* approach is at least a factor ten more precise compared to receiver generated Doppler measurements. Under dynamic experiments, the difference becomes smaller. It is also worth to mention that most of the experiments conducted involve a plane flying in a low-dynamics trajectory. Although it cannot be said that the influence of waves on a buoy are of high dynamics. The North Sea experiment may require assumptions in form of a dynamical model.

3.3.3.7 *Variance Models*

Variance models are almost always assumed diagonal. Wieser [2007], Kennedy [2003], Salazar et al. [2011]. Most approaches employ some form of post processing. Where only cycle-slip free observations are
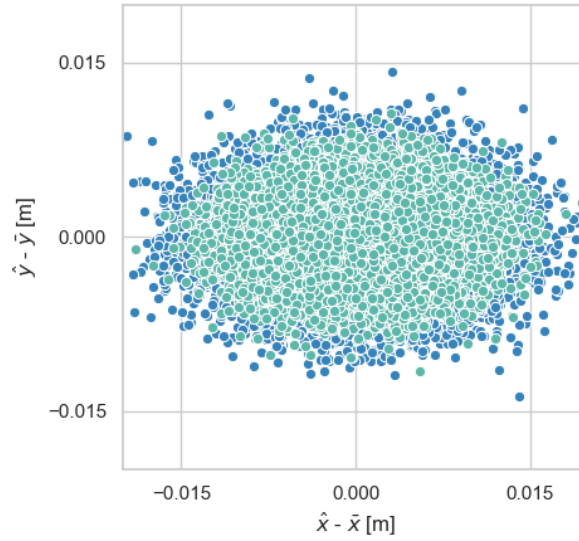
Figure 7: 2D position compared to known reference. Code and phase observables simulated with cross-correlation. Green: cross-correlation taken into account. Blue: cross-correlation not accounted for.

used and positions are estimated before velocity. This inherently assumes there is no correlation between carrier phase and the *differentiated carrier phase*. Which in itself is rather strict. Teunissen et al. [1998] show that not accounting for cross-correlation leads to less precise state estimates. This is shown in the following case. A two-dimensional world with eight satellites orbiting Earth equidistantly in a circular orbit. Receiver is positioned at the North-pole. Observations are Code and Phase. Using single point positioning. Standard deviations are $\sigma_P = 0.5$ and $\sigma_\Phi = 0.005$. And correlation matrix:

$$R_{P,\Phi} = \begin{bmatrix} 1 & 0.6 \\ 0.6 & 1 \end{bmatrix} \tag{51}$$

Fig. 7 shows that after 20000 epochs taking the correlation between observables into account can be shown to lead to more precise estimates.

Wieser [2007] investigates Doppler error using a fixed GPS station. Position and velocity are accurately known. Residuals errors are used to compare performance of three variance models. All three are diagonal:

$$D\{\dot{\Phi}_r^s\} = \sigma_\Phi^2 \tag{52}$$

$$D\{\dot{\Phi}_r^s\} = \frac{\alpha_1}{\sin^2 E} \tag{53}$$

$$D\{\dot{\Phi}_r^s\} = \alpha_2 10^{-\frac{C/N_0}{10}} \tag{54}$$

The first gives equal variance for all Doppler measurements. The second is elevation dependent. And third is the sigma-ϵ variance model.

With scale factors α_1 and α_2. Both are fitted to the median absolute deviation. Which is more robust to outliers. Evaluation is performed assuming $\mathcal{N} \sim (0, \sigma_\phi^2)$. This assumption holds for 80 - 90% for the equal variance model. 80% for the elevation dependent model. And 90 - 95% for the carrier-to-density ratio based model. The results are mostly consistent with literature on GNSS variance models for phase and code observables. With the exception that equal variance outperforms the elevation based model. This hints to variance being uncorrelated to elevation. But rather to site-specific factors such as diffraction and multipath. Another difference between code/carrier and Doppler models is caused by the slow rate of change for Ionosphere and Troposphere delays. Which is of the same order of magnitude as tracking-loop noise. For real-world data, the sigma-ϵ variance model is preferable.

3.4 MATHEMATICAL MODEL FOR VELOCITIES

3.4.1 Observation Equation

We follow observation Eq. 37 as formulated by Wieser [2007]. Which given the Doppler scaling of the *receiver generated Doppler* observable proposed by Aumayer and Petovello [2015] holds for the *receiver generated Doppler* and *time-differenced carrier phase* observables.

3.4.1.1 *Corrections*

Following Wieser [2007] we solely apply corrections that can reach millimeter to centimeter per second levels. These include the special and general relativity terms, the Troposphere and Ionosphere delay rates. The latter two are only varying significantly due to the change in satellite elevation angle. Creating a different angle at which the GNSS signal passes through both layers. The temporal variation of both layers can be neglected.[Wieser, 2007] (pp.34 and 50) This is not always the case. An ionospheric storm for instance may cause the whole model to be misspecified.

Only taking these terms into account Eq.37 simplifies to:

$$
\begin{aligned}
\underline{\dot{\Phi}}_r^s(t_r) = &-[(\mathbf{I}_3 - \Delta t_r^s \Omega_E)\dot{\mathbf{r}}^s(t^s) - \dot{\mathbf{r}}_r(t_r)]^\mathsf{T}\mathbf{a}_r^s(t_r)(1 - \delta\dot{t}_r) - \\
&c_0(1 - \delta\dot{t}_r)\delta\dot{t}_r + c_0\delta\dot{t}^s(t^s) - \dot{T}_r^s(t_r) + \alpha_f\dot{I}_r^s(t_r) - \cancel{\dot{m}_r^s(t_r)} - \\
&\cancel{\dot{\vartheta}_r^s(t_r)} - \cancel{\dot{\psi}_r^s(t_r)} + \underline{\dot{\varepsilon}}_r^s(t_r)
\end{aligned}
\tag{55}
$$

3.4.2 Matrix Representation

3.4.2.1 *Code+Phase+Receiver-generated Doppler*

Given observation equation formulated by Wieser [2007] Eq. 55 the single epoch model is given as:

$$
E\begin{bmatrix} \Delta\rho_{r,k}^m \\ \Delta\Phi_{r,k}^m \\ \Delta D_{r,k}^m \\ \hat{a}^{m-} \end{bmatrix} = \begin{bmatrix} -\mathbf{A}_{r,k}^m & c_0\mathbf{u}_m & \delta & & & \\ -\mathbf{A}_{r,k}^m & c_0\mathbf{u}_m & \delta & \lambda\mathbf{I} & & \\ & & & & -\mathbf{A}_{r,k}^m & c_0\mathbf{u}_m \\ & & & \lambda\mathbf{I} & & \end{bmatrix} \begin{bmatrix} \Delta\mathbf{r}_{r,k} \\ \delta t_{r,k} \\ \mathbf{b} \\ \mathbf{a}_r^m \\ \Delta\dot{\mathbf{r}}_{r,k} \\ \delta\dot{t}_{r,k} \end{bmatrix} \quad (56)
$$

Where $\mathbf{A}$ is a matrix with directional vectors to individual satellites:

$$
\begin{bmatrix} (\mathbf{a}_r^1)^\intercal \\ \vdots \\ (\mathbf{a}_r^m)^\intercal \end{bmatrix} \quad (57)
$$

$\mathbf{u}_m$ is a unit vector of length m satellites. Matrix δ, which is 0 for GPS and 1 for every other system. For each GNSS a new column. Between-system bias vector $\mathbf{b}$. Ambiguity vector $\mathbf{a}_r^m$. Note that ambiguity estimates using information up to the current epoch are included as measurement. This means that we assume that ambiguities are constant. And updated through recursive estimation. A single-epoch solution would exclude ambiguity state estimates.

With partial derivatives to observation Eq. 56 given as:

$$
\frac{\partial D_{r,k}^S}{\partial r_{r,k}} \approx \frac{[\dot{\mathbf{r}}^s - \hat{\dot{\mathbf{r}}}_r(t_r)]^\intercal}{\|\dot{\mathbf{r}}^s - \hat{\dot{\mathbf{r}}}_r(t_r)\|}(\mathbf{I}_3 - \hat{\mathbf{a}}_r^s(t_r)(\hat{\mathbf{a}}_r^s(t_r))^\intercal) \quad (58)
$$

$$
\frac{\partial D_{r,k}^S}{\partial \dot{r}_{r,k}} = (\hat{\mathbf{a}}_r^s(t_r))^\intercal (1 - \delta\tilde{\dot{t}}_r(t_r)) \approx (\hat{\mathbf{a}}_r^s(t_r))^\intercal \quad (59)
$$

$$
\frac{\partial D_{r,k}^S}{\partial \delta\dot{t}_{r,k}} = D_{r,\text{geom}}^s - c_0(1 - 2\delta\tilde{\dot{t}}_r) \approx -c_0 \quad (60)
$$

With $\tilde{[\cdot]}$ denoting approximate values, reiterated until the state variables have converged. Partial derivative to position Eq. 58 is introduced through the LOS unit vector. Wieser [2007] shows that the contribution of this term to ∂D_r^s is small. It mostly depends on the satellite elevation and azimuth angles. If the position offset is 10 [m] in the North direction, it corresponds to 1.5[mm/s] offset in the Doppler estimate.

This is confirmed by following Wieser [2007] method for estimating the influence of offsets in position on the partial derivatives of Doppler shift. Specifying the receiver position error in North, East and Down coordinates the change in δD_r^s is given by:

$$\frac{\delta D_r^s}{\delta r_r} = \left[\frac{(\dot{r}^s - \dot{r}_r)^\top}{\|r^s - r_r\|} (I_3 - a_r^s a_r^{s\top}) C_n^e \right] \tag{61}$$

With Doppler and position errors δD_r^s, δr_r^s. And rotation matrix C_n^e from NED to ECEF is given by Jekeli [2012] pp.25 as a function of receiver longitude ϕ and latitude λ:

$$C_n^e = \begin{bmatrix} -\sin(\phi)\cos(\lambda) & -\sin(\lambda) & -\cos(\phi)\cos(\lambda) \\ -\sin(\phi)\sin(\lambda) & -\cos(\lambda) & -\cos(\phi)\sin(\lambda) \\ \cos(\phi) & 0 & -\sin(\phi) \end{bmatrix} \tag{62}$$
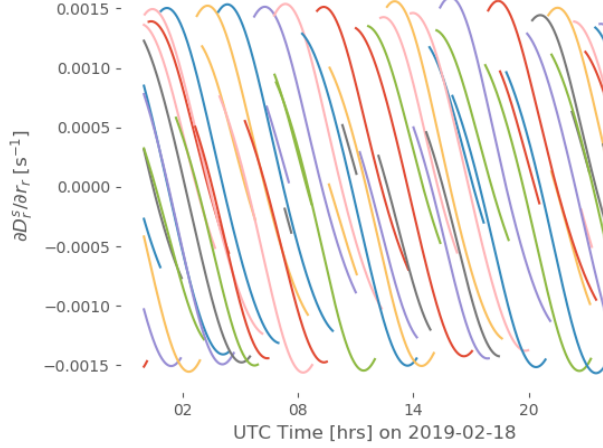
Figure 8: Partial derivatives of Doppler shift with respect to receiver position for a receiver at equator.

Fig. 8 shows Eq. 61 for the full day of 2019-02-18. Note that for this simulation two-line orbit elements were used opposed to precise orbits. The difference between the two are assumed negligible for their insight in this matter. Fig. 9 shows how the introduced error on the partial derivative $\frac{\partial D_r^s}{\partial r_r}$ propagates into the velocity estimate. Here a simple single epoch solution is used with equal variance for all Doppler observations.

The sudden fluctuations are caused by satellites orbiting in and out of view.

Figure 9: 10[m] error in receiver position in North direction propagated into the velocity estimate using single epoch solution. A cutoff angle of 10 [degrees] is used.

3.4.2.2 Code+Phase+Time-differenced Phase

The Code-plus-Phase-plus-Differenced-Phase is shown as:

$$
E \begin{bmatrix} \Delta\rho_{r,k}^m \\ \Delta\Phi_{r,k}^m \\ \Delta\dot\Phi_{r,k}^m \\ \hat{a}^{m-} \end{bmatrix} = \begin{bmatrix} -\mathbf{A}_{r,k}^m & c_0 u_m & \delta & \\ -\mathbf{A}_{r,k}^m & c_0 u_m & \delta & \lambda\mathbf{I} \\ & & & & -\mathbf{A}_{r,k}^m & c_0\mathbf{u}_m \\ & & & \lambda\mathbf{I} \end{bmatrix} \begin{bmatrix} \Delta r_{r,k} \\ \delta t_{r,k} \\ b \\ a_r^m \\ \Delta\dot r_{r,k} \\ \delta\dot t_{r,k} \end{bmatrix} \quad (63)
$$

3.4.2.3 Stochastic Model

The stochastic model for the constant ambiguity code-plus-phase solution was given in Eq.13. We can extend this model to incorporate Doppler observable:

$$
D \begin{bmatrix} \Delta\rho_{r,k}^m \\ \Delta\Phi_{r,k}^m \\ \Delta D_{r,k}^m \\ \hat{a}^- \end{bmatrix} = \begin{bmatrix} Q_{\rho\rho} & Q_{\rho\Phi} & Q_{\rho D} & \\ Q_{\Phi\rho} & Q_{\Phi\Phi} & Q_{\Phi D} & \\ Q_{D\rho} & Q_{D\Phi} & Q_{DD} & \\ & & & Q_{\hat{a}\hat{a}}^- \end{bmatrix} \quad (64)
$$

All terms apart from the ambiguities in Eq. 64 are further investigated in section 4 and 5.

4

EXPERIMENTS

Three main experiments were conducted in this work. Experiments are categorized by their platform, which implies a static or kinematic nature and type of dynamics that we can expect during the experiment. 1) A concrete pillar located on top of the roof of a building. 2) a freely drifting buoy in coastal area. 3) a car driving on a regional road. Experiment receiver, antenna and logging computer are detailed in App. B. General experiment processing settings are detailed in App. F.

4.1 GROUND-TRUTH FOR STATE ESTIMATES

All experiments require a ground-truth for evaluation measures to be computed such as the root-mean-squared-error. In case of a rover of static nature we either have a reference position readily available, or it can be obtained from a long-time average position solution; and velocity can be assumed to be zero assuming the object the antenna is attached to does not move and ignoring solid Earth tides.

In the kinematic case we can no longer rely on the methods above. In this case we follow de Bakker and Tiberius [2017] and use the RTK-type position and velocity solution as reference. With the assumptions that the RTK position solution has an accuracy better by one order of magnitude compared to the PPP solution; and assuming that the RTK solution once the ambiguities are fixed it almost solely relies on carrier-phase measurements, whereas the PPP solution is more strongly dependent on the code observable in comparison.

The final assumption with respect to the RTK processing is that we prefer epochs with fixed carrier-phase ambiguities in order to attain the most accurate reference, resulting in better evaluation of state estimates. RTK processing strategies most useful for this goal are: Forward- and backward processing of the timeseries of collected measurements and an elevation mask of 10 degrees. Since in all experiments the baseline between rover and basestation was sufficiently small precise orbits and ionosphere products were not used, and we solely relied on broadcast information.

After applying the above processing strategies we further select the RTK solution epochs to be used, based on several additional criteria. This selection is founded upon our own field experience and is meant to minimize large faults in the RTK-positioning. In total we formulated three criteria: 1) only use epochs with fixed ambiguities. 2) only use epochs with minimum of 6 satellites, regardless of constel-

lations used. Which guarantees sufficient degrees of freedom for the DIA procedure. 3) For static experiments the sum of formal position error components North, East and Up should be smaller than 0.05[m], and for kinematic experiments smaller than 0.1[m]

From the obtained position state estimates we obtain our velocity reference by taking the time-difference of the position state estimates.

4.2 SHORT-BASELINE EXPERIMENT

The short-baseline experiment consists of a stationary installment of two antennas on the roof of a tall building, offering a virtually unrestricted view of the sky. Distanced apart with small baseline, no longer than 3[m]. The experiment objectives are twofold. First we want to retrieve and model stochastic properties of GNSS measurements and estimate variance model parameters as function of carrier-to-noise density ratio, see Ch. 5. where we follow and expand upon
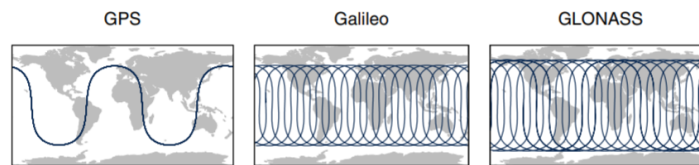

Figure 10: GPS, Galileo and GLONASS repeat tracks for one satellite each. They have ground repeat tracks in roughly 1, 10 and 8 days respectively. Image taken from work of Beer et al. [2020].

the methodology in de Bakker et al. [2012]. The second objective is to evaluate the performance of position and in particular velocity state estimates in the static receiver scenario.

Both receivers are of type μ-blox neo m8t single frequency receiver. Setup to collect code, carrier-phase, Doppler and carrier-to-noise density ratio observations. At a rate of 10[Hz]. Measurements were taken from 1 to 11 May 2017. We aimed for at least 24 hours of uninterrupted measurements. In case we suspected multipath inference we would at least be able to estimate its contribution for GPS code observations. As these groundtracks roughly repeat after a sidereal day, also shown in Fig. 10. For an overview image of the site and pillar setup see App. E.

4.3 NORTH SEA DRIFTING BUOY EXPERIMENT

Two buoys which consist of simple 10[L] water-tight containers filled with a small layer of concrete at the bottom to keep them upright. They are released at several locations near the shore and allowed to drift. Both GNSS receivers are setup similarly to the short-baseline experiment scenario. The experiment was split into two sessions, each spanning about thirty minutes. A basestation was setup on top of

the Sailing Innovation Center located at the coast in the harbor of Scheveningen. An overview of the experiment is shown in Fig. 11, where all four tracks of both the morning and afternoon sessions are shown. It can be seen that the baseline length between the basesta-

Figure 11: Overview map of North Sea drifting buoy experiments. The triangle represents the base station at roof of Sailing Innovation Centre at approximate latitude and longitude: [52.09793, 4.26493]. Four different color tracks are shown. The morning buoys are represented by the red and green lines, the afternoon experiments are represented by the orange and blue lines.

tion and the freely drifting buoys is at all times smaller than 3 kilometers. For images of the experiment see E. From which we assume that atmosphere and ionosphere delay is sufficiently similar for rover and basestation to fix ambiguities on single-frequency using RTK-positioning.

Fig. 12 shows the azimuth and elevation during both the morning and afternoon session.

The objective of the North-Sea drifting buoy experiment is singular. Determine the velocity and position state estimate performance. And determine if and under what circumstances we meet the required horizontal position RMSE of smaller or equal than 0.5 [m] and horizontal velocity RMSE of smaller or qual than 0.1 [m/s]. For an overview image of the drifting buoys and basestation see App. E.

4.4 REGIONAL ROAD EXPERIMENT

The regional road experiment consisted of two GNSS μ-blox m8t neo receivers mounted on top of a car via a magnetic Taoglass Magma
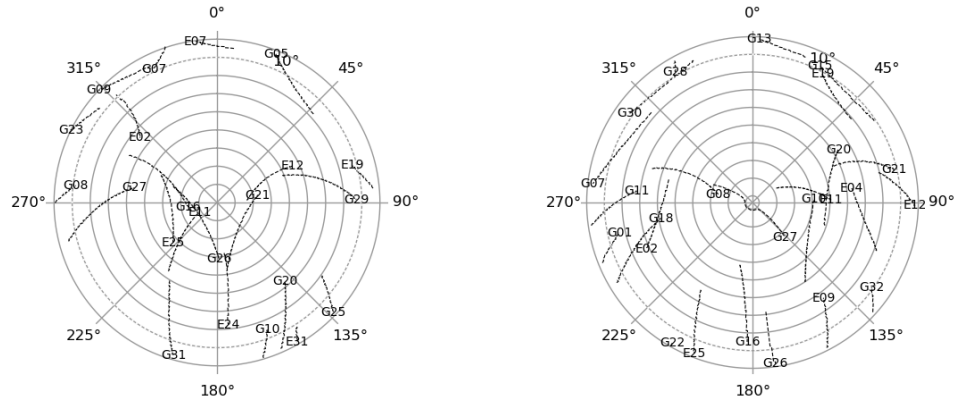
Figure 12: Skyplot for North-Sea drifting buoy experiment. Left image shows the morning session, the right image shows the afternoon session. Only GPS and Galileo satellites are shown.

antenna. The car was driving mostly straight, passing a handful of bridges overhead and turning two round-a-bouts. The goals were determining the velocity algorithm performance as speedometer and compare horizontal RMSE components with respect to the other experiments. Both receivers were setup at 10[Hz] receiving GPS, Galileo and Glonass. International EUREF station DLF100NLD was used as basestation. From overview Fig. 13 it can be shown that the maximum distance from this basestation is around 7.5 kilometers. Which we assume is sufficiently small for ordinary short baseline modeling given the Ionosphere and Troposphere spatial correlation.

4.5   EVALUATION OF EXPERIMENTS

The evaluation experiments with respect to algorithm requirements as stated in Ch. 1 is subdivided into accuracy, precision and reliability.

4.5.1   Accuracy

Given the empirical mean of horizontal state estimate for an unbiased estimator we assume that:

$$E(\hat{\underline{x}} - x) = 0 \ \text{ for all } x \tag{65}$$

In other words our estimator is unbiased if the mean of its distribution equals x.[Teunissen et al., 2006](pp.106) But accuracy is more than only a bias. Mean Squared Error (MSE) the root of it (RMSE) are both measures to evaluate accuracy. The MSE is given by:

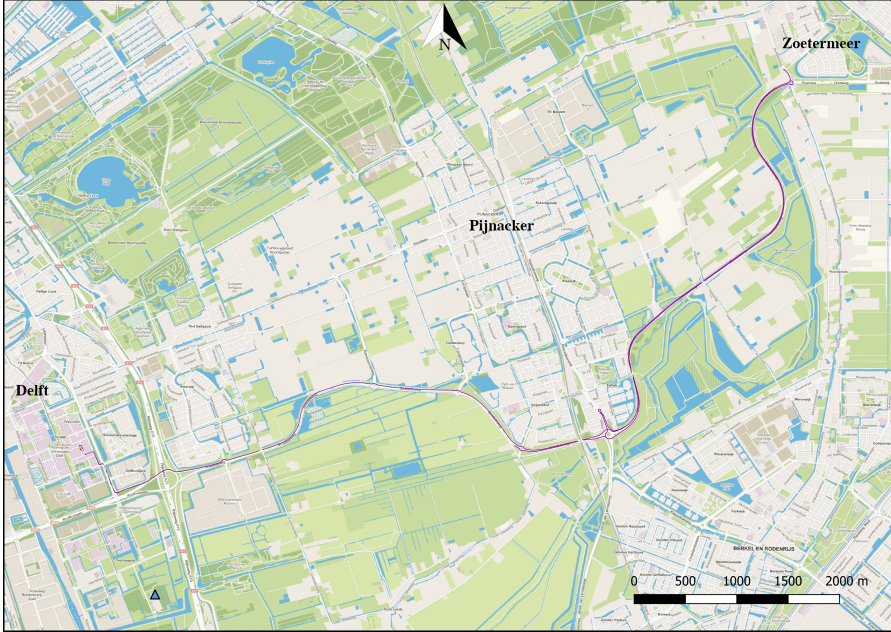$$\text{MSE} = \frac{1}{N} \sum_{i=1}^{N} (y_i - x)^2 \tag{66}$$

Figure 13: Overview map of regional road experiment on the N470 from Delft to Zoetermeer. The triangle represents the base station DLF1 at approximate latitude and longitude: $[51.98602, 4.38746]$. The purple line represents the ground track of receiver 1 which is mounted on the car roof using a magnetic Taoglas Magma 1 antenna.

With y_i measurement i, x the a perfect measurement. Now if we subtract and add state estimate $\hat{x}$ we transform the MSE to the standard-deviation plus bias:

$$MSE = \frac{1}{N} \sum_{i=1}^{N} (y_i - \hat{x})^2 + \frac{1}{N} \sum_{i=1}^{N} (\hat{x} - x)^2 \tag{67}$$

Where the first term is the sample variance, the second term is the bias squared.

4.5.2   Precision

For precision we use the horizontal state estimate components to compute the 99- and 95-percent confidence region. Following Teunissen et al. [2006] pp.285 we determine the confidence region for the case of known variance. And visualize precision, for various experiments and respective stochastic models. In case the variance matrix is known we get the $1 - \alpha$ confidence region as a subset of all state estimates through:

$$S_\alpha(\hat{\underline{x}}) = \|\hat{\underline{x}} - x\|^2_{Q_{xx}^{-1}} \leqslant \chi^2_\alpha(k, 0) \tag{68}$$

Where $\|\hat{\underline{x}} - x\|^2_{Q_{xx}^{-1}}$ is the norm of the state estimate vector error. Where x is not the real ground truth but rather an RTK-based position or ve-
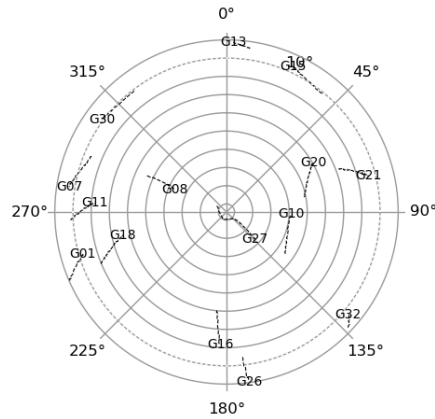
Figure 14: Skyplot for regional road experiment. Only GPS satellites are shown.

locity state estimate vector in this work. Which means our confidence region is centered on the mean difference between the RTK and PPP state estimates. Normalization by variance matrix Q_{xx}^{-1}. Degrees of freedom k, which is one in our case as we use individual components. And $\chi_\alpha^2(k, 0)$ is the ordinate-value of the $\chi^2(k, 0)$ distribution. The resulting confidence region can be interpreted as the region where we expect 95 or 99 percent of state estimates to be in, irrespective of the true state.

4.5.3 Reliability

Reliability is split into internal- and external reliability. Internal reliability evaluated in terms of the MDB and propagated to state estimates to evaluate external reliability. More thoroughly explained at the last section of Ch. 2. This is not part of the requirements but may be insightful next to accuracy and precision evaluation.

VARIANCE MATRIX COMPONENTS

This chapter explains how variance matrix components are obtained. Using data from a short-baseline two-receiver experiment. Formulating linear observation combinations. Correcting for effects that still persist by either subtracting a mean or low-order polynomial. And determining components of interest over 120 second-long bins from these combinations. In this Chapter we solely elaborate on the outcome of these short-baseline static experiments. And the respective variance matrix components.

Code, carrier-phase, Doppler, time-differenced carrier-phase and carrier-to-noise density ratio are all observables of interest. Components of interest for individual observables are variance and time-correlation up to lag of 100 seconds. And between observables the covariance and cross-correlation.

In the first place we are interested in the performance of u-blox neo m8t single-frequency GNSS receiver. And compare results to high-end Septentrio AsteRx1 single-frequency GNSS receiver.

5.1 VARIANCE COMPONENT DETERMINATION

Let variance matrix Eq.64 of Chapter 3 be our starting point:

$$
D \begin{bmatrix} \Delta P_{r,k}^S \\ \Delta \Phi_{r,k}^S \\ \Delta D_{r,k}^S \\ \hat{a}^- \end{bmatrix} = Q_{yy} = \begin{bmatrix} Q_{PP} & Q_{P\Phi} & Q_{PD} & \\ Q_{\Phi P} & Q_{\Phi\Phi} & Q_{\Phi D} & \\ Q_{DP} & Q_{D\Phi} & Q_{DD} & \\ & & & Q_{\hat{a}\hat{a}}^- \end{bmatrix} \tag{69}
$$

For the used hardware the reader is referred to Appendix A. We will estimate all terms in Eq. 69 but $Q_{\hat{a}\hat{a}}^-$. Because the ambiguity variance follows from error propagation of observations to the state space. All terms are modeled as function of the receiver carrier-to-noise density ratio estimates. The method is receiver independent. And retrieves first and higher moments of GNSS observables through linear observation combinations (LC).

5.1.1 Short Baseline Combinations

We build upon the variance component estimation procedure described in de Bakker et al. [2009] and de Bakker et al. [2012]. We formulate time-series of linear combinations of GNSS observables. The resulting time-series are then divided into equal sized bins. And corrected

for any systematic effect still present in their respective observation equations. Using a low-order polynomial or mean.

One receiver allows for combinations between observations to a single satellite. Take differences between observations to different satellites. And take time-differences for a single observable. Using a second receiver adds the between-receiver-difference to the list of possibilities.

On top of that we can also combine combinations. Using double-differenced (DD) carrier-phase observable as an example. We first difference carrier-phase observation between satellites for both receivers individually. Then these newly obtained single differences are differenced between receivers.

As shown by de Bakker et al. [2012], between observation and short-baseline(SB) combinations can be formed such that major error sources cancel out. For instance the common mode error for the receiver, which includes the clock-bias and hardware delays, is similar for all satellites in view. The between observation and SB combinations do however not cancel out all geometric effects.

Effects that remain are, as mentioned, corrected for by subtracting the mean or a low-order polynomial estimated using ordinary least-squares:

$$
E\begin{pmatrix} \underline{y}_1 \\ \vdots \\ \underline{y}_n \end{pmatrix} = \begin{pmatrix} t_1^2 & t_1 & 1 \\ & \vdots & \\ t_n^2 & t_n & 1 \end{pmatrix} \begin{pmatrix} a \\ b \\ c \end{pmatrix} \tag{70}
$$

With $\underline{y}_1$ to $\underline{y}_n$ an instance of a time-series from some combination of length n. The GPS time of week t normalized for the respective series between -1 and 1. And polynomial coefficients a, b and c. We assume the remaining time-series to be randomly distributed. The time-series are of course noisy, this noise will propagate into the polynomial coefficients. But since time-series length n is made sure to be large, we assume that polynomial coefficients model standard deviations σ_a, σ_b and σ_c are small and can be neglected.

The length of all series is kept constant. Length n is a hyper-parameter that can be tuned. This tuning depends on three semantic considerations:

- Small time-series length results in a less precise polynomial estimate. This may introduce an artificial distortion. Furthermore, estimate $\hat{\sigma}_y$ will also be less precise. This latter consideration will however be less of an issue, because with smaller time-series length the amount of available series increases. We therefore have more, but less precise estimates of $\hat{\sigma}_y$, that can in term be resampled and averaged to end up with the same result given larger n.

- Unwanted effects are accounted for by a second order polynomial. Such quadratic functions will fit the data only for a limited timespan due its characteristics. Take for instance a given GNSS broadcast ephemeris frame for a satellite, it is only valid for a few hours a day. Time-series should therefore not be too large to avoid introducing artificial distortions.

- Noise-level on observables varies gradually due to satellite-orbit stability. Satellite carrier to noise density ratio, C/N0 changes with a rate of up to $0,0083[deg/s]$Kaplan and Hegarty [2017]. If segments are too large, we average the gradually changing signal quality of interest.

5.1.2 Variance Estimator

In order to formulate a mapping from time-series to second order moments consider two time-series of random variables, $\underline{y}_1$ and $\underline{y}_2$, with length n. Both are normally distributed with zero mean and have unknown variance $\underline{\sigma}^2_{y_1}$ and $\underline{\sigma}^2_{y_2}$ and unknown covariance $\sigma_{y_1 y_2}$. Given a single random variable time-series we can represent the formal and empirical sample variance for discrete random variable $\underline{y}$, $\underline{\hat{\sigma}}^2_y$ as:

$$\sigma^2_y = D(\underline{y}) = E((\underline{y} - \mu)^2), \ \underline{\hat{\sigma}}^2_y = \frac{1}{n-1} \sum_{i=1}^{n} (y_i - \mu)^2 \tag{71}$$

5.1.3 (Auto)covariance Estimator

And using both time-series we estimate the covariance and auto-covariance on non-diagonal entries for discrete random variables. The auto-covariance can be estimated using the covariance function, with the latter series being a shifted version of the former with shift of τ epochs and $y_1 = y_2$, Otherwise $\tau = 0$:

$$\sigma_{y_1 \ y_2} = E((\underline{y}_1 - \mu_1)(\underline{y}_2 - \mu_2)), \ \underline{\hat{\sigma}}_{y_1 \ y_2}(\tau) = \frac{1}{n-1-\tau} \sum_{i=1}^{n-\tau} ((y_{1,i} - \mu_1)(y_{2,i+\tau} - \mu_2)) \tag{72}$$

5.1.4 Variance Components Expectation and Dispersion

Table 3 gives an overview of the expectations of the linear combinations. With OD two different observations substracted from one another and DD the double difference observation combination. Important are the expectation and dispersion, where the former may give insight into the interpretation of the results, for example in the DD case it is mostly multipath that remains as signal. The dispersion

is necessary in order to correct to single observation case variance from the DD case in the final variance estimates.

Linear Combination	Expectation	Correction	Dispersion
OD $P - \Phi$	$2I - \lambda a + d - \zeta$	Polynomial	σ_ρ^2
OD $D - \dot{\Phi}$	$(\delta \dot{t}_r - \delta \dot{\bar{t}}_r) + (\delta \dot{t} - \delta \dot{\bar{t}}^s)$	Polynomial	σ_D^2
DD P	$m_{P_{DD}}$	Mean	$4\sigma_P^2$
DD Φ	$m_{\Phi_{DD}}$	Mean	$4\sigma_\Phi^2$
DD D	0	Mean	$4\sigma_D^2$
DD $\dot{\Phi}$	0	Mean	$4\sigma_{\dot{\Phi}}^2$
DD S	$m_{S_{DD}}$	Mean	$4\sigma_S^2$

Table 3: Expectation and dispersion of linear combinations of GNSS observables. Used to compute variance matrix components from static baseline observations.

5.2 VARIANCE MODEL OVERVIEW AT 45[DB-HZ]

An overview of variance components obtained through modeling are shown in table 4. We show standard deviation at carrier-to-noise density ratio of 45[dB-Hz] for ease of interpretation. At 45 [dB-Hz]

		u-blox m8t			Septentrio AsteRx1			
		G	R	E	G	R	E	Unit
σ_P	OD	0.2445	0.2256	0.2125	0.2654	-	0.1332	m
σ_P	DD	0.1974	0.2021	0.2328	0.1560	-	0.1225	m
σ_Φ	DD	0.0043	0.0044	0.0035	0.0047	-	0.0034	m
σ_D	DD	0.0885	0.0937	0.0630	0.0461	-	0.0397	m/s
σ_D	OD	0.0151	0.0157	0.0092	-	-	-	m/s
$\sigma_{\dot{\Phi}}$	DD	0.0060	0.0050	0.0053	0.0046	-	0.0004	m/s
σ_S	DD	0.1227	0.0627	0.0620	0.2801	-	0.1335	dB-Hz

Table 4: Modeled standard deviations at 45[dB-Hz]. Model obtained from two separate short-baseline experiments. With two different single-frequency GNSS receivers: u-blox m8t and Septentrio AsteRx1. Observables are code, carrier-phase, Doppler, time-differenced carrier-phase and carrier-to-noise density ratio. (OD=observation difference). (DD=double difference). For constellations: GPS (G), GLONASS (R) and GALILEO (E).

the AsteRx1 receiver has lower standard deviation for code, Doppler and time-differenced carrier-phase. Whereas the u-blox neo m8t has

a slightly better performance for carrier-phase observable. Which is at sub-millimeter level. Overall Galileo performs best, Glonass worst. Compared to the other constellations, Galileo transmits on a wider bandwidth. Which leads to better correlator performance. And therefore better observable estimates.

	u-blox m8t	Septentrio AsteRx1
$\rho(P, \Phi)$	0.00	0.00
$\rho(P, D)$	0.00	0.00
$\rho(P, \dot{\Phi})$	0.00	0.00
$\rho(P, S)$	0.00	0.00
$\rho(\Phi, D)$	-0.75	-0.50
$\rho(\Phi, \dot{\Phi})$	0.00	0.00
$\rho(\Phi, S)$	0.00	0.00
$\rho(\dot{\Phi}, D)$	0.25	0.00
$\rho(\dot{\Phi}, S)$	0.00	0.00

Table 5: Modeled cross-correlation at 45[dB-Hz]. Model obtained from two separate short-baseline experiments. With two different single-frequency GNSS receivers: u-blox neo m8t and Septentrio AsteRx1. Observables are code, carrier-phase, Doppler, time-differenced carrier-phase and carrier-to-noise density ratio.

Table 5 shows the correlation components. Both receivers rely on negative feedback between carrier-phase and Doppler. The u-blox neo m8t has tighter coupling between both. Because Doppler is more instantaneous in comparison this may be by design; to achieve good performance under broad range of user dynamics.

	u-blox m8t	Septentrio AsteRx1
P	0.50	0.20
Φ	0.06	0.20
D	0.00	0.00
$\dot{\Phi}$	-0.03	-0.10
S	0.50	0.20

Table 6: Modeled time-correlation of observables after 1 second. Model obtained from two separate short-baseline experiments. With two different single-frequency GNSS receivers: u-blox neo m8t and Septentrio AsteRx1. Observables are code, carrier-phase, Doppler, time-differenced carrier-phase and carrier-to-noise density ratio.

Table 6 shows time-correlation of observables after one second. AsteRx1 has lower code time-correlation. Whereas the u-blox neo

m8t has lower time-correlation for carrier-phase and time-differenced carrier-phase.

5.3 CODE

Fig. 15 shows the results of the code standard deviation estimates for both receivers. The dots represent the data used for these estimates. Each dot represents a double-differenced time-series segment of 120 seconds. The colors represent three different constellations GPS in blue, Galileo in orange and Glonass in green. The lines represent the modeled standard deviations as function of carrier-to-noise density ratio using simple functional model used in de Bakker et al. [2012]:

$$\hat{\sigma}_P = a 10^{-\frac{C/N_0 - 45}{20}} \tag{73}$$

With C/N_0 in [dB-Hz] and a in [mHz]. For u-blox neo m8t as the carrier-to-noise density ratio becomes lower, the standard deviation sharply increases. Whereas the model fits the AsteRx1 measurements much better over the complete range of carrier-to-density ratios. One possible explanation is that u-blox uses certain assumptions within the receiver model that only work for satellites at higher elevation. For instance assumptions on their velocity.
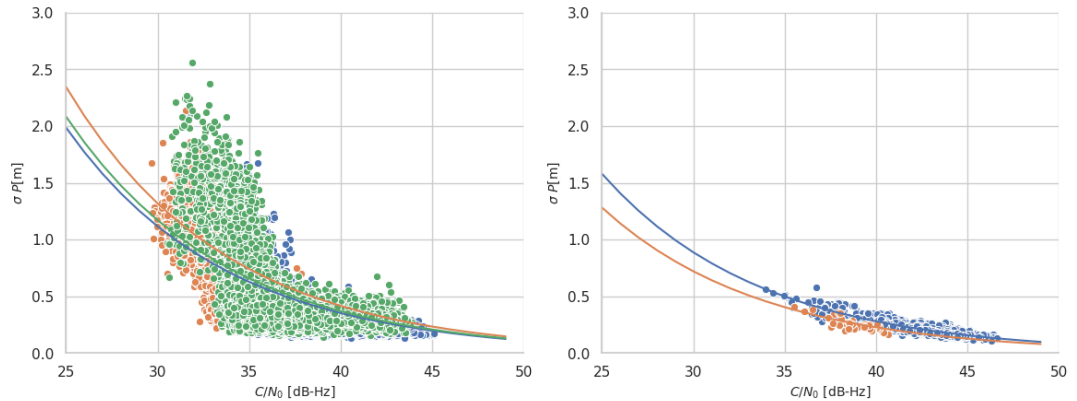

Figure 15: Computed standard deviation of code observable. For two single-frequency GNSS receivers: u-blox m8t (left) and Septentrio (right). Obtained from two short baseline experiments. Using double-difference linear observation combinations.

Fig. 16 shows the observation difference combination. Where carrier-phase is subtracted from code observations. Using polynomial fit to solve for ambiguity and other effects that remain. The dots again represent 120 second long segments of observation differenced time-series. The lines are realizations of functional model in Eq. 73. Note that for u-blox m8t both the OD and DD figures show a sharp increase of noise at around 33[dB-Hz]. But the DD-combination has a smudge-effect. Caused by mixing different levels of carrier-to-noise

density ratios together. We explicitly chose not to apply any criteria for mixing. As this would most likely lower the amount of usable segments.
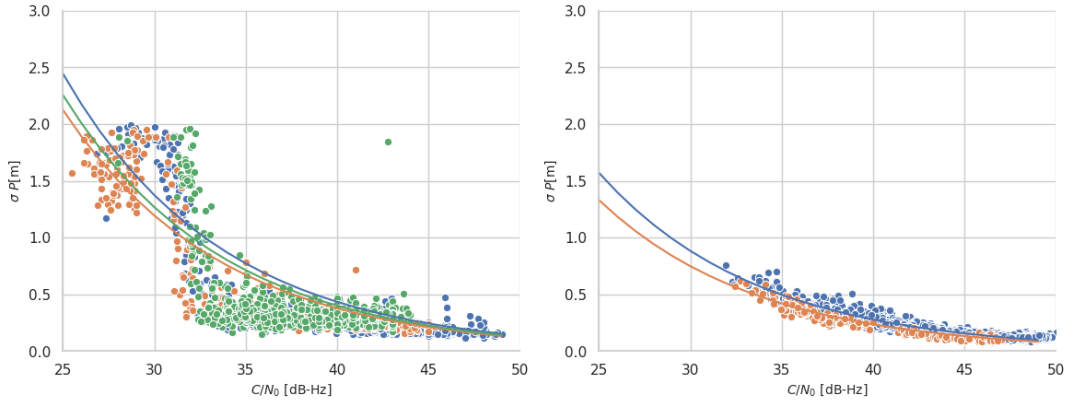

Figure 16: Computed standard deviation of code observable. For u-blox m8t single-frequency GNSS receiver (left) and Septentrio AsteRX 1 receiver (right). Obtained from short baseline experiment. Using observation-difference linear observation combination between code and carrier-phase observables.

A simplified expression of DLL variance is given by Teunissen and Montenbruck [2017] as:

$$\sigma_P^2 = T_C^2 \frac{B_{DLL}d}{2C/N_0}[1 + \frac{2}{(2-d)TC/N_0}] \quad [m^2] \tag{74}$$

With T_C the chip duration [m]. Early-late correlator spacing d [chips]. B_{DLL} the loop bandwidth. Coherent integration time T. And C/N_0 in [ratio-Hz]. The term in brackets represents the squaring loss. Mostly relevant at lower elevations. [Teunissen and Montenbruck, 2017] (pp.431) Two ways to decrease the noise at lower elevations are increasing the coherent integration time T or reduction of the correlation spacing d. We can rewrite Eq. 73 and link it to Eq. 74 by changing the carrier-to-noise density ratio from [dB-Hz] to [ratio-Hz]. Full rewriting can be found in Appendix D:

$$\sigma_\Phi^2 = a^2 b \frac{1}{C/N_0} \tag{75}$$

5.4 CARRIER-PHASE

The computed standard deviation of carrier-phase observations for both receivers is shown in Fig. 17. Both profiles show a rather similar curve. The variance of both receivers is inversely proportional to carrier-to-noise density ratio. Following de Bakker et al. [2009] we can indeed see that all constellations show similar noise profiles for both receivers. Which is in line with theory because the carrier-phase variance only depends on C/N_0 and not on signal modulation. de Bakker
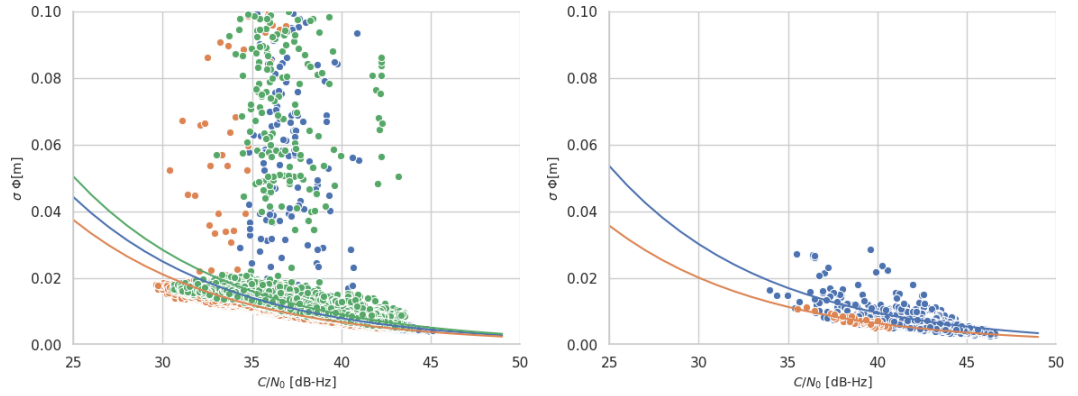
Figure 17: Computed standard deviation of carrier-phase observable. For two single-frequency GNSS receivers: u-blox m8t (left) and Septentrio (right). Obtained from two short baseline experiments. Using double-difference linear observation combinations.

et al. [2009] further note that the receiver clock is not fully removed by means of polynomal correction. Therefore a small effect remains on the DD carrier-phase observations. Which is proportional to the Doppler effect.

A representation of the formal variance of Φ is given by Teunissen and Montenbruck [2017] as:

$$\sigma_\Phi^2 = \frac{\lambda^2}{4\pi^2} \frac{B_{PLL}}{C/N_0}(1 + \frac{1}{TC/N_0}) \quad [m^2] \tag{76}$$

Note the similarity between the formal variance and again the used carrier-to-noise desity ratio model in Eq. 75.

5.5 DOPPLER

The standard deviation estimates of receiver generated Doppler are shown in fig. 18. With u-blox m8t (left) and Septentrio AsteRx1 (right) GNSS receivers. For all C/N_0 the Septentrio AsteRx1 outperforms the u-blox m8t receiver.

Similar to code we utilize the Doppler minus time-differenced carrier-phase. Shown in fig. 19. The standard deviation of this combination may be biased for u-blox m8t specifically. Because as we will see both observables have positive cross-correlation. Which means that the variance estimate is actually lower than it in reality is. It does however show a similar behavior as observed for code in Fig. 16. PLL or FLL parameters are changed to maintain an acceptable noise profile for Doppler observables. Just as with code DD observations it does not become apparent from the double-difference combination, again due to pairing satellites with varying carrier-to-noise density ratio.
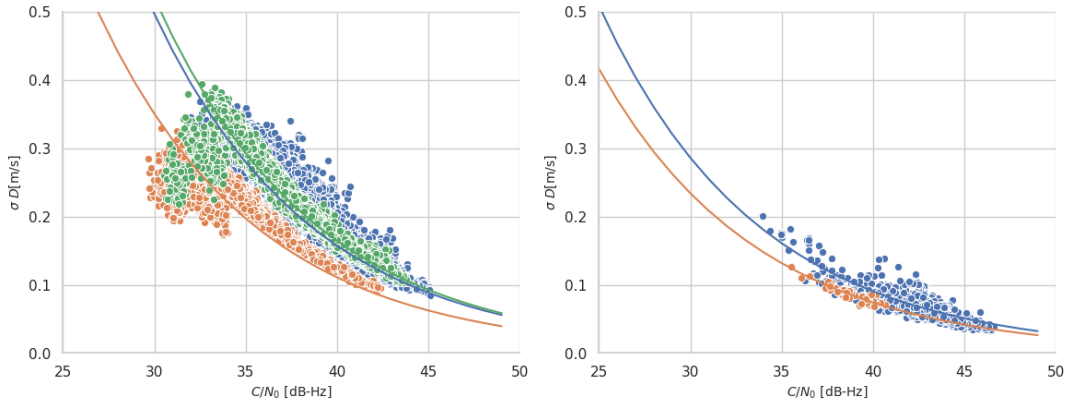
Figure 18: Computed standard deviation of Doppler observable. For two single-frequency GNSS receivers: u-blox m8t (left) and Septentrio (right). Obtained from two short baseline experiments. Using double-difference linear observation combinations.
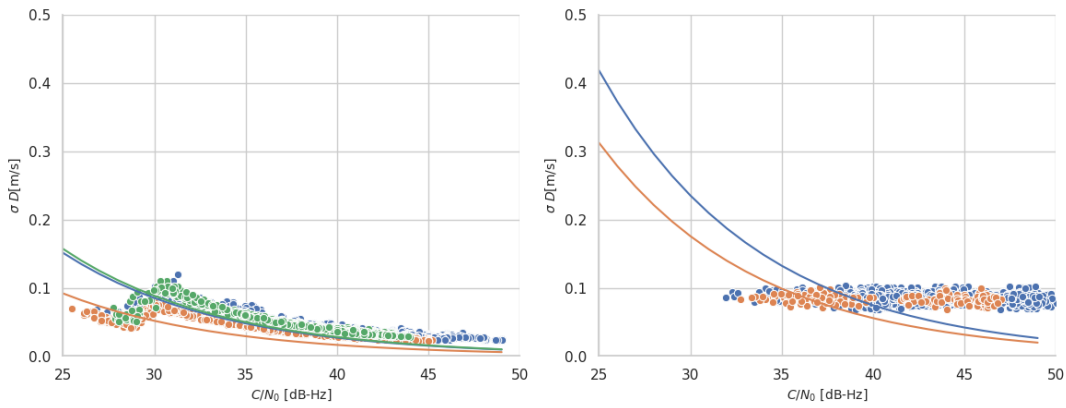

Figure 19: Computed standard deviation of Doppler observable. For two single-frequency GNSS receivers: u-blox m8t (left) and Septentrio (right). Obtained from two short baseline experiments. Using observation difference linear combination: Doppler-minus-time-differenced-carrier-phase.

Lets look at the representation of variance for the Doppler thermal noise given in Teunissen and Montenbruck [2017]:

$$\sigma_D^2 = \frac{\lambda^2}{4\pi^2 T^2} \frac{4B_{FLL}}{C/N_0}(1 + \frac{1}{TC/N_0}) \quad [(m/s)^2] \qquad (77)$$

There are two possible parameters to tune assuming we cannot change the physical components of our measurement system and obviously have no influence over the signal transmission power. Which would change the C/N_0. These are either the frequency locked loop bandwidth B_{FLL} or the coherent integration time T. Longer T and lower B_{FLL} lead to more precise Doppler measurements. However higher bandwidth leads to faster response to changes in dynamics. Because the u-blox m8t receiver is expected to cope with a large amount

of different dynamics, a higher bandwidth could be used. Exchanging accuracy for better robustness to changing dynamics.

5.6 TIME-DIFFERENCED CARRIER-PHASE

From fig. 20 the time-differenced carrier-phase shows an order of magnitude difference between both receivers. This is however in line
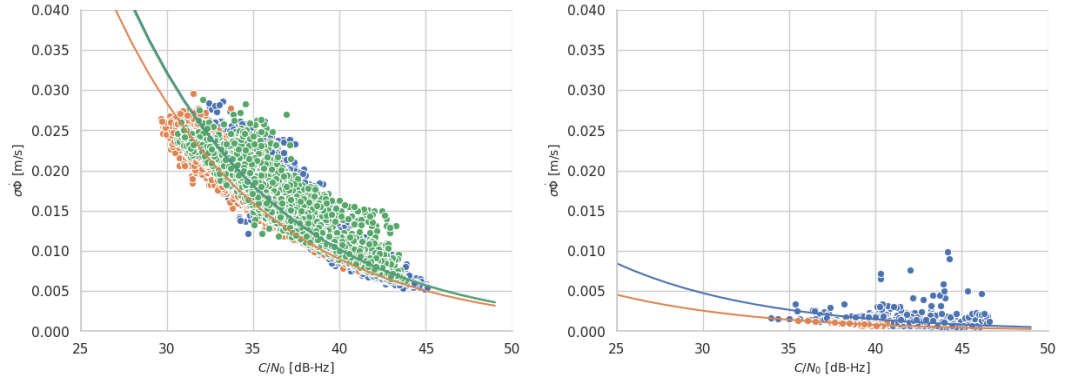

Figure 20: Computed standard deviation of time-differenced carrier-phase observable. For two single-frequency GNSS receivers: u-blox m8t (left) and Septentrio (right). Obtained from two short baseline experiments. Using double-difference linear observation combinations.

with what we expect. The expectation of variance is: $\sigma_\Phi^2 - b/2\Delta t^2$. With σ_Φ^2 the carrier-phase variance. And b the covariance between Φ_i and Φ_{i+2}. This leads to a difference in magnitude for two reasons. First the carrier-phase variance of the Septentrio AsteRx1 is lower on average compared to u-blox m8t GNSS receiver. And second, looking at the time-correlation coefficients for both receivers it becomes apparent that for AsteRx1 b has higher magnitude. Even though time-correlation fades faster for the Septentrio AsteRx1 receiver.

5.7 CARRIER-TO-NOISE DENSITY RATIO

Fig. 21 shows the carrier-to-noise density ratio standard deviation estimates. Lets first establish, to avoid confusion, that carrier-to-noise density ratio and signal-to-noise ratio are related through the receiver code bandwidth B_P:

$$10\log(\frac{S}{N}) = \frac{1}{B_P}\frac{C}{N_0} \tag{78}$$

And that we use the carrier-to-noise density ratio, as this enables us to compare between receivers independently of their architecture. Fig. 21 shows the normalized standard deviation of carrier-to-noise density ratio for both receivers. Notice that similar to the other ob-

servables, noise increases exponentially as carrier-to-noise density ratio becomes lower. This is probably due to lower elevation of satellites. Antennas are designed to behave best for satellites at zenith. A logical consequence of the signal having a non-zenith angle of incidence is lower signal magnitude.
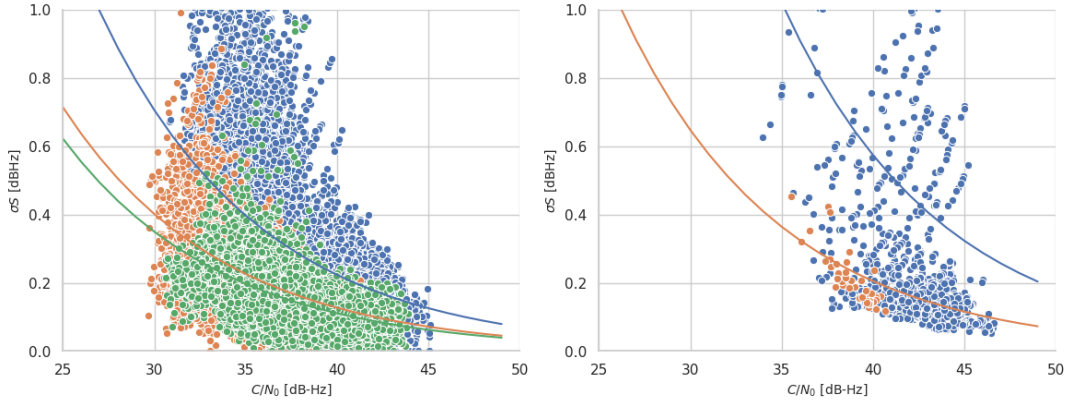

Figure 21: Computed standard deviation of time-differenced carrier-phase observable. For two single-frequency GNSS receivers: u-blox m8t (left) and Septentrio (right). Obtained from two short baseline experiments. Using double-difference linear observation combinations.

For both receivers the variation of standard deviation does not exceed 1[dB-Hz]. With added note that the u-blox neo m8t receiver has a resoluation of 1 [dB-Hz] and the AsteRX1 receiver $\frac{1}{4}$ [dB-Hz].

5.8 TIME-CORRELATION

Fig. 22 shows time-correlation of observables. For both u-blox m8t (left) and Septentrio AsteRx1 (right) GNSS receivers. Both code, carrier-phase and carrier-to-noise density ratio observables start positively time-correlated. And oscillate towards zero.

The u-blox neo m8t receiver shows stronger and longer time-correlation of code observable. Possibly using longer coherent integration time or a more narrow DLL tracking loop bandwidth. The carrier-phase time-correlation is weaker for u-blox but persists longer in comparison. The longer persistence of time-correlation is a general difference between both receivers. Using more observations in the current observation state estimate results in dampened noise due to averaging.

Receiver processing design choices could be at the root of this behavior. Users of low-cost receivers such as the u-blox m8t are generally more interested in ready-to-use position, velocity and time solutions. On the downside using more observations generally means slower response to changing user dynamics. When you hit the breaks of your car for instance if may appear as if you where still driving at higher speed. For the high-end AsteRx1 receiver on the other hand,
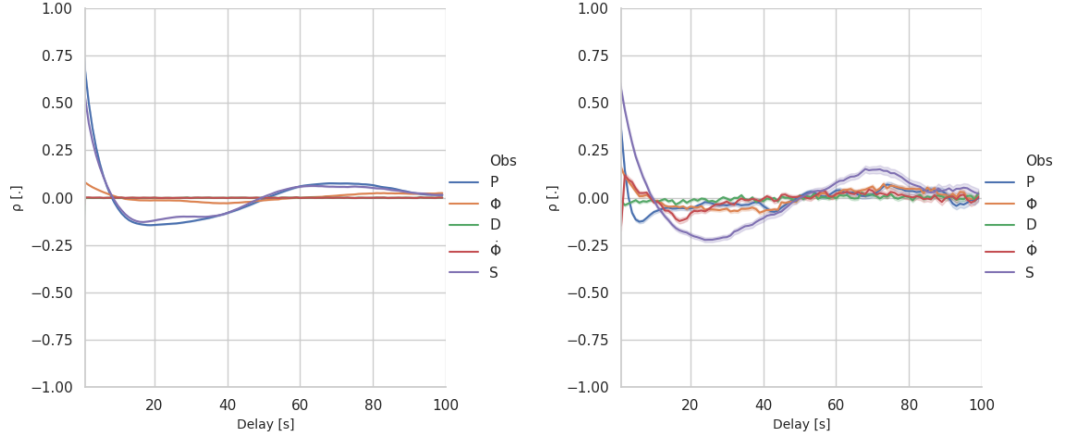
Figure 22: Computed time-correlation of code, carrier-phase, Doppler, time-differenced carrier-phase and carrier-to-noise density ratio observables. For two single-frequency GNSS receivers. Left for u-blox m8t data taken at 10[Hz]. And Septentrio AsteRx1 on the right, data taken at 1[Hz]. Computed from two short baseline experiments. Using double-difference linear observation combinations.

users are likely more interested in a raw observation state. Leaving room to apply their own filters to dampen noise if one wishes to do so.

As example consider measurement vector $\underline{y}$, with variance matrix $Q_{\underline{y}}$. And see how time-correlation propagates into state estimates:

$$
\underline{y} = \begin{pmatrix} \underline{y}_1 \\ \underline{y}_2 \\ \vdots \\ \underline{y}_{t-1} \\ \underline{y}_t \end{pmatrix}, \quad Q_{\underline{y}} \begin{pmatrix} \sigma^2 & a & & & \\ a & \sigma^2 & & & \\ & & \ddots & & \\ & & & \sigma^2 & a \\ & & & a & \sigma^2 \end{pmatrix} \tag{79}
$$

Vector $\underline{y}$ represents some time-series of measurements of the range between a stationary target and observer. Measurements are time-correlated up to one epoch, denoted by term a. Now say we want to take the moving average of measurements $\underline{y}$. Which in recursive-matrix form gives:

$$
\hat{\underline{\mu}}_t = Mp = \begin{pmatrix} \frac{t-1}{t} & \frac{1}{t} \end{pmatrix} \begin{pmatrix} \hat{\underline{u}}_{t-1} \\ \underline{y}_t \end{pmatrix} \tag{80}
$$

Where $\hat{\underline{\mu}}_t$ is the average estimate at epoch t. Propagation matrix M and p a vector with average estimate up to epoch t-1 and the measurement at epoch t. Vector p has dispersion:

$$
D \begin{pmatrix} u_{t-1} \\ y_t \end{pmatrix} = Q_p = \begin{pmatrix} \sigma^2_{\mu_{t-1}} & \frac{1}{t-1}a \\ \frac{1}{t-1}a & \sigma^2_{y_t} \end{pmatrix} \tag{81}
$$

Where $\frac{1}{t-1}a$ gets smaller as the time-series $\underline{y}$ gets larger. Because $\hat{\underline{\mu}}_{t-1}$ will depend on a larger amount of measurements that have no time-correlation with $\underline{y}_t$. Propagating variance matrix Q_p to variance of $\hat{\underline{\mu}}_t$ we get:

$$D\left(u_t\right) = MQ_pM^\mathsf{T} = \frac{(t-1)^2}{t^2}\sigma^2_{\mu_{t-1}} + \frac{1}{t^2}\sigma^2_{y_t} + (\frac{t-1}{t^3-t^2} + \frac{1}{t^2})a \quad (82)$$

Where 1) the overall variance of $\hat{\underline{\mu}}_t$ drops as time-series get longer. 2) with increasing t the estimate relies less on the current measurement $\underline{y}_t$ and more on the previous measurements. And 3) the influence of time-correlation on the estimate reduces exponentially with time. In this scenario we assumed that time-correlation will only be present between measurements of consecutive epochs. If time-correlation persists however, the propagated variance of the estimator will be higher compared to no time-correlation. As can be seen by term a in Eq. 82.

5.9 COVARIANCE

Fig. 23 shows the cross-correlation coefficients for the Septentrio AsteRx1 GNSS receiver. We see that for all combinations the correlation coefficients appear to be constant with respect to carrier-to-noise density ratio. Appearing randomly distributed, with the spread likely random measurement noise propagating into the coefficient estimates.

No correlation between observables would imply that we expect ρ to be zero and follow the Student's t distribution. Therefore our null hypothesis is given by $H_0 : \rho = 0$. And under the alternative hypothesis unequal $H_a : \rho! = 0$. With level of significance of $a_1 = 0.01$ and $a_2 = 0.05$. We see that the null-hypothesis is not rejected for all observation pairs, with exception of (Φ, D) under a_1. And that pairs (P, ϕ) and (Φ, D) correlation is more likely under a_2. Under a_2 for pair (P, Φ) H_0 is rejected. This could imply carrier aiding of DLL.

The absence of correlation between carrier-phase and time-differenced carrier-phase follows from two premises. 1) the differenced carrier-phase is obtained as function of the previous and next carrier-phase epochs. Which means that there is no direct correlation in terms of epochs between the pair. And 2) there is minimal time-correlation present on the carrier-phase observable.

Based on the findings above we assume no cross-correlation between pairs: (P, Φ), (P, D), $(P, \dot{\Phi})$, $(\Phi, \dot{\Phi})$, $(D, \dot{\Phi})$, (P, S), (Φ, S), (D, S), $(\dot{\Phi}, S)$. And a significant correlation coefficient of -0.5 between Doppler and carrier-phase: (D, Φ).

No correlation between pair (Φ, S) can be understood by looking at the transformation from Cartesian to polar coordinates. And the joint and marginal distributions that follow from the transformation.
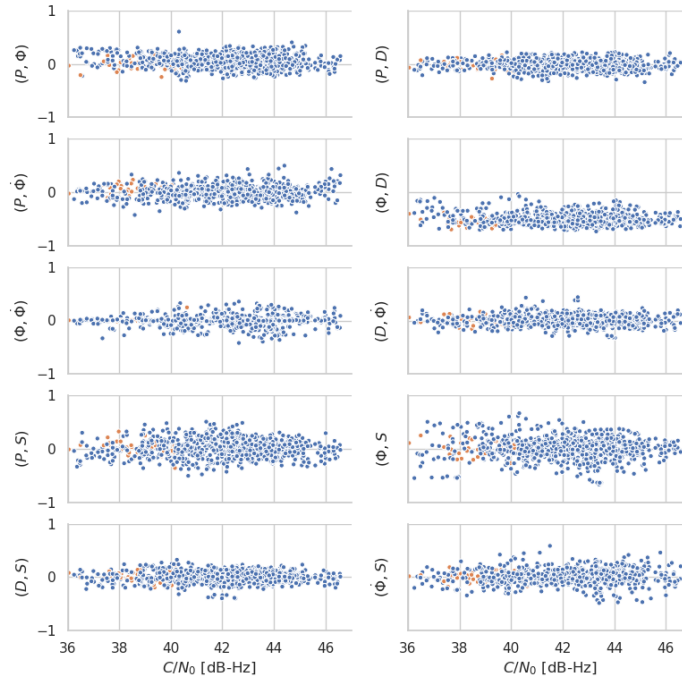
Figure 23: Computed cross-correlation of code, carrier-phase, Doppler and time-differenced carrier-phase observables. For Septentrio single-frequency GNSS receiver. Computed from a short baseline experiment. Using double-difference linear observation combinations.

Given two independent and identically distributed zero-mean normal random variables $\underline{x}_1$ and $\underline{x}_2$. And transformation:

$$\underline{y}_1 = \sqrt{\underline{x}_1^2 + \underline{x}_2^2}, \qquad \underline{y}_2 = \angle(\underline{x}_1, \underline{x}_2) \tag{83}$$

It can be shown that $\underline{y}_1$ and $\underline{y}_2$ are independent by virtue of their marginal distributions Teunissen et al. [2006](pp.75):

$$f_{\underline{y}_1}(y_1) = \frac{y_1}{\sigma^2}\exp(\frac{y_1^2}{2\sigma^2}), \quad y_1 \geqslant 0, \quad \text{and} \quad f_{\underline{y}_2}(y_2) = \frac{1}{2\pi}, \quad y_2 \in [0, 2\pi) \tag{84}$$

A receiver model can be interpreted in the same simplified way. Correlating the incoming signal with a sine and cosine function enables for estimating magnitude and phase of the signal. Applying the transformation above results in independent variables.

The correlation coefficient estimates of the u-blox NEO m8t GNSS receiver are shown in Fig. 24. Again the correlation coefficients appear stationary with respect to carrier-to-noise density ratio. We again test for significant non-zero correlations. Following the same approach as

for the AsteRx1 receiver. For both chosen levels of significance H_0 is rejected for pairs: (P, Φ), (Φ, D), and $(D, \dot{\Phi})$. The correlation between code and carrier-phase, upper-left figure, is centered around zero, randomly spreading in both directions. This could again imply carrier-aiding of the DLL. But on average we assume that the correlation between these two observations is averaged out over time. And therefore neglected. The upper-right figure shows the correlation co-
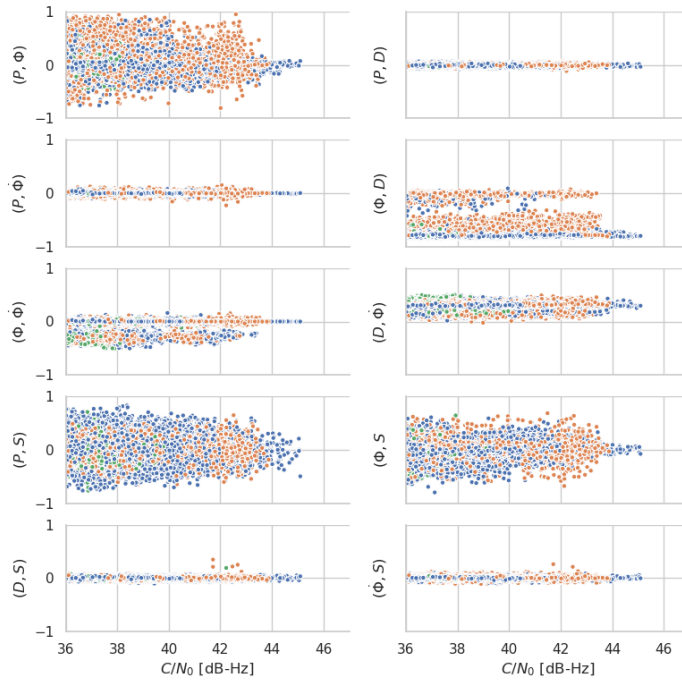

Figure 24: Computed crosscorrelation of code, carrier-phase, Doppler and time-differenced carrier-phase observables. For u-blox m8t single-frequency GNSS receiver. Computed from a short baseline experiment. Using double-difference linear observation combinations.

efficient as computed between code and Doppler. There is no visible correlation. The code state is therefore likely not steered by the state of Doppler in any way.

Now lets focus on the correlation between pair carrier-phase and Doppler. Depending on receiver architecture we expect no or very small correlation for first-order phase-lock loop. And either positive or negative correlation for second or higher order type loops. With the sign depending on the type of feedback used in the system. In the figure we see two distinct signals. No correlation and a negative correlation with mean around -0.8 [-]. The segments that show no correlation need some further explanation.

To remove any trend still present after double-differencing a low-order polynomial is used. These trends can for instance be caused

by low frequency multipath. If we do not detect a cycle slip within a segment, the estimated polynomial will attempt to mold itself after these jumps in the data. By their very nature polynomials do not cope well with jumps, but rather smooth patterns. Such as satellite orbital motion for instance. So if we miss a cycle slip we bias our segment by means of a polynomial. Cycle slips do not occur in Doppler observations. This means that if a cycle slip occurs the polynomial has potential to change the correlation between both observables. We can put this hypothesis to the test by making our cycle slip detection more strict. We therefore change the detectors treshold from the original 1λ to 0.5λ and $0.4\lambda[m]$. With λ being the carrier wavelength, at L1 this is 0.1905 [m]. It turns out that if we look at the fractions between both pointclouds we see that almost all zero-correlations are removed. Making it likely that there exist a negative feedback look in the PLL between carrier-phase and Doppler observables.

The pair carrier-phase and time-differenced carrier-phase are negatively correlated. When propagating a small example of four epochs of carrier-phase observables we see that in theory there is no correlation between Φ_n, $\dot{\Phi}_n$ and D_n. If we have expectation of observations:

$$
E
\begin{pmatrix}
\Phi_1 \\ \Phi_2 \\ \Phi_3 \\ \Phi_4 \\ \dot{\Phi}_2 \\ \dot{\Phi}_3 \\ D_1 \\ D_2 \\ D_3 \\ D_4
\end{pmatrix}
=
\begin{pmatrix}
1 & & & & & & & & & \\
& 1 & & & & & & & & \\
& & 1 & & & & & & & \\
& & & 1 & & & & & & \\
-\frac{1}{2\Delta t} & 0 & \frac{1}{2\Delta t} & & & & & & & \\
& -\frac{1}{2\Delta t} & 0 & \frac{1}{2\Delta t} & & & & & & \\
& & & & 1 & & & & & \\
& & & & & 1 & & & & \\
& & & & & & 1 & & & \\
& & & & & & & 1 & &
\end{pmatrix}
\begin{pmatrix}
\Phi_1 \\ \Phi_2 \\ \Phi_3 \\ \Phi_4 \\ D_1 \\ D_2 \\ D_3 \\ D_4
\end{pmatrix}
\tag{85}
$$

With dispersion excluding time-differenced carrier-phase:

$$
D
\begin{pmatrix}
\Phi_1 \\ \Phi_2 \\ \Phi_3 \\ \Phi_4 \\ D_1 \\ D_2 \\ D_3 \\ D_4
\end{pmatrix}
=
\begin{pmatrix}
\sigma_\Phi^2 & a & b & c & d & e & f & g \\
a & \sigma_\Phi^2 & a & b & e & d & e & f \\
b & a & \sigma_\Phi^2 & a & f & e & d & e \\
c & b & a & \sigma_\Phi^2 & g & f & e & d \\
d & e & f & g & \sigma_D^2 & 0 & 0 & 0 \\
e & d & e & f & 0 & \sigma_D^2 & 0 & 0 \\
f & e & d & e & 0 & 0 & \sigma_D^2 & 0 \\
g & f & e & d & 0 & 0 & 0 & \sigma_D^2
\end{pmatrix}
\tag{86}
$$

Propagating variance gives the following full variance matrix where we have included $\dot{\Phi}$.

$$
\begin{pmatrix}
\sigma_\Phi^2 & a & b & c & \frac{b-\sigma_\Phi^2}{2\Delta t} & \frac{c-a}{2\Delta t} & d & e & f & g \\
a & \sigma_\Phi^2 & a & b & 0 & \frac{b-\sigma_\Phi^2}{2\Delta t} & e & d & e & f \\
b & a & \sigma_\Phi^2 & a & \frac{\sigma_\Phi^2-b}{2\Delta t} & 0 & f & e & d & e \\
c & b & a & \sigma_\Phi^2 & \frac{a-c}{2\Delta t} & \frac{\sigma_\Phi^2-b}{2\Delta t} & g & f & e & d \\
\frac{b-\sigma_\Phi^2}{2\Delta t} & 0 & \frac{\sigma^2-b}{2\Delta t} & \frac{a-c}{2\Delta t} & \frac{\sigma_\Phi^2-b}{2\Delta t^2} & \frac{a-c}{4\Delta t^2} & \frac{f-d}{2\Delta t} & 0 & \frac{d-f}{2\Delta t} & \frac{e-g}{2\Delta t} \\
\frac{c-a}{2\Delta t} & \frac{b-\sigma_\Phi^2}{2\Delta t} & 0 & \frac{\sigma_\Phi^2-b}{2\Delta t} & \frac{a-c}{4\Delta t^2} & \frac{\sigma_\Phi^2-b}{2\Delta t^2} & \frac{g-e}{2\Delta t} & \frac{f-d}{2\Delta t} & 0 & \frac{d-f}{2\Delta t} \\
d & e & f & g & \frac{f-d}{2\Delta t} & \frac{g-e}{2\Delta t} & \sigma_D^2 & 0 & 0 & 0 \\
e & d & e & f & 0 & \frac{f-d}{2\Delta t} & 0 & \sigma_D^2 & 0 & 0 \\
f & e & d & e & \frac{d-f}{2\Delta t} & 0 & 0 & 0 & \sigma_D^2 & 0 \\
g & f & e & d & \frac{e-g}{2\Delta t} & \frac{d-f}{2\Delta t} & 0 & 0 & 0 & \sigma_D^2
\end{pmatrix}
\tag{87}
$$

As we can see there is covariance between Φ_n and $\dot{\Phi}_{n\pm1}$: $b-\sigma_\Phi^2$ and $\sigma_\Phi^2 + b$. So by virtue of time-correlation we expect small correlation both positive and negative. The majority of samples fall in line with this expectation.
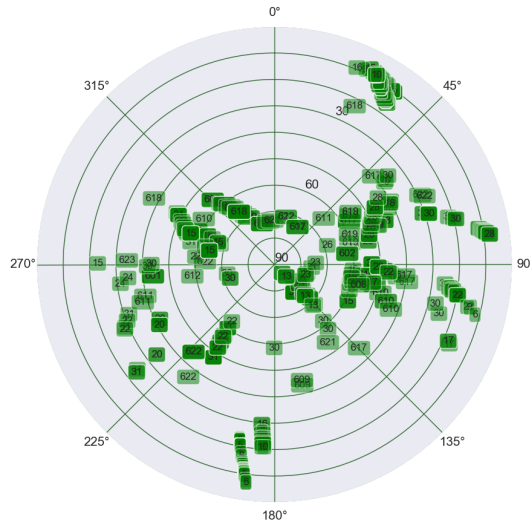
Figure 25: Azimuth-elevation plot of those DD segments that show negative correlation between Φ and $\dot{\Phi}$.

However, a small number of samples show a negative correlation. Two candidates causing this behavior were investigated.

1) High-frequency multipath could cause a strong time-dependent correlation on phase observables. With a repeating pattern as orbits repeat. Leading to a higher impact of time-correlation and thereby to a higher negative correlation between phase and differenced phase.

This implies that a receiver-site-satellite specific geometry causes correlation. Fig. 25 shows an azimuth-elevation plot of just the samples that show negative correlation. No apparent trend is visible. 2) Another possibility would be that the variance or time-correlation is significantly higher for these samples. Looking at both quantities for these samples shows that this is not the case.

Finally lets focus on pair Doppler and time-differenced carrier-phase. From the propagated variance matrix in Eq. 87 we see that the covariance between pair $(D_{n\text{-}1}, \dot{\Phi}_n)$ is: $\frac{f\text{-}d}{2\Delta t}$. With d the covariance between pairs $(D_n \Phi_n)$ and f between pairs: $(D_{n\text{-}1} \Phi_n)$. Remember that we did not see any correlation between this observation pair for the Septentrio AsteRx1 receiver. This difference could be explained by the fact that there is stronger correlation between (D, Φ) for the u-blox m8t GNSS receiver. But this correlation fades faster with time compared to the AsteRx1 receiver.

RESULTS

6.1 INTRODUCTION TO STATE ESTIMATION

In this chapter we detail and interpret state estimation results from the conducted experiments. There are three experiments: 1) A short-baseline installment consisting of two receivers on the roof of the TU Delft GNSS Observatory, The Netherlands. 2) Two buoys freely drifting in the North-Sea near the shore of Scheveningen, The Netherlands. And 3) two receivers mounted on a car driving a regional road East of Delft, The Netherlands. For an in depth description of these experiments the reader is referred to Ch. 4.

All experiments use identical hardware, on which a brief discussion is provided in appendix A. All receivers have been configured to measure available GPS, Galileo and GLONASS satellite signals at 10[Hz]. Measurement vector y consists for each satellite of code, carrier-phase and Doppler or time-differenced carrier phase measurements. Code and carrier-phase measurements and their respective observation equations are detailed in Ch. 2. Doppler and time-differenced carrier-phase measurements are described in Ch. 3. We estimated the variance model for individual observables and the correlation between them; all based on the short-baseline experiment. The resulting variance model is detailed in Ch. 5.

Position and velocity state estimates were obtained from processing the measurements from the above mentioned experiments. Multiple processing strategies were used. Commonalities between these strategies are described in appendix F. Differences arise by choosing what constellations to use (GPS, Galileo and/or GLONASS), by choosing the type of stochastic model, either: the one used by de Bakker and Tiberius [2017] or the one developed in this work. And finally by what velocity observable to use, either Doppler or time-differenced carrier-phase.

All Doppler based experiments are processed with both stochastic models mentioned above. The time-differenced carrier-phase models are only processed using the stochastic model developed in this work. Both the short-baseline static and drifting buoy experiments are processed using GPS, GPS+Galileo and GPS+Galileo+GLONASS. Which leads to nine different sets of state estimation results. The regional road experiment is processed using GPS only, totaling three different state estimate results.

For a thorough discussion on evaluation measures on accuracy, precision and reliability the reader is referred to Ch.4. Next we will first

make a note on the interpretation of the a-priori and empirical confidence region. Thereafter an overview of estimation results is discussed using two tables: position and velocity. Where we will discuss general trends in terms of precision and accuracy. We conclude by detailing interesting aspects of the individual experiments; where we show these through horizontal scatter plots of North and East component state estimates-minus-ground-truth.

6.2   A-PRIORI AND EMPIRICAL CONFIDENCE REGIONS

The a-priori confidence region follows from the A and Q_y matrices as shown in Eq. 6. For each experiment set A and Q_y are taken from the middle epoch of an experiment. Where we chose to take both A and Q_y after the DIA procedure in order to be as comparable as possible to the empirical estimate of Q_x. The empirical confidence region is computed from position and velocity state estimates using estimates for the variance and covariance from Ch. 5 and Eq. 68.

The formal- and empirical confidence regions may not fully match. This can be a direct result of the geometry in A for the center epoch differing somewhat from the geometry at another epoch in the experiment. Furthermore Q_y can for each individual satellite be optimistic or pessimistic; which is in large part depending on the stochastic model. Then when propagating Q_y to Q_x the dimensions go from m measurements to n unknown variables, where often $m > n$. Depending on the ensemble of individual mismatches it leads to Q_x being also either pessimistic or optimistic. Which will result in a scaling of a-priori with respect to the empirical confidence region.

We expect satellite geometry to play a central role in the behavior of horizontal error components. As becomes apparent the confidence regions are mostly elongated in the North direction. Meaning the North component is less precise than the East component. This is a direct consequence of GNSS satellite groundtracks and the experiment latitude of 52 degrees. Analogous would be the following. Imagine an empty a small room with no lights and a vase in the middle. You are asked to install lights such that shadows are minimized. And no lights is no option. It will take at least a few lights at different positions to get rid of all the shadows perceived by the human eye. Satellites are no different in that it also results in a play of angles and illumination.

6.3   EXPERIMENT PRECISION AND ACCURACY OVERVIEW

Here we give an overview of horizontal RMSE, horizontal bias and horizontal standard deviations for all different processing settings. The first column denotes aspects of the experiment configuration, namely: platform, velocity observable, stochastic model. The velocity

observable is as discussed either Doppler (D) or time-differenced carrier phase ($\dot{\Phi}$). And stochastic model either elevation (ele) or C/N_0 (cnr) based. For the buoy experiments the subscripts denote: ⊗$_{2,1}$ (buoy 2, morning experiment) and ⊗$_{1,2}$ (buoy 1, afternoon experiment).

6.3.1 Experiment Position State Estimate Accuracy and Precision

Tab. 7 shows the mentioned experiment results for horizontal position state estimates for all experiments. In terms of accuracy the second column shows the horizontal RMSE. Where the horizontal RMSE stays within the 0.5[m] threshold for the full static experiment. With elevation based model performing best. For the kinematic experiments only the afternoon drifting buoy experiments, denoted by subscript 2, are over the 0.5[m] threshold by a small margin. The morning experiment, second subscript 1, shows worse results and has lower accuracy because the state of the sea was rougher.

6.3.2 Experiment Velocity State Estimate Accuracy and Precision

Tab. 8 shows the mentioned experiment results for horizontal velocity state estimates for all experiments. In terms of accuracy the horizontal RMSE stays within the threshold of 0.1[m/s] for all experiment configurations with the static receiver on rooftop and car on a regional road experiments. With the use of the time-differenced carrier phase observable the accuracy is almost twice as good compared to using the Doppler observable. For the drifting buoy experiment only the time-differenced carrier phase observable stays within the threshold of 0.1[m/s].

6.4 STATIC RECEIVER ON ROOF TU DELFT GNSS OBSERVATORY

State estimation results are represented through nine subfigures. Each subfigure represents one set of state estimates according to the settings described in the introduction to this chapter. The columns denote the used variance model, either elevation or C/No-based, and velocity observable, either Doppler or time-differenced carrier phase. And rows refer to the used constellations (GPS, GPS and Galileo, and GPS, Galileo and Glonass). The blue dots represent horizontal position estimates relative to a known reference. The a-priori (95=red) and empirical (95=solid-black, 99=striped-black) percent confidence regions are also visualized.

Experiment site | vobs | Q_y	Horizontal RMSE [m]	b_n [m]	b_e [m]	$\hat{\sigma}_n$ [m]	$\hat{\sigma}_e$ [m]	$\hat{\rho}_{ne}$ [-]
🏢 | D | ele	0.429	-0.392	0.164	0.043	0.023	-0.015
🏢 | D | cnr	0.483	-0.451	0.090	0.104	0.061	0.007
🏢 | $\dot{\Phi}$ | cnr	0.484	-0.452	0.090	0.104	0.061	0.007
⊕$_{1,1}$ | D | ele	0.771	-0.268	-0.325	0.457	0.267	0.441
⊕$_{1,1}$ | D | cnr	0.792	-0.295	-0.320	0.468	0.289	0.329
⊕$_{1,1}$ | $\dot{\Phi}$ | cnr	0.812	-0.313	-0.305	0.484	0.292	0.336
⊕$_{2,1}$ | D | ele	0.725	-0.173	-0.144	0.487	0.268	0.355
⊕$_{2,1}$ | D | cnr	0.772	-0.224	-0.150	0.512	0.326	0.357
⊕$_{2,1}$ | $\dot{\Phi}$ | cnr	0.781	-0.218	-0.134	0.522	0.326	0.337
⊕$_{1,2}$ | D | ele	0.507	0.259	-0.212	0.269	0.189	0.179
⊕$_{1,2}$ | D | cnr	0.504	0.120	-0.201	0.316	0.224	0.110
⊕$_{1,2}$ | $\dot{\Phi}$ | cnr	0.529	0.156	-0.210	0.325	0.228	0.009
⊕$_{2,2}$ | D | ele	0.530	0.232	-0.164	0.316	0.204	-0.185
⊕$_{2,2}$ | D | cnr	0.507	0.090	-0.160	0.334	0.204	-0.000
⊕$_{2,2}$ | $\dot{\Phi}$ | cnr	0.507	0.088	-0.163	0.334	0.213	0.045
🚗 | D | ele	0.717	0.632	-0.066	0.235	0.177	-0.283
🚗 | D | cnr	0.684	0.595	-0.051	0.236	0.176	-0.204
🚗 | $\dot{\Phi}$ | cnr	0.682	0.592	-0.053	0.237	0.176	-0.222

Table 7: Horizontal position accuracy overview, GPS only. First column denotes the experiment. Given three variables. 1) the site: 🏢=roof,⊕=buoy(number,morning/afternoon),🚗=car,✈=uav. 2) the velocity observable used, either Doppler (D) or time-differenced carrier phase ($\dot{\Phi}$). 3) and finally the variance model used, either elevation (ele)- or C/N_0 (cnr) based. The second column denotes the horizontal RMSE. Two following columns the horizontal East and North bias components (b_n, b_e). The final three columns denote the North and East component standard deviation ($\hat{\sigma}_n$), $\hat{\sigma}_e$) and the correlation between the two ($\hat{\rho}_{ne}$).

6.4.1 Position in the Static Rover Case

Horizontal position components are shown in Fig. 26. The GPS-only elevation based processing of Doppler measurement performs best. With a bias of around -0.4[m] and 0.16[m] in North and East directions. Standard deviation of 0.04[m] and 0.02[m] in North and East direction. And a correlation coefficient of -0.015. The bias for the C/N_0 based model is slightly worse in North component: 5.9[cm], but better in East component by 7.4[cm]. As are the horizontal sample standard deviations North an East by 0.1[m] and 0.06[m] respectively.

Experiment site | vobs | Q_y	Horizontal RMSE [m/s]	b_{dn} [m/s]	b_{de} [m/s]	$\hat{\sigma}_{dn}$ [m/s]	$\hat{\sigma}_{de}$ [m/s]	$\hat{\rho}_{dne}$ [-]
▦ | D | ele	0.033	0.001	0.002	0.023	0.016	-0.073
▦ | D | cnr	0.030	-0.002	0.002	0.022	0.016	-0.068
▦ | $\dot{\Phi}$ | cnr	0.014	0.001	0.001	0.010	0.007	-0.041
$\otimes_{1,1}$ | D | ele	0.122	-0.002	-0.000	0.086	0.077	-0.124
$\otimes_{1,1}$ | D | cnr	0.111	-0.001	-0.001	0.079	0.075	-0.137
$\otimes_{1,1}$ | $\dot{\Phi}$ | cnr	0.068	-0.002	0.002	0.048	0.035	0.159
$\otimes_{2,1}$ | D | ele	0.122	-0.005	0.002	0.086	0.078	0.004
$\otimes_{2,1}$ | D | cnr	0.116	-0.002	0.002	0.082	0.074	-0.037
$\otimes_{2,1}$ | $\dot{\Phi}$ | cnr	0.064	-0.004	0.003	0.045	0.036	0.114
$\otimes_{1,2}$ | D | ele	0.113	0.000	0.001	0.080	0.077	-0.021
$\otimes_{1,2}$ | D | cnr	0.110	-0.001	0.002	0.078	0.076	-0.047
$\otimes_{1,2}$ | $\dot{\Phi}$ | cnr	0.067	-0.002	0.001	0.047	0.032	-0.016
$\otimes_{2,2}$ | D | ele	0.110	0.001	0.002	0.078	0.078	-0.034
$\otimes_{2,2}$ | D | cnr	0.107	-0.000	0.002	0.076	0.077	-0.081
$\otimes_{2,2}$ | $\dot{\Phi}$ | cnr	0.059	-0.000	0.001	0.042	0.030	-0.058
🚗 | D | ele	0.061	0.001	0.001	0.043	0.030	-0.001
🚗 | D | cnr	0.064	-0.001	0.001	0.045	0.030	0.062
🚗 | $\dot{\Phi}$ | cnr	0.044	0.000	0.001	0.031	0.021	-0.099

Table 8: Horizontal velocity accuracy overview, GPS only. See Fig. 7. With the addition that d in the subscripts indicates that we are talking about horizontal velocities and not positions.

6.4.1.1 *Precision of BLUE Estimator for Added Satellite Measurements*

The BLUE estimator becomes more precise by using more measurements. This line of reasoning holds when unknown parameter vector x remains the same, more measurements become available in vector y and with that A and Q_y in Eq. 7 change. In the GPS-only case, adding another satellite adds an unknown carrier-phase (float) ambiguity parameter plus two range and one range-rate related measurements: code, carrier-phase and Doppler. Where the carrier-phase ambiguity parameter is assumed constant and therefore its estimator becomes more precise over time. Adding a satellite of another constellation also adds one inter-system bias parameter for the whole constellation, see Eq. 56. So here not only our model gets compromised by another carrier-phase ambiguity. The inter-system bias weakens the solution, unless this can be overcome by adding enough satellites of the other constellations.
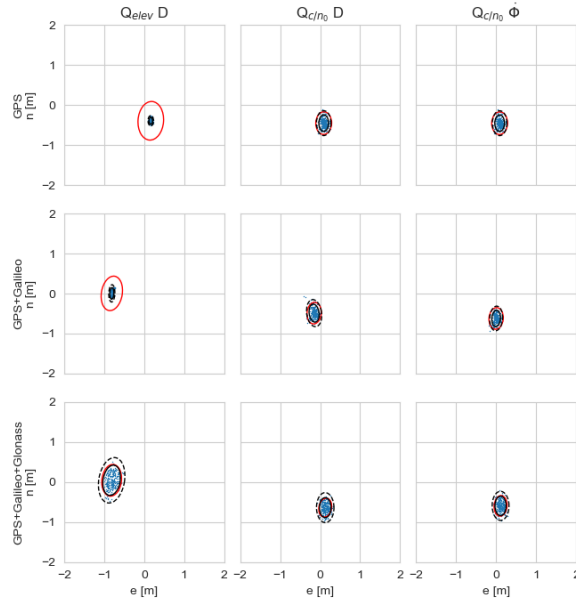
Figure 26: Horizontal **position** component estimates North and East, with respect to the ground truth. Data obtained using a static single frequency ublox neo m8t receiver. Setup on rooftop of TU Delft GNSS Observatorium. The nine sub-figures represent a combination of different constellations as rows. With either GPS only, GPS+GALILEO and GPS+GALILEO+GLONASS. And columns represent three different combinations. Doppler with elevation-based variance, Doppler with C/N_0-based variance, and TDCP with C/N_0-based variance

6.4.1.2 *Variance Models and Low Elevation Satellites*

The elevation based variance model outperforms the carrier-to-noise density based variance model in terms of precision as represented through the empirical confidence region. This can be explained by the nature of both models. The elevation based model is very pessimistic about satellites at low elevation. Whereas the carrier-to-noise density based models assigns more merit to these measurements. The low elevation satellites are prone to not take into account effects such as multipath. We have also shown from the short-baseline experiments that the receiver adjusts its signal processing parameters for both Code and Doppler observations when the satellite gets a lower C/No, and corresponding elevation (see Ch. 5 for in depth discussion of this effect). Possibly to aid with tracking the carrier-phase. Both variance models are incapable in a mathematical sense of taking this effect properly into account. Therefore the difference between the 95-percent a-priori and empirical confidence ellipses in especially the first two columns of Fig. 26 could originate from how low-elevation satellites are weighed in Q_y.

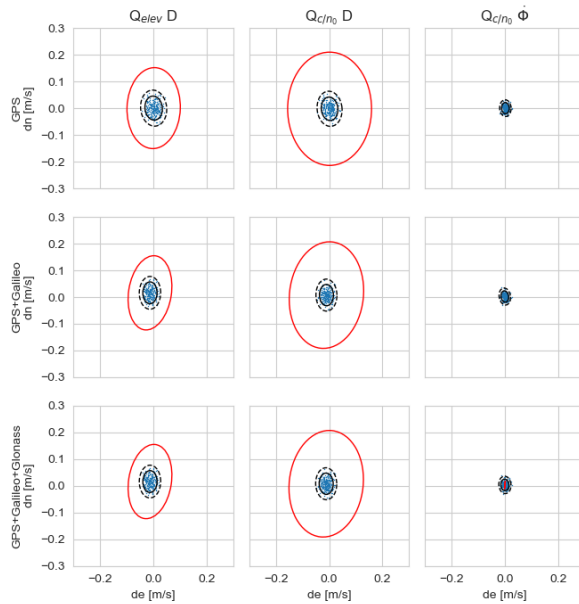### 6.4.2 Velocity in the Static Rover Case

Figure 27: Horizontal **velocity** component estimates in local North and East. See caption Fig. 26

Fig. 27 shows the velocity results for the short-baseline experiment. As expected and shown in column 3 of this figure and in overview tab. 8 the time-differenced carrier phase results in more accurate horizontal velocity error components compared to using Doppler measurements. Where the Doppler+elevation and Doppler+C/N_0 based processing have RMSE of 0.033[m/s] and 0.03[m/s] respectively. And the time-differenced carrier-phase + C/N_0 based processing has RMSE of 0.014[m/s]. All well within margins of required horizontal accuracy of 0.1[m/s].

In the static rover case there is no added benefit using multi-constellation measurements. Nor is there any noticeable downside either other than a small difference in bias in the order of 0.01 [m/s].

6.5 BUOY DRIFTING IN COASTAL AREA SCHEVENINGEN

The drifting buoy experiment is explained in Ch. 4. The experiment was divided into a morning- and afternoon session. There was a definite difference in significant wave height and surface current velocity. With rougher state of the sea surface in the morning.

6.5.1 Position in the Drifting Buoy Case

The morning horizontal positioning results for the drifting buoy experiments are shown by Figs. 28 and 29 for buoy 1 and 2 respectively.
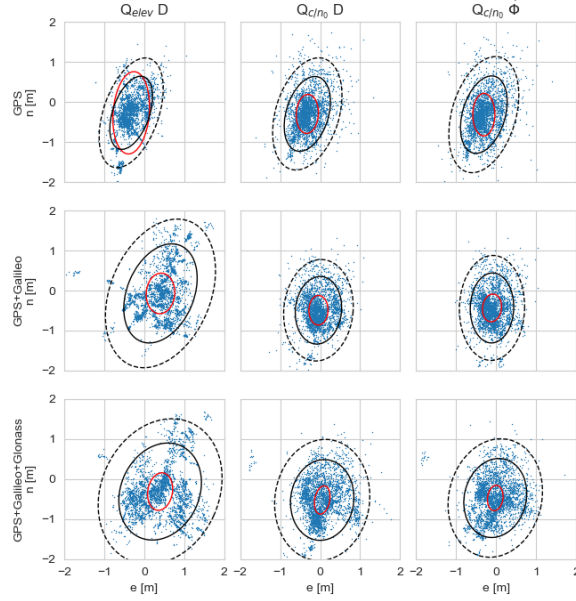
Figure 28: Horizontal **position** component estimates in local North and East for buoy 1, morning experiment. Referenced to real-time kinematic estimates using a high-end basestation on shore. Data obtained using a single frequency ublox neo m8t receiver. Mounted on a freely drifting buoy at Scheveningen coastal area. See Fig. 26

The bias in North component is better compared to the static experiment, the East component is worse.

The North and East horizontal standard deviations in the GPS-only case are comparable for all models, with the elevation based variance model slightly outperforming the rest. The North position component standard deviation was 0.457[m] and East 0.267[m] for buoy 1. And the North and East standard deviation for buoy 2 were 0.487[m] and East 0.268[m] respectively for buoy 2.

The horizontal position components for the afternoon experiments are shown in Figs. 30 and 31 for buoy 1 and 2. Here the The North and East horizontal standard deviations in the GPS-only case are again better for the elevation based variance model, slightly outperforming the rest. North position component standard deviation was 0.269[m] and East 0.189[m] for buoy 1. The North and East standard deviation for buoy 2 are 0.316[m] and East 0.204[m] respectively for buoy 2. Well within the 0.5[m] horizontal position margins of error.

The differences between morning and afternoon session horizontal position components are remarkable. This most likely is caused by the calmer state of the North-sea. Fewer waves washing over the buoy, that would lead to disturbances in signal tracking. And and less bobbing, that leads to more fluctuating antenna orientations, for which our stochastic models are not accounting for. It is of interest to see that it seems there is a slight benefit using Galileo alongside
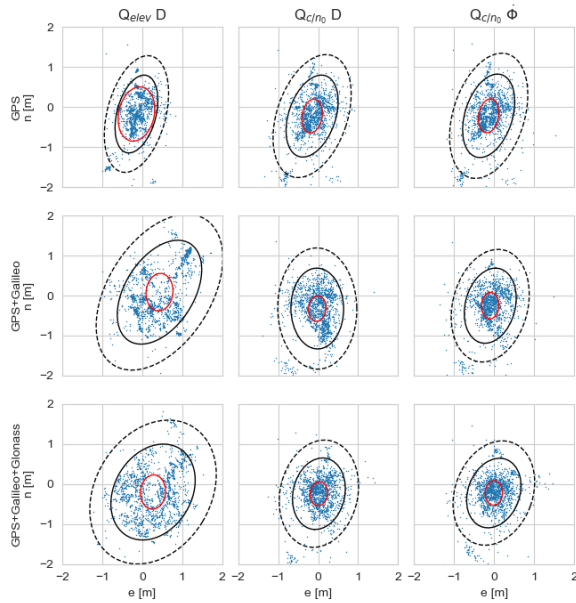
Figure 29: Horizontal **position** component estimates in local North and East for buoy 2, morning experiment. See caption Fig. 28
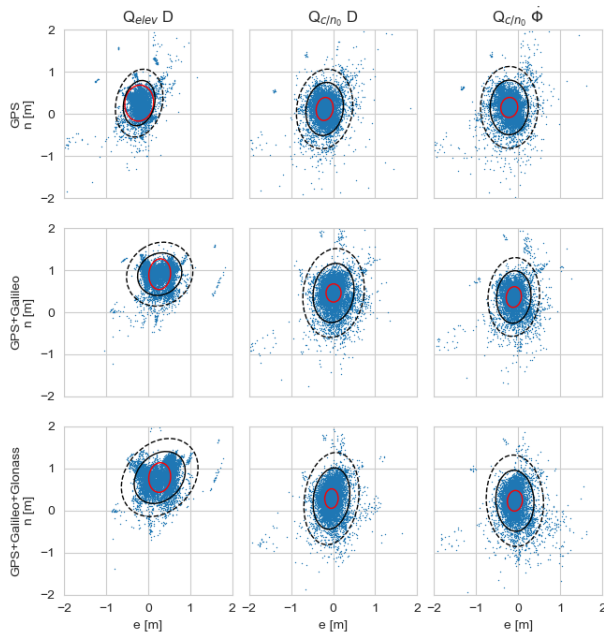

Figure 30: Horizontal **position** component estimates in local North and East for buoy 1, afternoon experiment. See caption Fig. 28

GPS measurements when in rougher waters. Especially when using the carrier-to-noise density variance based model. This latter can be attributed by the fact that as mentioned earlier this model has more confidence in lower elevation satellites, which may benefit state esti-
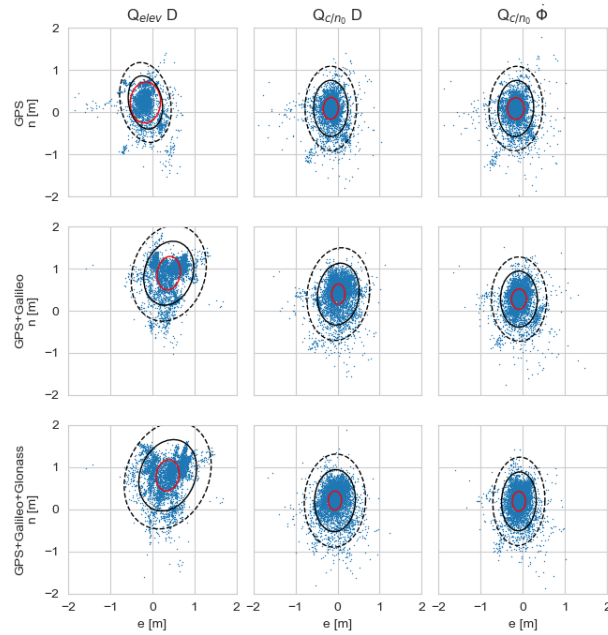
Figure 31: Horizontal **position** component estimates in local North and East for buoy 2, afternoon experiment. See caption Fig. 28

mates. It can be expected that multipath plays at least some role in degrading the signal quality. Adding more satellites may reduce its influence by 'averaging' with non- or less effected satellites.

6.5.2   Velocity in the Drifting Buoy Case

Velocity results for the morning drifting buoy session are shown in Figs. 32 and 33. Similar to the rooftop experiment, results based on Doppler are less precise compared to those based on the time-differenced carrier phase. This follows from the receiver signal processing described in the velocity literature review in Ch. 3, which showed that the time-differenced carrier phase is computed over a longer time period compared to that of the Doppler observable.

The bias for both horizontal velocity error components is in the order millimeter per second. The time-differenced carrier phase based velocity estimates outperform the Doppler based velocity estimates by a factor of 2.0 in terms of precision, also shown in tab. 8 which is in line with the static experiment. With North and East standard deviation components of 0.048 and 0.035 [m/s], and 0.045 and 0.036 [m/s] for buoy 1 and 2 respectively. Here the Doppler based velocity components with the carrier-to-noise density variance model slightly outperform the elevation based model at 0.079, 0.075 and 0.082, 0.074 [m/s] for buoy 1 and 2. Which for the rough sea state means that only
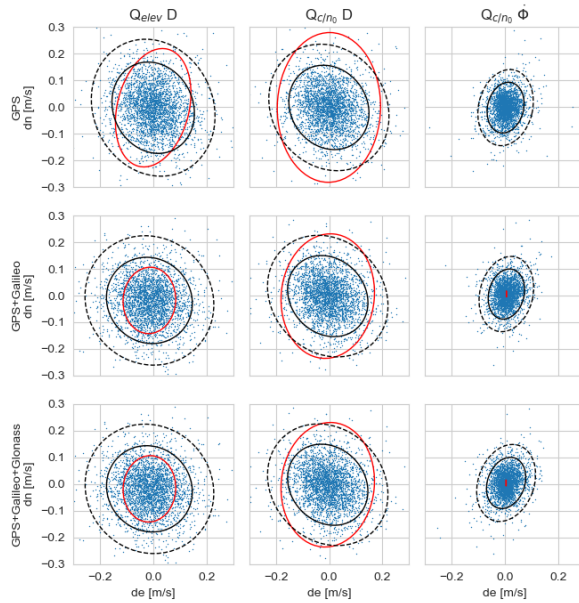
Figure 32: Horizontal **velocity** component estimates in local North and East for buoy 1, morning experiment. See caption Fig. 28

the time-differenced carrier phase velocity estimate meets the aimed at 0.1[m/s] horizontal velocity error margin.
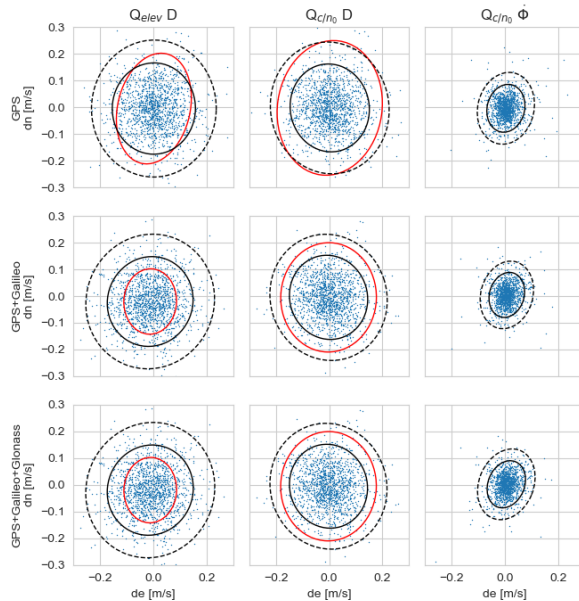

Figure 33: Horizontal **velocity** component estimates in local North and East for buoy 2, morning experiment. See caption Fig. 28

Velocity results for afternoon drifting buoy session are shown in Figs. 34 and 35. The calmer sea state leads to better velocity results for all models. Albeit smaller compared to the position improvements.

Which may reinforce our preceding observation from literature that multipath is not as much a factor for velocity based measurements.

The North and East component standard deviations are 0.047 and 0.032 [m/s] and 0.042 and 0.030 [m/s] for buoy 1 and 2 respectively. Again the Doppler based velocity components under the carrier-to-noise density variance model slightly outperform the elevation based model at 0.078, 0.076, and 0.076, 0.077 [m/s] for buoy 1 and 2. Which also for the calm sea state means that only the time-differenced carrier phase velocity estimate meets the aimed at 0.1[m/s] horizontal velocity error margin.
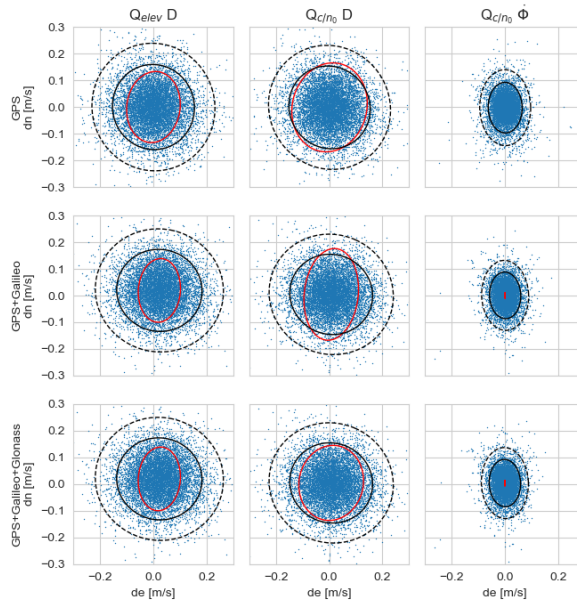

Figure 34: Horizontal **velocity** component estimates in local North and East for buoy 1, afternoon experiment. See caption Fig. 28

6.5.3 Internal and External Reliability in the Drifting Buoy Case

The reliability of our estimates is captured by the internal- and external reliability, where we set $\alpha_0 = 0.01$ and $\gamma_0 = 0.8$. As described in the last section of Ch. 2.

6.5.3.1 Internal Reliability: Code, Carrier-phase, Doppler (and Ambiguity) Measurements

Fig. 36 shows the internal reliability of our measurements as a histogram in the GPS-only case. For each individual observation per epoch the largest bias is taken as we are interested in the worse-case scenario. The x-axis denotes the MDB_1, the y-axis the count. In total the MDB_1 of four measurements are shown by the four subfigures. The ambiguity estimate up to this epoch, Code, carrier phase and
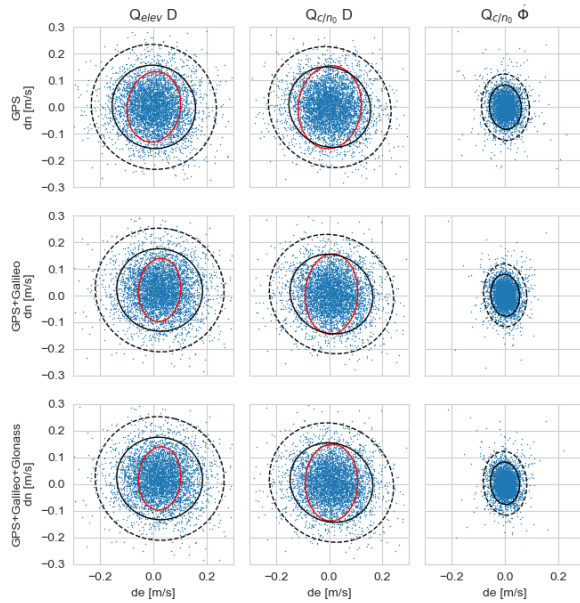
Figure 35: Horizontal **velocity** component estimates in local North and East for buoy 2, afternoon experiment. See caption Fig. 28

velocity observable: either time-differenced carrier phase or Doppler. Here ambiguities of previous epochs are taken into account for it includes effects like cycle slips.
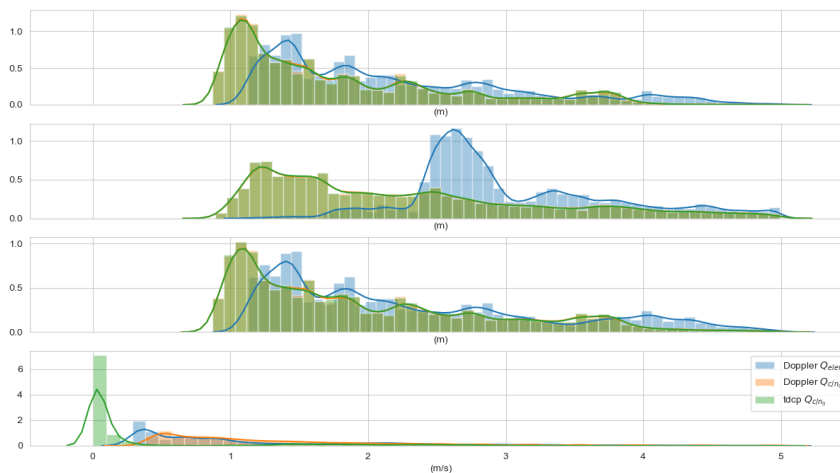

Figure 36: Internal reliability (MDB_1) for ambiguities, code, carrier-phase and Doppler or time-differenced carrier phase observable shown in the four panels respectively. For buoy experiments with three different processing settings: Blue: [variance: elev, Velocity: Doppler], Orange: [variance: C/N_0, velocity: Doppler], and Green: [C/N_0, velocity: Time-differenced carrier-phase].

The major difference in terms of the first three subfigures is found in code and carrier-phase observables. In both cases the elevation based variance model results in higher MDB_1. This is a direct result

from again the mathematical difference between both models. As the elevation based variance model is more pessimistic about low elevation satellites. This leads to smaller wiggle room for measurements from these satellites to help identify anomalies in measurements of other satellites.

The fourth row shows primarily that the internal reliability for processing settings using the time-differenced carrier-phase Green: [C/N_0, velocity: Time-differenced carrier-phase] is more reliable compared to the other two processing settings: Blue: [variance: ele, velocity: Doppler] and Orange: [variance: C/N_0, velocity: Doppler]. Comparison between these two shows that the elevation based model is more reliable. This may be caused again by difference in weights for low-elevation satellites.

6.5.3.2 *External Reliability: Position and Velocity State Estimates*

Fig. 37 and Fig. 38 show the external reliability of horizontal position and velocity components. The MDB of each individual observation were propagated as a separate hypothesis. reliability. The largest re-
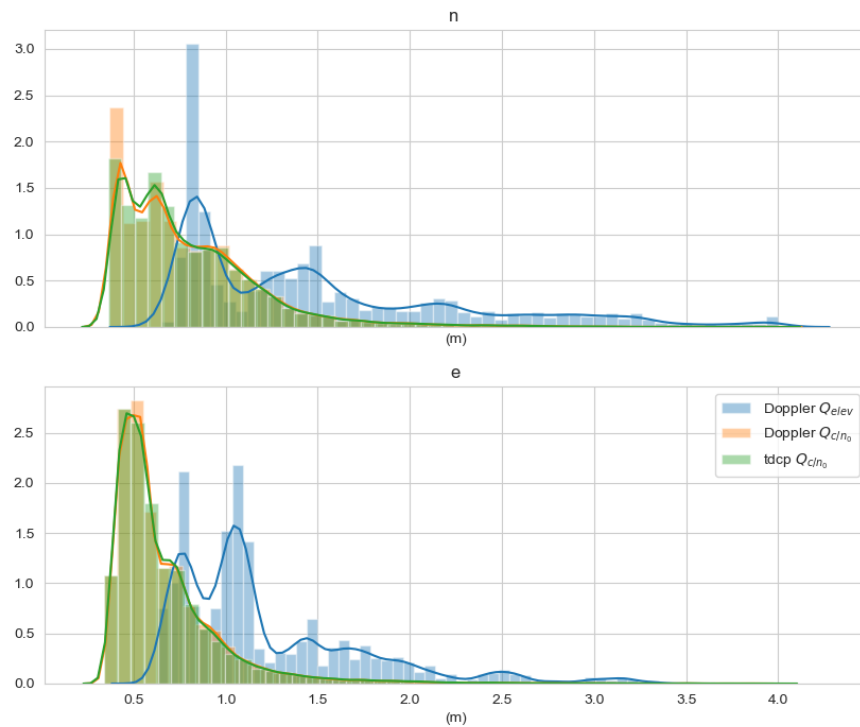

Figure 37: External reliability for North and East **position** components. For buoy experiments for three different processing settings: Blue: [variance: elev, Velocity: Doppler], Orange: [variance: C/N_0, velocity: Doppler], and Green: [C/N_0, velocity: Time-differenced carrier-phase]

sulting biases on the position and velocity state estimates were taken and shown as a histogram. For the horizontal position components

both North and East the carrier-to-noise density ratio model outper-
forms the elevation model. The bias undetected by a probability γ_0
that may propagate into the final estimates is in the order of decime-
ter to one meter. This can be explained from the internal reliability,
that of course propagates into the external

A similar consequence is manifested in Fig. 38. Where the carrier-to-
noise density based variance model for Doppler has a much wider tail
compared the other two models. Where the external reliability bias
peaks are found at 0.05, 0.25 and 0.35 [m/s] approximately for both
horizontal velocity components, for the three respective models: time-
differenced carrier phase carrier-to-noise density ratio, elevation and
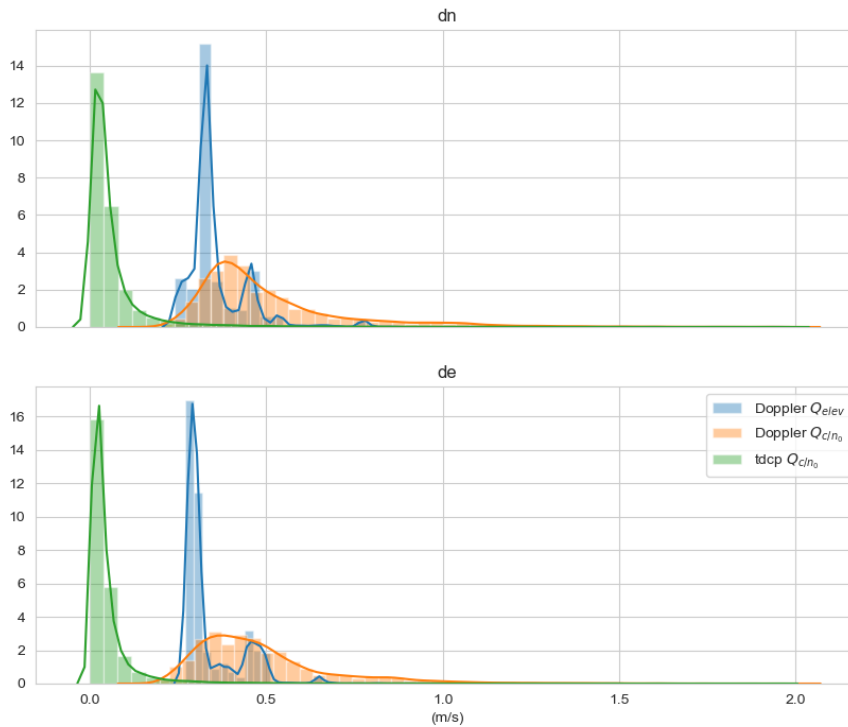Doppler carrier-to-noise density ratio based models. We can conclude

Figure 38: External reliability for North and East **velocity** components. GPS-
only. For buoy experiments for three different processing settings:
Blue: [variance: elev, Velocity: Doppler], Orange: [variance: C/N_0,
velocity: Doppler], and Green: [C/N_0, velocity: Time-differenced
carrier-phase]

based on the external reliability that for at least the time-differenced
carrier phase case the model is robust against outliers by means of
DIA procedure.

6.6 MOUNTED ON CAR ROOF, DRIVING A REGIONAL ROAD

The regional road experiment is described in Ch. 4.

6.6.1   Position in the Moving Car Case

Horizontal position error components for both rovers are shown for GPS-only in Fig. 39 and Fig. 40. The GPS-only carrier-to-noise vari-
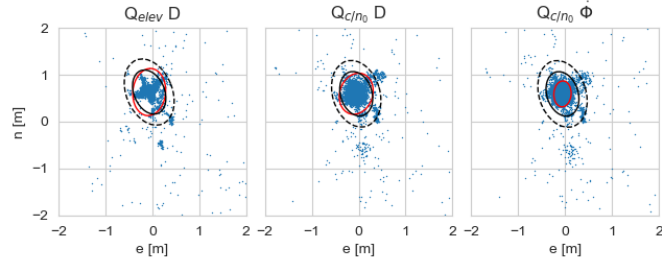

Figure 39: Horizontal **position** component estimates in local North and East for car experiment receiver 1. The columns represent three different combinations. Doppler with elevation-based variance, Doppler with C/N_0-based variance, and TDCP with C/N_0-based variance. All states are processed with GPS-only.

ance model performs slightly better. With a bias of around 0.595[m] and -0.051[m] in North and East directions. Standard deviation of 0.236[m] and 0.176[m] in both directions. The bias for the elevation based variance model is worse better at 0.623[m] and -0.066[m]. With similar horizontal position error component for North an East: 0.235[m] and 0.177[m] respectively.

Figure 40: Horizontal **position** component estimates in local North and East for car experiment receiver 2. See caption Fig. 39

6.6.2   Velocity in the Moving Car Case

Fig. 41 and 42 show the horizontal velocity error components for both rovers of the car experiment. Biases for all three models are about 0.001[m/s]. Standard deviations of both Doppler based models are rather similar at 0.045[m/s] and 0.03[m/s] in North and East directions.

From Tab. 8 and Figs. 41 and 42 we can further see that the precision of the TDCP based velocity state estimates remain more precise

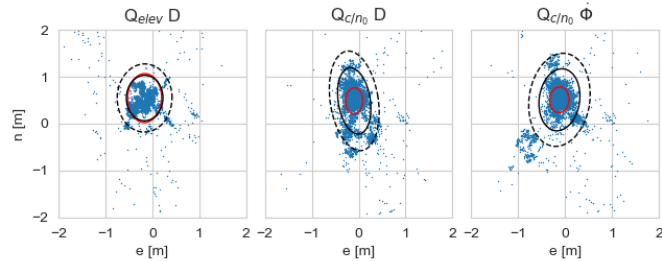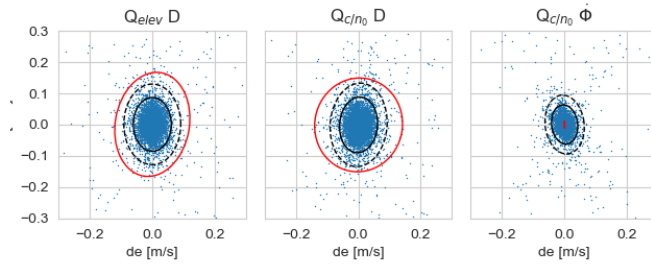Figure 41: Horizontal **velocity** component estimates in local North and East for car experiment receiver 1. See caption Fig. 39
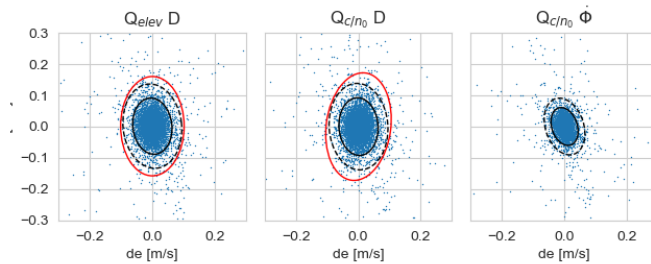
Figure 42: Horizontal **velocity** component estimates in local North and East for car experiment receiver 2. See caption Fig. 39

compared to the Doppler observable state estimates. However this difference is smaller in this case compared to the static rooftop and drifting buoy experiments. This could follow from the mathematical nature of the TDCP differentiator that has trouble keeping up if the platform moves more erratic, as described in Ch. 3.

Finally the set threshold for position of 0.5[m] is not met. This is mainly caused by a large bias for the North component. This could have been caused by the loss of satellites South and North of the rover. As shown in overview Fig. 13 possibly caused by trees or other fence like objects next to the road. In terms of velocity the Threshold of 0.1[m/s] RMSE is met by both Doppler and TDCP based processing settings.

DISCUSSION

7.1 KINEMATIC EXPERIMENT REFERENCE

Central to evaluation of horizontal position- and velocity state estimates is the ground truth or reference used. In contrast to the static rooftop experiment there was no reference available for kinematic experiments. Therefore we followed the method by de Bakker and Tiberius [2017] and employed a real-time kinematic (RTK) based solution. With a high-end base station setup on shore for the drifting buoy experiments and using available reference station DLF1 at the TU Delft campus for the regional road experiment.

In the RTK-based computed reference case we introduce a weakness. It uses the same measurements of the moving target receiver as the experiment itself. The RTK-based solution has a one order of magnitude better position accuracy than the to-be evaluated PPP-solution, but it is unavoidable that errors that occur in one solution likely correspond to errors in the other solution. One of the major upsides of this technique is the minimal amount of extra hardware required, which means less prone to human error.

Furthermore the PPP-solution primarily relies on the pseudorange measurements, whereas the RTK-solution, once the carrier phase ambiguities are fixed, relies solely on the carrier phase measurements. So the emphasis for both PPP and RTK is placed on different measurements, leading to smaller effect errors that are occur in both solutions have.

7.2 MULTIPATH CONSIDERATIONS

In general multipath effects on GNSS measurements are very hard to model. Observation combinations using measurements from on site experiments may be the most realistic method, where one can leverage the difference in magnitude of multipath between pseudorange and carrier-phase observations. [de Bakker et al., 2012]

It is possible to simulate these signals in a controlled environment by simplification; for instance capping the amount of signal bounces. Wieser [2007] applies a simple geometric relation using a single satellite a receiver and a planar reflector for multipath delay:

$$m = 2d\cos(\Psi) \tag{88}$$

With m the multipath delay in meters, d the height of the receiver above the planar reflector and Ψ angle of incidence between reflec-

tor and receiver. Obviously the height of receiver above the reflector is important, since it determines directly the maximum distance the signal can travel in addition to the direct line of sight.

This multipath signal delay then has to be transformed through a receiver simulation to get insight how much influence the multipath delay has on the mutlipath delay in the measurements.

This type of simulation was proven to be capable to work reasonably well for very simple geometry cases in real world applications for GNSS by Smyrnaios et al. [2013]. Adding complexity means that this model will likely fail on several grounds to represent the real world adequately. Which leads to the conclusion that it almost always more fruitful to design an experiment to retrieve multipath on at least the pseudorange measurements.

7.3 FURTHER DIRECTIONS IN VELOCITY ESTIMATION

We have explored a small subset of the solution space, spanning minimal assumptions on rover dynamics. This leaves us with minimal to no tuning. There are however various directions left unexplored.

As shown by the short-baseline experiment, both code and Doppler observables for the ublox neo m8t receiver show on-the-fly signal tracking parameter tuning. This effect was too pronounced for our two simple models to be captured. It could be fruitful to employ a n-degree polynomial model that operates well between the available carrier-to-noise density ratios (between 20 and 55 [dB-Hz]). This has the downside that one should be careful to carry over such a model from one receiver to the other. But the upside is that when a receiver uses parameter tuning, these signals will be better represented by the variance model. Thereby improving state estimates.

Another route would be the use of a dynamic model, which will work in concert with the measurement model. Explained for instance in Teunissen [2001a]. One dynamic model that can be used is the constant velocity model. This would make assumptions on the dynamics of the application. In case of a buoy, the main direction of current would be emphasized as being the constant velocity. Whereas the short-term motion superimposed on current due to the waves would be filtered out. When the assumptions on the dynamics hold true for the application at hand, employing them in the estimation process leads to improved precision for the (unbiased) state estimators.

Finally it may be fruitful to add additional means of measuring velocity to the platform. Inertial measurement units consisting of a 3-axis accelerometer, -magnetometer and -gyroscope come in compact low-cost modules. And have proven as a possibility to improve positioning, so why not velocity. Henkel and Iafrancesco [2014] Falco et al. [2014]

CONCLUSION

8.1 APPROACH TO ESTIMATE VELOCITY

The Delft GNSS real-time single-frequency precise point positioning algorithm is extended to include velocity and clock drift as states, which allows to take redundancy into account to perform DIA on the full state vector and incorporates covariance between position- and velocity based observables; where for instance a fault identified in a Doppler observation may help identify a cycle slip on a carrier-phase observable. Furthermore, the algorithm is applicable anywhere on the surface of the Earth without needing a basestation, which makes it user friendly besides being operational in real-time.

8.1.1 Observation Standard deviation and Correlation

The u-blox neo m8t GNSS receiver is shown to apply on-the-fly tuning of signal processing parameters for satellite signals below 32[dB-Hz] carrier-to-noise density ratio. Through a short baseline experiment at carrier-to-noise density ratio reference value of 45[dB-Hz] it was found that the u-blox has a standard deviation for GPS L1 measurements of: 0.1974[m] (code), 0.0043[m] (carrier-phase), 0.0885[m/s] (Doppler), 0.006[m/s] (time-differenced carrier-phase) and 0.1227[dB-Hz] (carrier-to-noise density ratio) and it was shown that the Doppler and carrier-phase observable have negative correlation of ρ equals -0.75. Glonass measurements are found to be less precise, where carrier-phase may be influenced by frequency modulation. And Galileo Code observations are more precise, assumed due to the wider signal bandwidth and being at same frequency as GPS.

8.2 TWO DIFFERENT VARIANCE MODELS

Both variance models used: variance as function of satellite elevation and variance as function of carrier-to-noise density ratio have elongated North components of their respective confidence ellipses, this is expected from the satellite geometry with respect to the location of the Netherlands, at 52 degrees North. Of the two used variance models, the elevation based variance model outperformed the carrier-to-noise density ratio based variance model in terms of horizontal position component accuracy in most experiments. This can be explained by the differences in weights applied to measurements of low-elevation satellites by the two variance models, where the ele-

vation based model incorporates these satellites more loosely in the model compared to the carrier-to-noise density ratio model, and measurements from low-elevation satellites suffer more often from unmodelled effects like multipath plus these effects are larger in magnitude. By weighting these satellites more opportunely (in the C/N_0-based model) these unmodeled effects propagate more strongly into the state estimate resulting in worse state estimate accuracy.

8.3 EMPIRICAL POSITION AND VELOCITY ACCURACY

It was found that in terms of position in the static experiment and under calm water conditions during the drifting buoy experiment the horizontal RMSE was between 0.429 and 0.530 [m], and under rough water conditions in the drifting buoy experiment and during the regional road experiment between 0.682 and 0.812 [m]. During the rough water conditions waves washed over the buoy, which likely distorted the quality of the satellite signal and the road was partly flanked by fences and trees which probably caused the large North component bias.

For velocity it was found that the TDCP observable in combination with the carrier-to-noise density based variance model has a horizontal RMSE between 0.014 and 0.068 [m/s] over all experiments, and using the Doppler observable with either variance model a RMSE between 0.033 and 0.122 [m/s]. The Doppler observable does not meet the requirement of 0.1 [m/s] horizontal RMSE in the drifting buoy case, which does not mean it is without a use case as it is expected that under extreme conditions the Doppler will outperform the TDCP as it can better keep up with platform dynamics.

8.4 INTERNAL- AND EXTERNAL RELIABILITY

Baarda's internal reliability, MDB_1, were evaluated for the drifting buoy experiment. The MDB_1 shows differences mostly dictated by the variance model used. The elevation based variance model has a MDB_1 for Code observations concentrated at 2.8[m] versus 1.2[m] for carrier-to-noise density ratio model, for the carrier-phase observable the difference is smaller: MDB_1 of 1.4[m] versus 1.1[m] and in terms of velocity observables using the TDCP the MDB_1 is about 0.1[m/s] versus the Doppler observable at 0.35 and 0.5 [m/s] for both variance models respectively.

The external reliability was acquired by propagating the largest MDB_1 found at each epoch. It is shown that for horizontal position components by means of DIA the algorithm can remain under 0.5[m] for all processing settings where variance is C/N_0 based. Again explained by the C/N_0 variance model that applies more weight, compared to the elevation based variance model, to low elevation satel-

lites. Which means that these satellites can in theory be leveraged more easily to detect faults. For horizontal velocity components the TDCP based processing is capable of detecting faults at the boundary of the 0.1 [m/s] velocity requirement.

Concluding that in the drifting buoy case the TDCP based functional model and carrier-to-noise based variance model is a good match for the dynamics expected for a coastal drifter. Not only does the algorithm meet the requirements in terms of accuracy but also in terms of reliability for the developed position and velocity state estimation system.

A

GNSS SYSTEM

A.1 RECEIVER

The u-blox m8t neo GNSS receiver is used for experiments in this work. It has 72-channels, and is capable of concurrently receive three systems: GPS L1C/A, Galileo E1B/C, SBAS L1C/A, QZSS L1C/A, SAIF and GLONASS L1OF or BeiDou B1. Various single-frequency experiments found in de Bakker and Tiberius [2017] have been conducted using either this or a predecessors like the u-blox NEO 7 receiver.

A.2 ANTENNA

The Taoglas Magma AA 170 GNSS antenna is tuned for GPS+Galileo frequencies (1575.42 [Mhz]) and GLONASS frequency ($1598.0625 - 1609.3125$ [Mhz]). It is a car-type antenna with a strong magnet. It is recommended to use a groundplate to minimize the magnetic field from interacting with the electronics, which may have severe effects on the quality of measurements.

A.3 LOGGING AND RECEIVER SETUP

The field experiments were logged using a custom c-plus-plus program that configures and logs the data to SD-card. For this purpose any general linux-based microprocessor is capable as long as it has a compiler, but we went for the commonly available Raspberry Pi 3.

APPROXIMATION OF DOPPLER SHIFT FOR LIGHT

Let s be the source of light and o its observer. The relative velocity between both given by v, λ_0 and f_0 the wavelength and frequency when $v = 0$. Now imagine two consecutive crests of the signal. The received wavelength by observer o is given by:

$$\lambda = c_0 \Delta t - v \Delta t \tag{89}$$

With c_0 the speed of light in a vacuum, v the relative velocity between source and observer and Δt the time crest 1 has moved since transmission. Since light is subjected to special relativity, the time between emission of wavecrests undergoes time dilation. [Giancoli, 2008](pp. 979):

$$\Delta t = \Delta t_0 / \sqrt{1 - v^2/c^2} \tag{90}$$

With Δt_0 the time between emissions of wavecrests in reference frame of the source:

$$\Delta t_0 = \frac{1}{f_0} = \frac{\lambda_0}{c_0} \tag{91}$$

Using Eqs. 89, 90 and 91 we can write the received wavelength λ and frequency f as:

$$\lambda = \lambda_0 \sqrt{\frac{c_0 + v}{c_0 - v}}; \qquad f = \frac{c_0}{\lambda} = f_0 \sqrt{\frac{c_0 - v}{c_0 + v}} \tag{92}$$

As the relative velocity v is negative, s and o are moving towards each other. Hence the received frequency increases. And the other way around.

Wieser [2007] points out, most GNSS textbooks and papers use an approximated form for the received frequency f in Eq. 92. First rewrite f in Eq. 92 as:

$$f = f_0 \sqrt{\frac{c_0 + v}{c_0 - v}} = f_0 \sqrt{\frac{1 + v/c_0}{1 - v/c_0}} = f_0 \sqrt{\frac{1 + x}{1 - x}}; \quad x = v/c_0 \tag{93}$$

We know that for GNSS relative velocity $v \ll c_0$, thus x goes to 0. With this insight and f solely a function of x we approximate function $f(x)$ through Taylor series:

$$f(x) \approx f(0) + f'(0)x + \frac{1}{2}f''(0)x^2 + \dots \tag{94}$$

With:

$$f' = \frac{f_0}{2\sqrt{\frac{1+x}{1-x}}} \frac{2}{(1-x)^2} = \frac{f_0}{\sqrt{1+x}(1-x)^{3/2}} \tag{95}$$

From Eq.95 we see that $f'(0) = 0$. Using Eq. 95 in 94 and if the range rate between satellite and receiver is very small compared to the speed of light c_0 we get:

$$f(x) \approx f_0 + f_0 x = f_0(1 + x) = f_0(1 + \frac{v}{c_0}) \tag{96}$$

The Doppler shift is the received minus transmitted frequency $f_D = f - f_0 = f_0 \frac{v}{c_0}$. Multiply by wavelength λ to get the relative velocity in [m/s]:

$$D_o^s = \lambda f_D = \frac{\lambda f_0}{c_0} v = v \tag{97}$$

With D_o^s the Doppler shift in [m/s] between observer and source. Where for GNSS we split relative velocity v into satellite ^{s} and receiver $_r$ components:

$$D_r^s = a_r^s(\dot{s} - \dot{r}_r) \tag{98}$$

TWO DIMENSIONAL ORBIT SIMULATION

Let the Earth be two dimensional and perfectly circular. With radius $R_e = 6371000[m]$. There are N satellites. All in a circular orbit. With orbit radius $R^s = R_e + 25000[m]$. Distributed equally over the circle. The receiver is located on the surface at the North pole: $r_r = (x, y) = (0, Re)$. Tthe polar coordinates of satellite n as function of time t[s] be:

$$r^s(t) = (R^s, \theta(t) + \Delta\theta); \qquad \theta(t) = wt \qquad w = 2\pi/T \tag{99}$$

With satellite position $r^s(t)$ at time t. Time dependent angle on the unit circle $\theta(t)[rad]$. Static angle increment based on equally distributed satellites $\Delta\theta$. Orbital velocity $w[rad/s]$. And orbit period T[s].

Let Earth be represented by a circle with radius R_1. Let r be the line of sight vector between center of Earth [0, 0] and satellite. The satellite's orbit is circular. The length of vector $\|r\|$ gives the distance between Earth and satellite Vector r can therefore be represented by:

$$r = R(\cos(\theta); \sin(\theta)) \tag{100}$$

Where R is length of vector r and θ the angle between satellite with respect to Earth, where 0 degrees is East. We assume that the satellite travels its orbit at constant velocity. Angle θ as function of time t can be represented as:

$$\theta(t) = at \tag{101}$$

The function is known when the satellite makes a complete revolution, specifically at t = T. Where $\theta(t) = 2\pi$. This gives an expression for a:

$$a = \frac{2\pi}{T} \tag{102}$$

The total distance the satellite will travel in period T is equal to the circumference of this circular Earth. With constant velocity V this is:

$$VT = 2\pi R \tag{103}$$

$$T = \frac{2\pi R}{V}, f = \frac{1}{T} \tag{104}$$

Combining Eq. 101, 102, 103 and 104 gives an expression for $\theta(t)$:

$$\theta(t) = 2\pi ft = \frac{Vt}{R} \tag{105}$$

We can plug this result into Eq. 100 to get an expression for $r(t)$:

$$r(t) = R(\cos(\frac{Vt}{R}); \sin(\frac{Vt}{R})) \tag{106}$$

Now lets add toe receivers, r1 and r2. One exactly at the surface. The other h meter below. With positions $r1 = (0; R_1)$ and $r2 = (0; R_2)$. With $R_2 = R_1 - h$ and $h = 3(m)$.

The distance between receiver and satellite is described by:

$$s = \|r - r1\| = \sqrt{R^2 \cos^2(\frac{Vt}{R}) + (R\sin(\frac{Vt}{R}) - R_1 + h)^2} \tag{107}$$

Where $h = 0$ for receiver r1. We can differentiate this function with respect to time which gives an expression for line of sight velocity:

$$\dot{s} = -\frac{(R_1 - h)V\cos(\theta)}{s1} \tag{108}$$

Where $\dot{s}$ is the line of sight velocity between receiver and satellite. Using the following values and plugging them in:

variable	value	units
R	26500000	m
θ	0	degree
V	4×10^{3}	m/s
h	3	m
R1	6378000	m

This gives the following results. In case of the DD combination the geometric order of magnitude that remains and if we should correct for this effect. The component itself is in the order of 10^{-4} [m/s]. This means it is indeed not fruitful to correct for leftover geometric effects in the DD combination for velocity observables.

variable	value	unit
s1	27256721.8132	m
s2	27256721.1112	m
$\dot{s}1$	-935.9893	m/s
$\dot{s}2$	-935.9889	m/s
$\dot{s}1 - \dot{s}2$	-0.0004	m/s

DB-HZ TO RATIO-HZ

Starting with standard deviation model used in de Bakker et al. [2009] as:

$$\sigma_\Phi = a10^{-(C/N_0-45)/20} \tag{109}$$

With C/N_0 in units of [dB-Hz]. Now lets write factor 45 in units of ratio-Hz as b. The original ratio-Hz quantities C/N_0 and b are converted to dB-Hz units through: $10\log_{10}(C/N_0)$ and $10\log_{10}(b)$. The equation becomes:

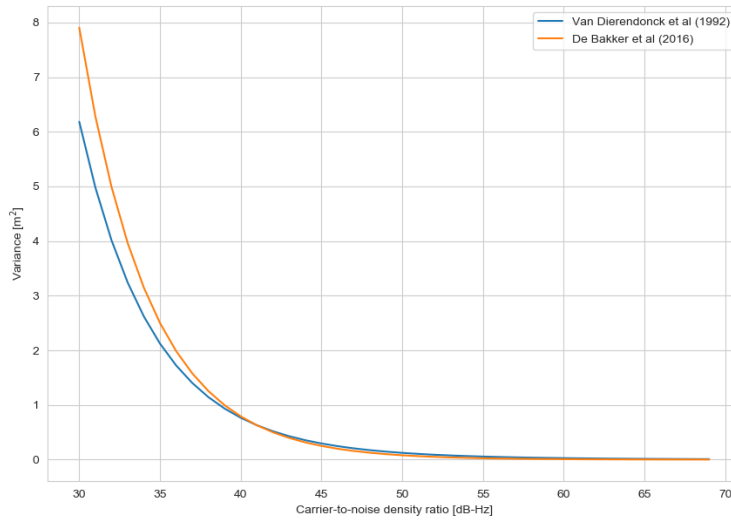$$\sigma_\Phi = a10^{-(10\log_{10}(C/N_0)-10\log_{10}(b))/20} \tag{110}$$

Figure 43: Representation of empirical and formal variance models for code observables. Van Dierendonck et al. [1992].

Convert standard deviation to variance:

$$\sigma_\Phi^2 = (a10^{-(10\log_{10}(C/N_0)-10\log_{10}(b))/20})^2 \tag{111}$$

Reformulating the term in brackets partially using power- and logarithmic rules, $(b^n)^m = b^{nm}$ and $a^{\log_a(b)} = b$:

$$(10^{-(10\log_{10}(C/N_0)-10\log_{10}(b))/20})^2 = \frac{b}{C/N_0} \tag{112}$$

And getting rid of the brackets by squaring we get a final expression:

$$\sigma_\Phi^2 = a^2 b \frac{1}{C/N_0} \tag{113}$$

A representation of the formal variance of Φ is given by Van Dierendonck et al. [1992] as:

$$\sigma_\Phi^2 = \frac{\lambda^2}{4\pi^2} \frac{B_{PLL}}{C/N_0} (1 + \frac{1}{TC/N_0}) \quad [m^2] \tag{114}$$

Where the ratio-Hz C/N_0 quantity also appears at the denominator side of the equation. Underlining the similarity between both. Also shown in Fig. 43. Both models are put on display. With $a = 0.5$.

OVERVIEW IMAGES OF EXPERIMENTS

E.1 SHORT-BASELINE EXPERIMENT

Figure 44

E.2 NORTH SEA DRIFTING BUOY EXPERIMENT
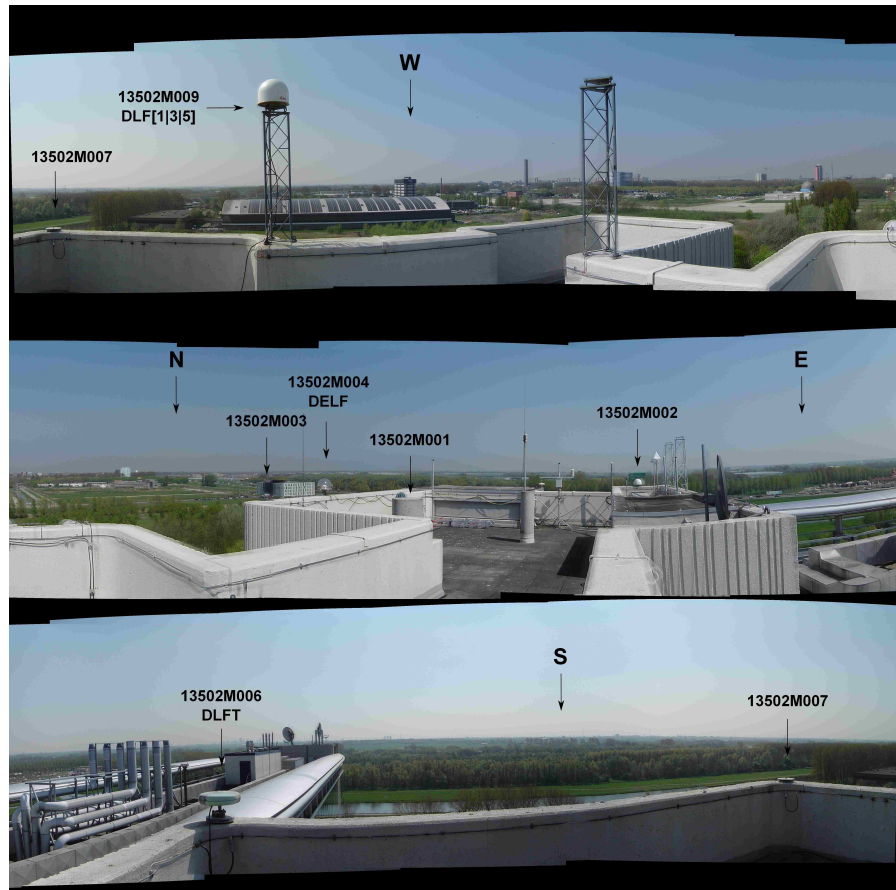
Figure 45: Delft GNSS Observatorium Overview Image, taken from http://gnss1.tudelft.nl/dpga/station/Delft.html from the site pictures section, 03/01/2021

Figure 46: Two of our buoys (orange flags) drifting freely near Scheveningen harbor in the Netherlands. The larger buoy, de Kardinaal, is chained to the ocean floor. The smaller buoys are equipped with ublox-neo m8t single frequency GNSS receivers. The antenna is from Taoglass of type Magma X AA.170.

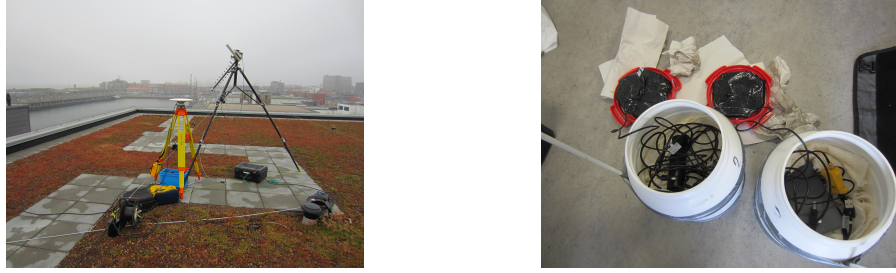Figure 47: Left: Basestation set up on the roof of Sailing Innovation Centre, Scheveningen harbor at longitude and latitude: (52.097922, 4.264947). Right: Both buoys opened up. The lit contains a metal baseplate with the antenna mounted on top of it. The duct tape is made sure not to interfere with the satellite signal. The box further contains a small power supply, a Raspberry Pi 3 micro processor and GNSS receiver ublox-neo m8t.

F

COMMONALITIES IN PROCESSING OPTIONS

Parameter	Value	Units
Ionosphere height	400	km
Sat elevation cutoff	10	deg
lom α	0.001	-
w-test α	0.001	-
w-test β	0.2	-
Measurement frequency	10	Hz
Constellations	GPS, Galileo, GLONASS	

Table 9: List of common processing options used throughout the experiments.

A. Alonso-Arroyo, A. Camps, H. Park, D. Pascual, R. Onrubia, and F. Martín. Retrieval of significant wave height and mean sea surface level using the GNSS-R interference pattern technique: Results from a three-month field campaign. *IEEE Transactions on Geoscience and Remote Sensing*, 53(6):3198–3209, 2015.

S. Andrew and F. Boon. Carrier phase and Doppler-based algorithms for real-time standalone positioning. In *Proceedings of the GNSS. 2003.*, 2003.

B. Aumayer and M. Petovello. Effect of sampling rate error on GNSS velocity and clock drift estimation. *Navigation: Journal of The Institute of Navigation*, 62(3):229–238, 2015.

C. Aydin and H. Demirel. Computation of Baarda's lower bound of the non-centrality parameter. *Journal of geodesy*, 78(7-8):437–441, 2004.

W. Baarda. A testing procedure for use in geodetic networks. 1968.

S. Beer, L. Wanninger, and A. Heßelbarth. Galileo and glonass group delay variations. *GPS Solutions*, 24(1):23, 2020.

D. M. Bevly, J. C. Gerdes, C. Wilson, and G. Zhang. The use of GPS based velocity measurements for improved vehicle state estimation. In *American Control Conference, 2000. Proceedings of the 2000*, volume 4, pages 2538–2542. IEEE, 2000.

D. Borio, N. Sokolova, and G. Lachapelle. Doppler measurements and velocity estimation: A theoretical framework with software receiver implementation. In *Proceeding of ION GNSS*, pages 23–25, 2009.

K. Borre and C. Tiberius. Time series analysis of GPS observables. In *Proceedings of ION GPS*, pages 19–22. Citeseer, 2000.

B. H. Brumley, R. G. Cabrera, K. L. Deines, and E. A. Terray. Performance of a broad-band acoustic Doppler current profiler. *IEEE Journal of Oceanic Engineering*, 16(4):402–407, 1991.

A. M. Bruton. *Improving the accuracy and resolution of SINS/DGPS airbone gravimetry*. Calgary, 2000.

M. Caparrini, A. Egido, F. Soulat, O. Germain, E. Farres, S. Dunne, and G. Ruffini. Oceanpal®: Monitoring sea state with a GNSS-R coastal instrument. In *Geoscience and Remote Sensing Symposium, 2007. IGARSS 2007. IEEE International*, pages 5080–5083. IEEE, 2007.

P. F. De Bakker. *On user algorithms for GNSS precise point positioning*. PhD thesis, TU Delft, Delft University of Technology, 2016.

P. F. de Bakker and C. C. Tiberius. Real-time multi-GNSS single-frequency precise point positioning. *GPS Solutions*, 21(4):1791–1803, 2017.

P. F. de Bakker, H. van der Marel, and C. C. Tiberius. Geometry-free undifferenced, single and double differenced analysis of single frequency GPS, EGNOS and GIOVE-A/B measurements. *GPS solutions*, 13(4):305–314, 2009.

P. F. de Bakker, C. C. Tiberius, H. Van Der Marel, and R. J. van Bree. Short and zero baseline analysis of GPS L1 C/A, L5Q, GIOVE E1B, and E5aQ signals. *GPS solutions*, 16(1):53–64, 2012.

W. Ding and J. Wang. Precise velocity estimation with a stand-alone GPS receiver. *The Journal of Navigation*, 64(2):311–325, 2011.

G. Falco, M. C.-C. Gutiérrez, E. Serna, F. Zacchello, and S. Bories. Low-cost real-time tightly-coupled GNSS/INS navigation system based on carrier-phase double-differences for UAV applications. In *Proceedings of the 27th International Technical Meeting of the Satellite Division of The Institute of Navigation (ION GNSS 2014), Tampa, FL, USA*, volume 812, page 841857, 2014.

P. Freda, A. Angrisano, S. Gaglione, and S. Troisi. Time-differenced carrier phases technique for precise GNSS velocity estimation. *GPS Solutions*, 19(2):335–341, 2015.

D. C. Giancoli. *Physics for scientists and engineers*. 2008.

W. Gurtner and L. Estey. Rinex-the receiver independent exchange format-version 3.00. *Astronomical Institute, University of Bern and UNAVCO, Bolulder, Colorado.*, 2007.

P. Henkel and M. Iafrancesco. Tightly coupled position and attitude determination with two low-cost GNSS receivers. In *2014 11th International Symposium on Wireless Communications Systems (ISWCS)*, pages 895–900. IEEE, 2014.

T. Herbers, P. Jessen, T. Janssen, D. Colbert, and J. MacMahan. Observing ocean surface waves with GPS-tracked buoys. *Journal of Atmospheric and Oceanic Technology*, 29(7):944–959, 2012.

R. Hohensinn, A. Geiger, D. Willi, and M. Meindl. Movement detection based on high-precision estimates of instantaneous GNSS station velocity. *Journal of Surveying Engineering*, 145(3):04019005, 2019.

D. Imparato, P. Teunissen, and C. Tiberius. Minimal detectable and identifiable biases for quality control. *Survey review*, pages 1–11, 2018.

C. Jekeli. *Inertial navigation systems with geodetic applications*. Walter de Gruyter, 2012.

E. D. Kaplan and C. Hegarty. *Understanding GPS/GNSS: Principles and applications*. Artech House, 2017.

S. Kennedy. Precise acceleration determination from carrier-phase measurements. *Navigation*, 50(1):9–19, 2003.

F. Kleijer. *Troposphere modeling and filtering for precise GPS leveling*. PhD thesis, TU Delft, Delft University of Technology, 2004.

V. Klemas. Remote sensing of coastal and ocean currents: An overview. *Journal of Coastal Research*, 28:576–586, 05 2012. doi: 10.2112/JCOASTRES-D-11-00197.1.

S.-G. Kong and K. Okajima. Diverse photoreceptors and light responses in plants. *Journal of plant research*, 129(2):111–114, 2016.

N. J. M. Laxague, T. M. Özgökmen, B. K. Haus, G. Novelli, A. Shcherbina, P. Sutherland, C. M. Guigand, B. Lund, S. Mehta, M. Alday, and J. Molemaker. Observations of near-surface current shear help describe oceanic oil and plastic transport. *Geophysical Research Letters*, 45(1):245–249, 2018. doi: 10.1002/2017GL075891. URL https://agupubs.onlinelibrary.wiley.com/doi/abs/10.1002/2017GL075891.

A. Le, C. Tiberius, H. Van der Marel, and N. Jakowski. Use of global and regional ionosphere maps for single-frequency precise point positioning. In *Observing our Changing Earth*, pages 759–769. Springer, 2009.

A. Q. Le and C. Tiberius. Single-frequency precise point positioning with optimal filtering. *GPS solutions*, 11(1):61–69, 2007.

J. Liu, W. J. Emery, X. Wu, M. Li, C. Li, and L. Zhang. Computing coastal ocean surface currents from modis and viirs satellite imagery. *Remote Sensing*, 9(10):1083, 2017.

R. G. Lyons. *Understanding digital signal processing, 3/E*. Pearson Education India, 2004.

P. Misra and P. Enge. Global positioning system: signals, measurements and performance second edition. *Massachusetts: Ganga-Jamuna Press*, 2006.

O. Montenbruck, A. Hauschild, and P. Steigenberger. Differential code bias estimation using multi-GNSS observations and global ionosphere maps. *Navigation: Journal of The Institute of Navigation*, 61(3):191–201, 2014.

F. G. Nievinski and K. M. Larson. Forward modeling of GPS multipath for near-surface reflectometry and positioning applications. *GPS solutions*, 18(2):309–322, 2014.

K. Oberg and D. S. Mueller. Validation of streamflow measurements made with acoustic Doppler current profilers. *Journal of Hydraulic Engineering*, 133(12):1421–1432, 2007.

C. Ohlmann, P. White, L. Washburn, B. Emery, E. Terrill, and M. Otero. Interpretation of coastal hf radar–derived surface currents with high-resolution drifter data. *Journal of Atmospheric and Oceanic Technology*, 24(4):666–680, 2007.

T. G. Online. Coasts. 01-10-2019. URL https://www.thegeographeronline.net/coasts.html.

J. D. Paduan and L. K. Rosenfeld. Remotely sensed surface currents in monterey bay from shore-based hf radar (coastal ocean dynamics application radar). *Journal of Geophysical Research: Oceans*, 101(C9): 20669–20686, 1996.

W. A. Peer, J. J. Blakeslee, H. Yang, and A. S. Murphy. Seven things we think we know about auxin transport. *Molecular plant*, 4(3):487–504, 2011.

I. S. Robinson. *Measuring the oceans from space: the principles and methods of satellite oceanography*. Springer Science & Business Media, 2004.

R. Romeiser. High-resolution imaging of current fields from satellites. *Sea Technology*, 48(9):44–46, 2007.

R. Romeiser, H. Breit, M. Eineder, H. Runge, P. Flament, K. De Jong, and J. Vogelzang. Current measurements by SAR along-track interferometry from a space shuttle. *IEEE Transactions on Geoscience and Remote Sensing*, 43(10):2315–2324, 2005.

D. Salazar, M. Hernandez-Pajares, J. M. Juan-Zornoza, J. Sanz-Subirana, and A. Aragon-Angel. Eva: GPS-based extended velocity and acceleration determination. *Journal of Geodesy*, 85(6):329–340, 2011.

L. Serrano, D. Kim, and R. B. Langley. A single GPS receiver as a real-time, accurate velocity and acceleration sensor. In *Proceedings of the the 17th international technical meeting of the satellite division of the institute of navigation (ION GNSS 2004), Long Beach, CA, USA*, volume 2124, 2004.

M. Smyrnaios, S. Schön, and M. L. Nicolás. Multipath propagation, characterization and modeling in GNSS. *Geodetic sciences-observations, modeling and applications*, pages 99–125, 2013.

P. Teunissen. An integrity and quality control procedure for use in multi sensor integration. In *ION GPS Redbook Vol. VII Integrated Systems*. Institute of Navigation (ION), 1990.

P. Teunissen. Adjustment theory, series on mathematical geodesy and positioning, 2000.

P. Teunissen. *Dynamic data processing, Series on Mathematical Geodesy and Positioning*. VSSD, 2001a.

P. Teunissen. *Testing theory, Series on Mathematical Geodesy and Positioning*. VSSD, 2006.

P. Teunissen. Distributional theory for the DIA method. *Journal of geodesy*, 92(1):59–80, 2018.

P. Teunissen and O. Montenbruck. *Springer handbook of global navigation satellite systems*. Springer, 2017.

P. Teunissen and S. Verhagen. GNSS carrier phase ambiguity resolution: challenges and open problems. In *Observing our changing Earth*, pages 785–792. Springer, 2009.

P. Teunissen, P. Joosten, and C. Tiberius. A comparison of TCAR, CIR and LAMBDA GNSS ambiguity resolution. In *Proceedings of the 15th International Technical Meeting of the Satellite Division of the Institute of Navigation (ION GPS 2002)*. ION, 2003.

P. Teunissen, D. Simons, and C. Tiberius. Probability and observation theory, lecture notes. *University of Technology Delft*, 2006.

P. J. Teunissen. GNSS ambiguity bootstrapping: theory and application. In *Proceedings of international symposium on kinematic systems in Geodesy, geomatics and navigation*, pages 246–254, 2001b.

P. J. Teunissen, N. Jonkman, and C. Tiberius. Weighting GPS dual frequency observations: bearing the cross of cross-correlation. *GPS Solutions*, 2(2):28–37, 1998.

M. Valk, H. Savenije, C. Tiberius, and W. Luxemburg. Determining slack tide with a GPS receiver on an anchored buoy. *Hydrology and Earth System Sciences*, 18(7):2599, 2014.

R. J. van Bree and C. C. Tiberius. Real-time single-frequency precise point positioning: accuracy assessment. *GPS solutions*, 16(2):259–266, 2012.

A. Van Dierendonck, P. Fenton, and T. Ford. Theory and performance of narrow correlator spacing in a gps receiver. *Navigation*, 39(3):265–283, 1992.

M. Vigo, M. D. Sempere, B. F. Chao, and M. Trottini. Mediterranean surface geostrophic circulation from satellite gravity and altimetry observations. *Pure and Applied Geophysics*, 175(11):3989–4005, 2018.

A. Wieser. *GPS based velocity estimation and its application to an odometer*. Shaker, 2007.

S. Zaminpardaz and P. Teunissen. DIA-datasnooping and identifiability. *Journal of Geodesy*, pages 1–17, 2018.

J. Zhang. Precise velocity and acceleration determination using a standalone GPS receiver in real time. 2007.